# MASTERARBEIT | MASTER'S THESIS

Titel | Title

Quantifying shear strain of a potential halite detachment below the Swiss Eastern Tabular Jura

verfasst von | submitted by

Alina Mohideen BSc

angestrebter akademischer Grad | in partial fulfilment of the requirements for the degree of

Master of Science (MSc)

Wien | Vienna, 2025

| | |
|---|---|
| Studienkennzahl lt. Studienblatt \| Degree programme code as it appears on the student record sheet: | UA 066 815 |
| Studienrichtung lt. Studienblatt \| Degree programme as it appears on the student record sheet: | Masterstudium Erdwissenschaften |
| Betreut von \| Supervisor: | Dr. Kurt Decker |

# I. Acknowledgement

At this point I would like to thank everyone who supported and motivated me in the development of this master's thesis. I would especially like to thank my thesis supervisor Dr. Kurt Decker who supported me in my practical work and answered all of my questions with great patience.

Special thanks go to Nagra for giving me access to the core samples and financially supporting my master's thesis.

I would also like to thank Univ. Prof. Mag. Dr. Susanne Gier, who gave me access to the X-ray diffractometer of the University of Vienna.

Finally, I would like to thank my family and friends, who have supported and motivated me throughout the long process of completing my master's thesis.

# II. Abstract

The National Cooperative for Radioactive Waste Disposal (NAGRA) recently has drilled through the evaporitic successions of the Zeglingen Fm., which are known to form a major detachment along the floor thrust of the Jura fold-and-thrust belt in northern Switzerland, at four locations within the "Vorfaltenzone". The core sections from the so-called "Salzlager" of the Zeglingen Fm. examined in this thesis mainly consist of halite, anhydrite and clay in different quantities and degrees of viscous deformation. Based on mineralogical content and degree of deformation core sections were divided into different lithological units and summarised in lithological profiles. A model describing the potential evolution of the different evaporitic rock types was elaborated.

To test the competing deformation models (thin-skinned vs. thick-skinned) for this tectonic domain, cores from these Zeglingen evaporites are analysed for structures which can be used for quantifying the shear strain of the drilled anhydrite and halite. Cores are oriented allowing to determine the true orientation of structures. Variably oriented stretching lineations along with sigma clasts and other shear sense indicators (shear bands, winged inclusions, asymmetrical boudins, `V´-pull-aparts) prove polyphase kinematics with different transport directions arguing against a continuous high-strain detachment. Recorded shear directions are top-NNW, top-NNE and top-W.

Winged inclusions, relatively high angles between S and C planes in shear bands, elongations calculated from boudinaged layers and the abundance and sizes of survivor grains are used to estimate the finite shear strain for the different lithotypes, which are categorised in coaxial ($\gamma=0$), low shear strain ($\gamma<2$), medium shear strain ($\gamma<7$), and high shear strain ($\gamma<15$). The total displacement, calculated from the sum of the thickness-shear strain products for each strain category, accommodated by the analysed sections of the "Salzlager" range from ca. 41 to 123m for the four analysed boreholes. The stated numbers are maximum values.

Studies of thin-skinned deformation models for the area of interest state a shortening, estimated from balanced cross-sections, of approximately 150 to 220m of the Jura fold-and-thrust belt, which is accommodated in the so-called Siglistorf Anticline north of the investigated boreholes. In this thin-skinned model the whole respective displacement must be accommodated by the regional detachment of the Zeglingen evaporites, which, however

would not be feasible with the total maximum displacements derived from the cores of the "Salzlager". Therefore other detachments in the Zeglingen Fm. would also have to be involved in the decoupling process to make the accommodation of the postulated shortening of 150 to 220m feasible. Alternatively, some of the overall shortening compensated by the Siglistorf Anticline could be due to the involvement of the basement, inferring thick-skinned deformation. Based on the systematic measurements and calculations of the current study it is therefore rather likely that the deformation of the most eastern part of the Jura fold-and-thrust belt is in fact a combination of thin-skinned and late stage thick-skinned tectonics.

# III. Zusammenfassung

Die Nationale Genossenschaft für die Lagerung radioaktiver Abfälle (NAGRA) hat kürzlich innerhalb der „Vorfaltenzone“ vier Bohrungen durchgeführt, die die Evaporitabfolgen der Zeglingen-Fm., die den basalen Abscherhorizont des Jura Falten- und Überschiebungsgürtels in der nördlichen Schweiz bilden, durchteuft haben. Die in dieser Arbeit untersuchten Kernabschnitte aus dem sogenannten „Salzlager“ der Zeglingen-Fm. bestehen hauptsächlich aus Halit, Anhydrit und Ton in unterschiedlichen Mächtigkeiten und Intensitäten viskoser Deformation. Basierend auf der mineralogischen Zusammensetzung und dem Deformationsgrad wurden die Kerne in verschiedene lithologische Einheiten unterteilt und in lithologischen Profilen zusammengefasst. Es wurde ein Modell ausgearbeitet, das die mögliche Entwicklung der verschiedenen Evaporittypen beschreibt.

Um die konkurrierenden Deformationsmodelle (thin-skinned vs. thick-skinned) für diesen tektonischen Bereich zu testen, werden Kerne der Zeglingen-Evaporite im Hinblick auf Strukturen analysiert, die für die Quantifizierung der Scherdeformation verwendet werden können. Die orientiert gewonnenen Kerne ermöglichen die wahre geographische Orientierung von Strukturen einzumessen. Unterschiedlich orientierte Streckungslineare zusammen mit Sigmaklasten und anderen Schersinnindikatoren (Scherbänder, winged inclusions, asymmetrische Boudins, `V´-pull-aparts) beweisen eine mehrphasige Kinematik mit unterschiedlichen Transportrichtungen, die gegen einen durchgehend hoch deformierten Abscherhorizont sprechen. Die aufgezeichneten Scherrichtungen sind top-NNW, top-NNO und top-W.

Winged inclusions, relativ große Winkel zwischen S- und C-Flächen in Scherbändern, aus boudinierten Schichten berechnete Elongationen, sowie die Häufigkeit und Größe von survivor grains werden verwendet, um die finite Verformung der verschiedenen Lithotypen abzuschätzen, die in koaxial ($\gamma$=0), geringer shear strain ($\gamma$<2), mittlerer shear strain ($\gamma$<7) und hoher shear strain ($\gamma$<15), kategorisiert werden. Der Gesamtversatz, berechnet aus der Summe der Produkte aus Mächtigkeit und strain für jede der vier Strainkategorien, reicht in den vier untersuchten Bohrungen von ca. 41 bis 123 m. Die angegebenen Zahlen sind Maximalwerte.

Auf thin-skinned-Tektonik basierende Deformationsmodelle ergeben eine Verkürzung des Jura-Falten- und Überschiebungsgürtels im Untersuchungsgebiet von etwa 150 bis 220 m. Diese Werte wurden aus der Bilanzierung von geologischen Profilen durch die sogenannte Siglistorf Antiklinale entnommen, die nördlich der in dieser Arbeit betrachteten Bohrungen liegt. In diesem thin-skinned Modell muss der gesamte Versatz am regionalen Hauptabscherhorizont der Zeglingen-Fm. erfolgen. Dies ist jedoch mit den gesamten maximalen Versätzen, die aus den hier untersuchten Kernen des „Salzlagers“ abgeleitet wurden, nicht möglich. Um die Aufnahme der postulierten Verkürzung von 150 bis 220 m möglich zu machen, müssten daher noch weitere Abscherhorizonte innerhalb der Zeglingen-Fm. vorhanden sein. Alternativ könnte ein Teil der Gesamtverkürzung, die durch die Siglistorf Antiklinale kompensiert wird, auf Deformationsprozesse innerhalb des Grundgebirges zurückzuführen sein, was mit thick-skinned-Tektonik gleichzusetzen wäre.

Aufgrund der Messungen und Berechnungen der finiten Scherverformung der vorliegenden Studie ist es daher sehr wahrscheinlich, dass die Deformation des östlichsten Teils des Jura-Falten- und Überschiebungsgürtels durch eine Kombination aus thin-skinned- und später folgender thick-skinned-Tektonik erfolgte.

# Contents

# 1. Introduction

The Jura fold-and-thrust belt constitutes the outermost fold-thrust units of the Western and Central European Alps, developed during the Middle Miocene and Pliocene compression exerted by the Alps (Schori, 2021).

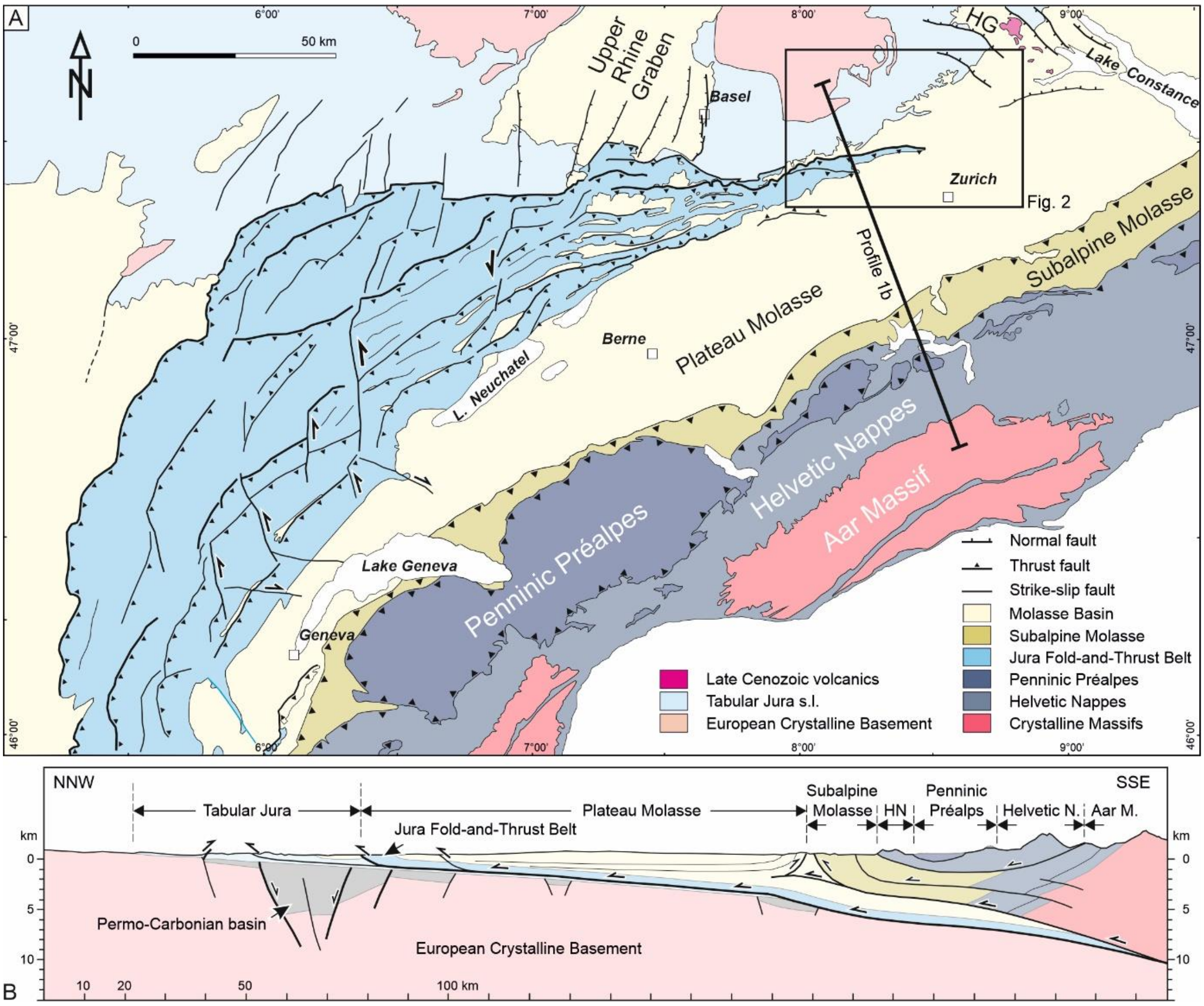


*Fig. 1: (a) Tectonic map of the Jura fold-and-thrust belt (modified from Malz et al., 2015 and Schori, 2021). (b) Profile 1b, geological cross-section (modified from Malz et al., 2015).*

Based on structural characteristics the Jura Mountains in the northern part of Switzerland can be separated into three main parts: the tabular Jura to the north, the deformed eastern tabular Jura ("Vorfaltenzone") in the middle and the folded Jura to the south. Adjacent to the folded Jura is the Plateau Molasse. Both the Molasse Basin and the Jura Mountains are part of the foreland fold-and-thrust belt formed in the late Miocene deformation zone of the alps (Rime et al., 2019)(Fig. 1).

In the Mesozoic, the areas later forming the Jura Mountains and the Molasse Basin where part of the European passive margin north and northwest of the Penninic Ocean. During that period of time approximately 2km thick sequences of limestones and marls in alternation were deposited (Sommaruga, 1997). In the Anisian evaporitic sequences of 40 to 150m thickness were deposited on this carbonate platform (Jordan, 2016). The clastic Molasse sediments were deposited in the Oligocene and Miocene and consist of fluvial, lacustrine and marine sediments in alternation, representing sea level fluctuations. The Mesozoic rocks are covered by the onlapping Molasse sediments, whereby the overall thickness of the sediments extents from 4km in the south to a couple of hundred meters in the north (Sommaruga, 1997).

Based on previous knowledge, the Jura Mountains were formed by "Fernschub", meaning by large-scale decoupling and detachment from the underlying basement units, in the Late Miocene to Pliocene. However, the mechanical feasibility of a large-scale décollement within the Triassic evaporites has led to many controversial discussions. The heterogeneity of the Triassic evaporites at any scales results in various rheological behaviors of layers, and therefore different rheological responses. While viscous flow may be a possible deformation mechanism in pure halite and anhydrite, pure shales and carbonates would rather deform in cataclastic flow. The variation of deformation mechanisms allows for the preservation of sedimentary structures, such as bedding or enterolithic faults. The deformation of the 150 to 300m thick Triassic evaporitic layers took place at depths of 1.5 to 6km at temperatures between 75°C to 150°C. The eastern part of the Jura fold-and-thrust belt accommodated a shortening of up to 16km, which is concentrated in the Triassic evaporites, at bulk strain rates varying between $5 \cdot 10^{-14} \cdot s^{-1}$ to $2 \cdot 10^{-13} \cdot s^{-1}$ (Jordan, 1992).

Thrust distances decrease from West to East finally dying out in the area northern of Zurich (Fig. 1). The study area is located almost at the most eastern tip of the fold-and-thrust belt equitable with no thrusting of the Jura floor thrust (Jordan, 1994) (Fig. 2).

The four bores recently drilled by NAGRA give the opportunity to analyse structures of the Zeglingen Fm. with regards to a possible large-scale decoupling or a lack thereof. The studied deep boreholes ("Tiefbohrungen") STA2-1, STA3-1, BUL1-1B and BAC1-1 are located in the Constance-Frick Trough in the "Vorfaltenzone" of Northern Switzerland at the edge of the Northern Alpine Molasse Basin (Fig. 3).

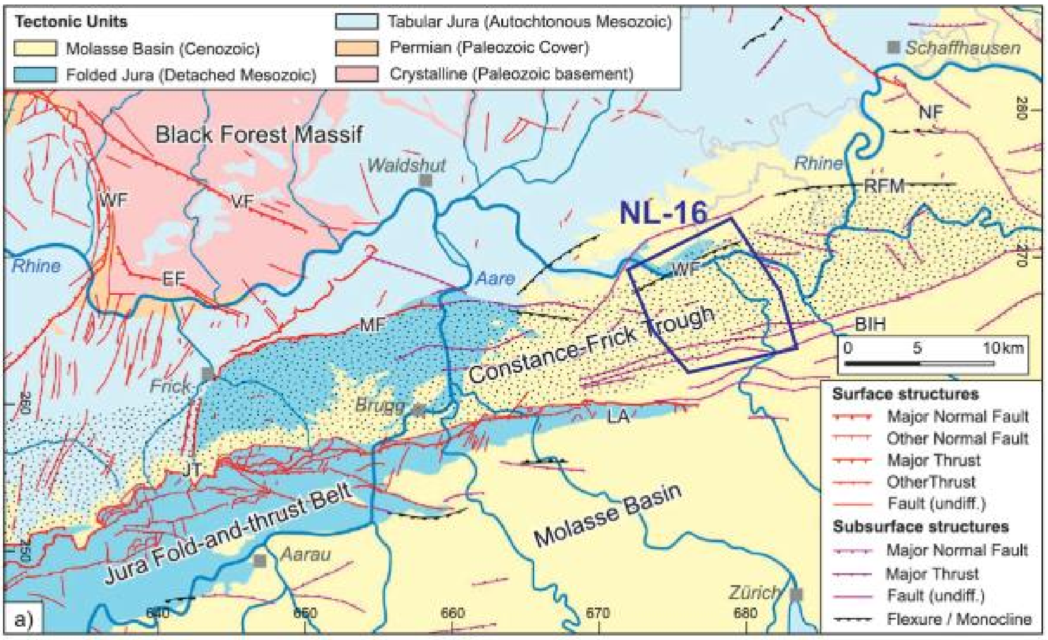


*Fig. 2: Tectonic sketch map of the Swiss Tabular Jura and the allochthonous Jura ("Folded Jura")(modified after Madritsch et al., 2018). Polygon labelled NL-16 indicates the location of the 3D-seismic "Noerdlich Laegern" where the investigated boreholes are located (see Fig. 3).*

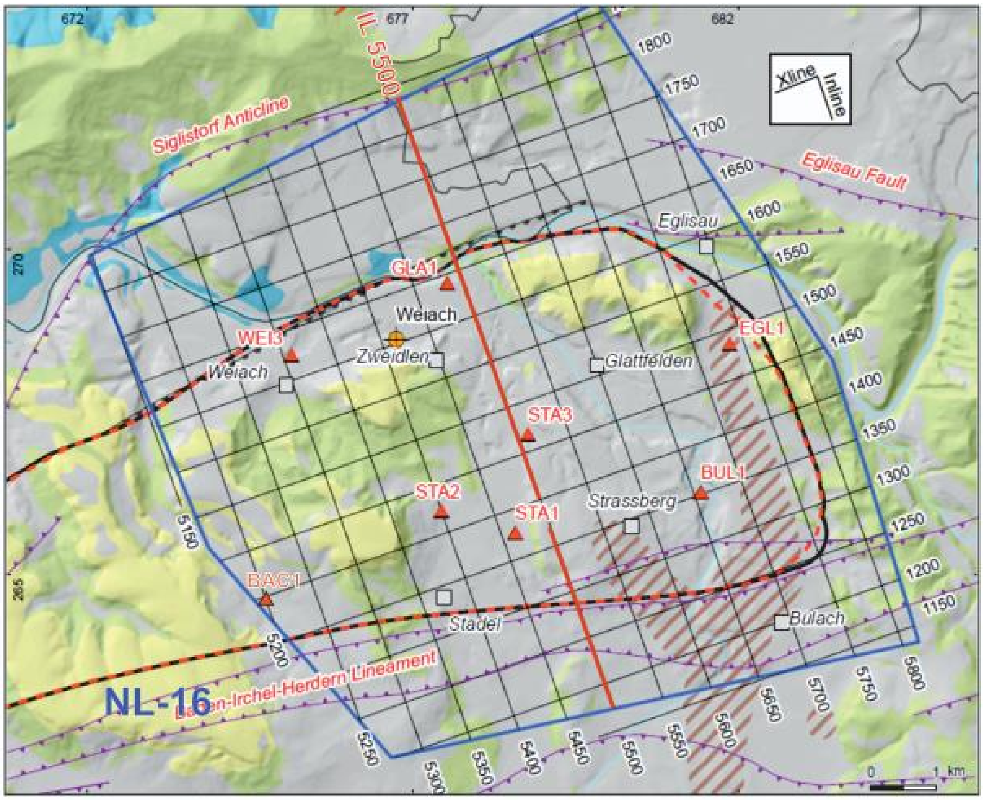


*Fig. 3: Location of the four studied deep boreholes (modified from NAGRA, 2019).*

## 1.1. Thick-Skinned vs. Thin-Skinned Tectonics

The terms thick- and thin-skinned tectonis are representative for the two endmembers of crustal shortening occuring in thrust belts of mountain ranges all over the world. Thereby thick-skinned refers to crustal shortening associated with an involvement of crustal scaled thrust faults, steepening with increasing depth, leading equally to a deformation of the basement and the sedimentary cover (Fig. 4, C; Coward, 1983). Thin-skinned style shortening on the other hand is characterised by deformed sheets overlying a basement unaffected by the shortening (Fig. 4, A). The thin-skinned fold-and-thrust belt and the basement are separated by a detachment horizon, which serves as a gliding surface for the sedimentary cover. Typical structures occuring in the folded sedimentary cover are conditioned by the thickness and type of the decollment layer and particularly by the mechanical contrast between the cover and the decollment layer (Pfiffner, 2016).

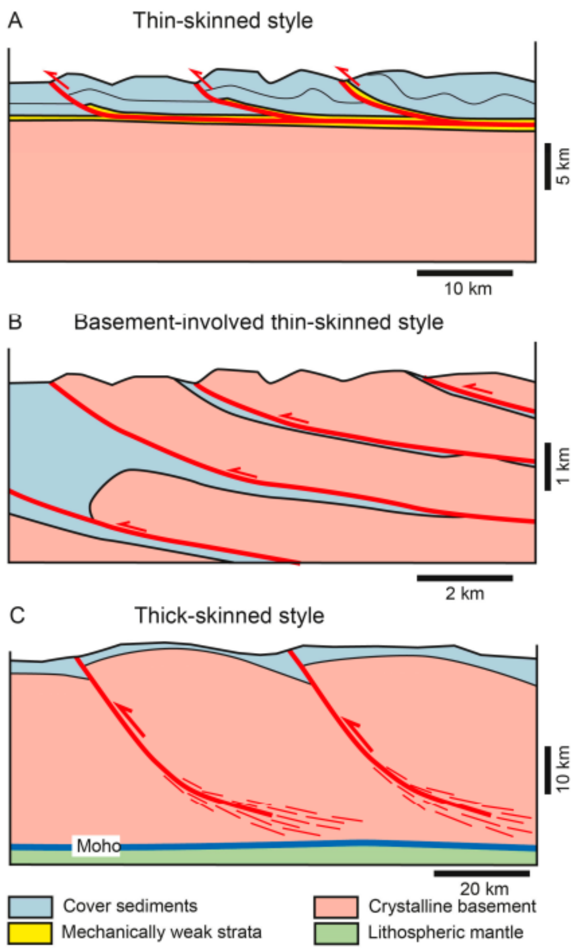


*Fig. 4: Schematic cross-sections: A) Thin-skinned tectonics, B) Thin-skinned tectonics with an involvement of the basement, C) Thick-skinned tectonics (Pfiffner, 2017).*

Transitions between thick- and thin-skinned tectonics are mostly characterised by thin-skinned tectonic behaviour with only thin slabs of crystalline basement rocks getting piled up into a nappe stack (Fig. 4, B; Pfiffner, 2016).

Different from the end members depicted in Fig. 4, deformation types in most mountain ranges are not uniform throughout the area and vary with the postition within the fold and thrust belt.

The main deformation processes which were active in the formation of the Jura Mountains were mostly interpreted as thin-skinned. Newer studys, however, suggest that the deformation should be seperated into two stages. The first and main stage of deformation covers the onset of the Jura fold-and-thrust belt formation by thin-skinned tectonics and ended appoximately 3.3Ma ago (Becker, 2020). The second stage refers to ongoing compressional tectonics at the northern front of the Jura Mountains during the Pliocene and Quaternary (Giamboni et al., 2004). Reflection seismic data of this area lead to the suggestion that this late or second stage deformation is dominated by thick-skinned tectonic processes (Madritsch et al., 2008).

Numerous studies made in the Jura Mountains point out the importance of pre-existing structures in the latter deformation processes of the fold-and-thrust belt (Homberg et al., 2002). Inherited basement faults in the crystalline basement underlying the Jura fold-and - thrust belt show structural orientations based on three Paleozoic trends associated with the Variscan orogeny: NNE-SSW striking sinistral shear zones, ENE-WSW striking dislocation zones and NW-SE striking dextral shear zones (Fig. 5). Vertical offsets of the basement and the cover, depositional differences of Mesozoic and Cenozoic sediments and mechanical heterogeneities in the deformed sediment can all be linked to these during the Mesozoic transpressionally or transtensionally reactivated faults (Schori et al., 2021).

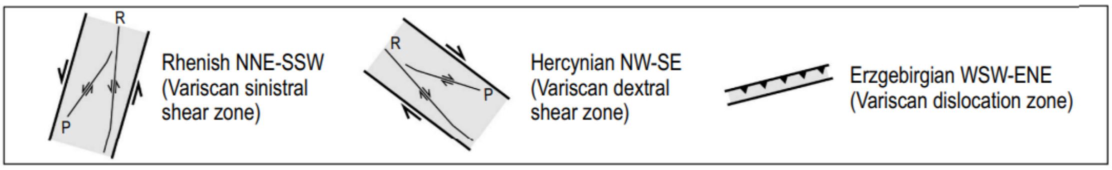


*Fig. 5: Main Paleozoic trends (modified after Schori et al. 2021).*

## 1.2. The Constance-Frick Trough

The Constance-Frick Trough (CFT) is a Late Paleozoic ENE-WSW striking basin located in Northern Switzerland, with its southern border roughly coincidising with the front of the Jura fold-and-thrust belt (Diebold & Noack, 1997).

Late Paleozoic basins developed after the planation of the Variscan Orogen due to crustal thinning and extension (Henk & Timmerman, 2005). The direct process which lead to the degradation of the orogen and the formation of basins is still a matter of controversy. Nevertheless the assumption that the impact of inherited fault systems on the process of basin formation is significant, is accepted by most authors (e.g., McCann et al., 2006; Ziegler & Dèzes, 2006). It is also considered that inherited faults had an influence on later tectonic events, and could be reactivatd in the present-day tectonic regime (e.g., Madritsch et al., 2008; Mosar, 1999).

Recent studies focused on the structure and the kinematic to develop an improved model of the Constance-Frick Trough. The CFT is characterised by opposing half-graben geometries and can therefore be parted into an eastern and a western segment. The segments are separated by a NW-SE trending transition zone. Based on seismic studies the western segment reaches depths of up to 5km, whereas the eastern segment is shallower with approximate depths between 1600 and 2000m. The western part of the CFT is characterised by a distinct half-graben geometry, which could possibly be a result of a low-angle detachment fault being active during trough formation. The CFT may also be related to a deep-seated listric detachment fault at the border to the Black Forest Massiv. The reactivation of such a crustal-scale fault in Neogene, could have led to a propagation of deformation underneath the décollement of the Jura fold-and-thrust belt, inferring thin-skinned deformation with basement involvement (Lacombe & Bellahsen, 2016; Pfiffner, 2016). Both 2D seismic reflection and outcrop-scale structures underline the importance of preexisting Late Variscan faults in Neogene reactivation scenarios (Madritsch et al., 2018).

## 1.3. Lithostratigraphic and lithological context based on BUL1-1B

The following description of occurring lithologies in the cores of BUL1-1B are based on the model presented by Jordan et al. (2021) (Fig. 6). The described succession is representative for the other boreholes described in this master thesis.

### 1.3.1. Quaternary

The uppermost 5m consist of polymict, subangular to well rounded, poorly sorted gravel and components of anthropogenic origin such as bricks, tiles and glass. The colour of the soil variies between yellowish to dark grey with brownish undertones. The section below of approximately 20m thickness consists mainly of polymict, light grey to pale yellow gravel, sand and sporadic blocks. The lowermost quaternary section is made up of polymict gravel (same properties as in the previous section) and blocks that show glacial striation.

### 1.3.2. Paleogene/Neogene

*Lower Freshwater Molasse Group (36.00-502.00m)*

The group can be subdivided into five different litholgies which are present in variable abundances. The first lithologie is medium to coarse grained sandstone of light beige to leight grey/whitish colour. The main components are quartz and feldspar of various colours and transparency. Minor components are hornblende and garnet. This rock type is refered to as "Granitischer Sandstein" and is generally interpreted as a river channel deposit. Fine grained silty sandstone which consists predominantly of quartz, feldspar and fine grained mica builds the second lithology. The colour ranges from grey to beige to reddish grey. The third occuring lithology is claystone of varoious colours. Splintery limestone and crumbly limestone are the fourth and fith lithology respectively.

Lithologies 2 to 5 are representative for four different facies outside of the channels, e.g. floodplain sediments.

*Siderolothic Group (502.00-504.00m)*

The Siderolithic Group is characterised by the appearance of iron-pisoids ("bohnerz") along with large, isolated transparent quartz grains.

### 1.3.3. Late Jurassic

*Malm Group (504.00-805.28 m)*

The Malm Group can be subdivided into four formations: Felsenkalke/Massenkalke (504.00-653.57m), Schwarzbach Formation (653.57-676.58m), Villigen Formation (676.58-751.11m), and Wildegg Formation (751.11-805.28m).

The Malm Group consists mainly of thin to thick bedded limestone of various colours and intervals of calcareous and argillaceous marls. The limestones are often internally laminated or contain interlayers of clay. The occurence of chert nodules, fossils and macrofossils (bivalves, sponges, brachiopods, belemnites and crinoids), pyrite, glauconite, silt and sandstones allows for a distinguishment into the four formations mentioned above.

### 1.3.4. Middle Jurassic

*Dogger Group (805.28-995.85m)*

The Dogger Group consists of eight lithostratigraphic units: Wutach Formation, Variansmergel Formation, Parkinsoni-Württembergia-Schichten, Herrenwis Unit, Humphriesioolith Formation, Wedelsandstein Formation, Murchisonae-Oolith Formation and Opalinus Clay.

The Wutach Formation is a thin layer of a continous iron-oolite bed and represents the boundary to the overlaying Malm. The Variansmergel Formation consists of an alternation of silty marl and limestone beds and is characterised by the abundant occurance of fossils. The Parkinsoni-Württembergia-Schichten are build up from thick successions of argillaceous marl with thin iron-oolitic interbeds. The Herrenwis Unit is a sedimentary unit consisiting mainly of coral bioherms, crinoidal limestone and reef detritus. The Humphriesioolith Formation is a thin succession represented by limonitic to iron-oolitic beds. The Wedelsandstein Formation is predominantly build up from silty claystone and limestone which allows for a separation into two shallowing upward cycles. The Murchisonae-Oolith Formation is characterised by the occurance of two iron-oolithic sections which are seperated by silty claystone. The Opalinus Clay is a relatively monotonous succession of dark gray silty claystone and can be subdivided according to the existence and type of interbeds.

### 1.3.5. Early Jurassic

*Lias Group (995.85-1030.51m)*

The Lias Group consists of the Staffelegg Formation which can be split into several members of various thickness: Gross Wolf Member, Rietheim Member, Breitenmarr and Rickenbach Members, Grünschholz Member, Frick Member, Beggingen Member and Schambelen Member.

Even though the Staffelegg Formation is dominatd by limestone and marl (argillaceous, dolomitic and calcareous), it is also characterised by its heterogeneity. The different members are mainly distingished by their carbonate, bitumen and phosphorus content and the occurance of fossils, nodular limestones and iron-oolithic beds.

### 1.3.6. Late to Middle Triassic

*Keuper Group (1030.51-1132.00m)*

The Keuper Group is subdivided into two formations, each consisting of several Members.

The Klettgau Formation is mainly characterised by its dominance of variegated playa sediments with fine to coarse grained siliciclastic or calcareous sediments in overspill layers and channels. The Gruhalde Member, the Seebi Member, the Gansingen Member and the Ergolz Member are part of the Klettgau Formation. The differentiation into the different members is primarly based on coulour variations, erosional surfaces, lithoclasts and inclusions.

The Bänkerjoch Formation consists of evaporites displaying both complete as well as incomplete cycles and subcycles. The evaporitic sequences are interrupted by dolomitic marl, sulphate sediments, sandstone and dolostone (Dronkert et al., 1990). By now, a formal subdivision of the Bänkerjoch Formation is not existent.

### *Muschelkalk Group (1132.00-1306.17m)*

The Muschelkalk Group contains three formations: the Schinznach Formation, the Zeglingen Formation and the Kaiseraugust Formation. Each of the formations can further be divided into several members of various thickness.

The primarly lithologies of the five members of the Schinznach Formation are variegated limestone and dolostone, whereas the division between members is based on erosional surfaces, fossils, microstructures and bitumen and clay content.

The Zeglingen Formation can be subdivided into four informal units (cf. Jordan & Deplazes 2019): the Dolomitzone, the Obere Sulfatzone, the Salzlager and the untere Sulfatzone. The sections are mainly build up of dolomite, anhydrite, claystone and rock salt, which occur both, in alternating beds as well as massive layers. The differentiation between the units is based on their lithology.

In the Kaiseraugust Formation we can distinguish between three informal units based on informal marker beds (cf. Jordan & Deplazes 2019): the Orbicularismergel, the Wellenmergel and the Wellendolomit. The units mainly consist of dolostone, which can be partly bituminous, anhydrite, shale, argillaceous marl and limestone. They are also characterised by the abundant occurance of various fossils.

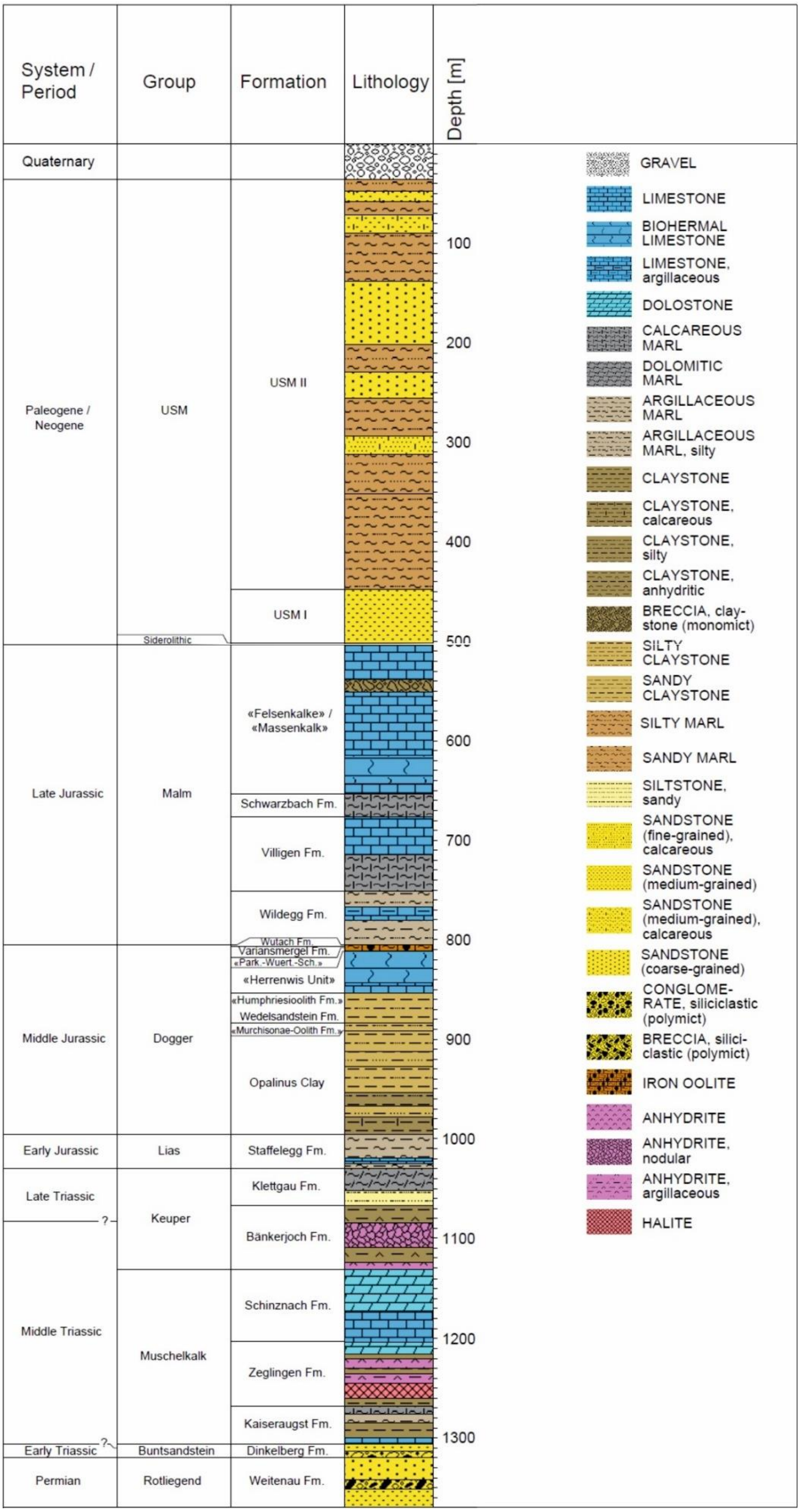


*Fig. 6: Lithostratigraphic profile of BUL1-1B (modified after Ammen & Palten, 2021).*

### 1.3.7. Early Triassic

*Buntsandstein Group (1306.17-1319.63m)*

The Buntsandstein Group consists of the Dinkelberg Formation wich is subdivided into three units: the Plattensandstein, the Karneolhorizont VH2 and the Vogesensandstein. They consist of pooly sorted sandstone, conglomerate, lithoclasts and argillaceous matrix. The coulour of the different sandstones varies from greenish gray, white and yellow to greyish violet.

### 1.3.8. Permian

*Permo-Carboniferous Sedimets (1319.63-1370.19m)*

The Permo-Carboniferous Sediments of the Weitenau Formation can be parted into several levels based on lithology. They consist mostly of sandstone, showing crossbeding and lamination and fanglomeratic sediments, deposited in grading upward cycles.

## 1.4. The Zeglingen Formation

The Zeglingen Formation functioned as the main detachment horizon of the Jura fold-and-thrust belt (Jordan & Deplazes, 2019). All structures recorded and described in the course of this master thesis are located within the "Salzlager" of the Zeglingen Formation.

The Zeglingen Formation further known as "Anhydritgruppe" ("Mittlerer Muschelkalk") consists of Anisian evaporitic sequences, deposited on the northern Tethyan carbonate platform in a transgressive-regressive megacycle (Jordan, 2016; Dronkert et al., 1990). The formation consists of four subdivisions referred to as "Untere Sulfatzone", "Salzlager", "Obere Sulfatzone" and "Dolomitzone" (Widmer, 1991). The overall thickness of the formation varies between 40 to 150m (Jordan, 2016), whereas the rock salt deposits of the "Salzlager" are only present in an area northwest of the line Bern-Zurich-Schaffhausen (Jordan, 2016; Bock & Simon, 2009) (Fig. 7).

The "Dolomitzone" is build up from beige-grey to dark beige, predominantly laminated dolostone, which shows bioturbation. Chert nodules with average sizes increasing with depth aswell as anhydrite nodules occur (Jordan & Deplazes, 2019; Jordan et al., 2021; Jordan et al., 2022; Jordan et al., 2023).

The "Obere Sulfatzone" can be further separated into several sections which are either dominated by dolostone, anhydrites, claystone or an alternation of thin layers of dolostone, anhydrite and claystone. The dolostone sections consists of a thin- to medium-bedded alternation of dolostone with anhydrite nodules and nodular beds occurring in different thicknesses and sizes. Chert nodules may also occur at different levels of the section. The anhydrite section is characterised by an alternation of argillaceous, massive and laminated anhydrite. Folds generated by diagenetic processes may be observable within this section. The section dominated by claystone consists of an alternation of claystone and dolostone with small anhydrite nodules within the claystone. The dolomitic sequences can be brecciated and often show a fine lamination (microbial mats). Folding can also be observed within this section. The last section consists of an alternation of thin layers of anhydrite, dolostone and claystone, interrupted by anhydrite with chicken wire texture and massive anhydritic sections. Various deformation structures can be seen in this section, including brecciation, thrusting and chaotic folding (Jordan et al., 2021; Jordan et al., 2022; Jordan et al., 2023).

The "Salzlager" consists of massive rock salt in variable colours from light pink, to nearly colourless, to orange-red. The grain size of the salt varies between fine grained to coarse grained, with large xenomorphic crystals. Interclasts of various sizes and densities are embedded within the salt. The interclasts consist mostly of fine-layered alternations of claystone and anhydrite. The salt to interclast ratio varies within the section to an extent where the volume of interclasts exceeds the volume of rock salt (Jordan et al., 2021; Jordan et al., 2022; Jordan et al., 2023).

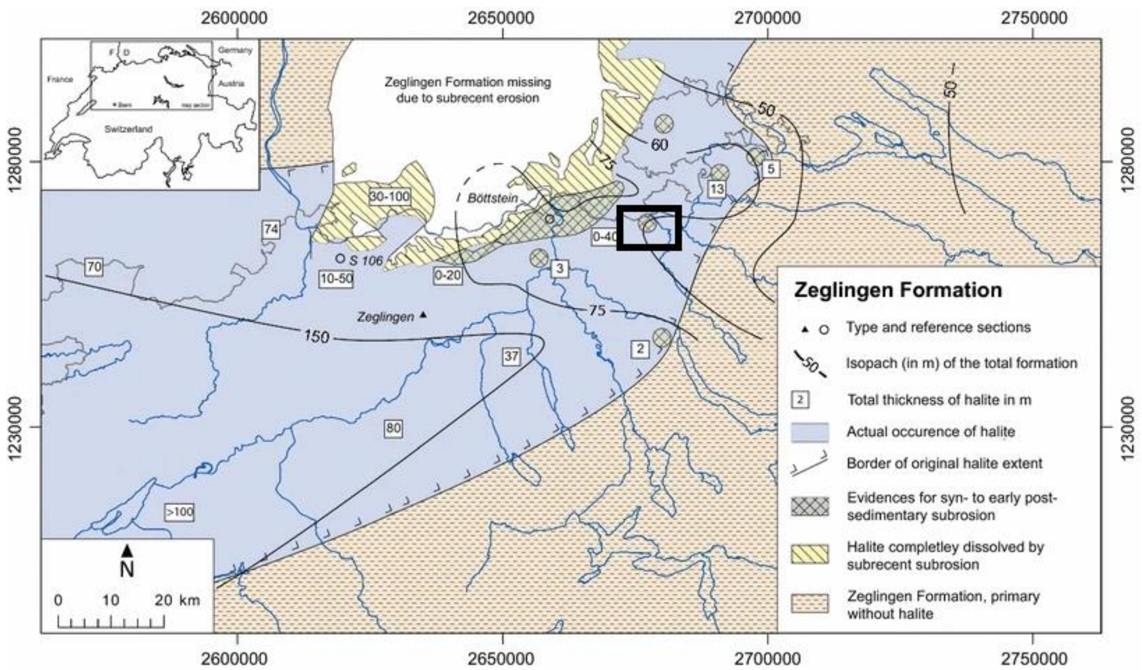


*Fig. 7: Isopach and facies map of the Zeglingen Formation (Jordan, 2016). Rectangle indicates the location of the study area.*

The "Untere Sulfatzone" can be parted into two sections. The first section is characterised by a fine layered alternation of claystone, anhydrite and massive anhydrite. Orange to milky white halite can be found in veins and pores. The section shows various signs of deformation, such as brecciation, both chaotic and geometric folding and thrusting. The second section consists mostly of pure white anhydrite, showing early diagenetic deformation structures (Jordan et al., 2021; Jordan et al., 2022; Jordan et al., 2023).

## 2. Methodology

In the years between 2019 and 2022 the National Cooperative for Radioactive Waste Disposal (Nagra) drilled four boreholes in siting area Noerdlich Laegern which penetrate the evaporitic succession of the Zeglingen Fm. The relevant sections of the thereby obtained cores were examined in person within two 1-week trips in the Nagra core storage facility Würenlingen.

The lithologies and structures of the core were analysed. Structures that allow conclusions to be drawn about kinematics and strain were particularly focused on. During the recording process, detailed photographs of the lithology and structures were taken and later used to obtain further information about the strain.

Immediately after core retrieval all Nagra cores were marked with so-called core orientation lines (red and yellow) parallel to the core axis. During the subsequent core analyses most of the cores of the boreholes BUL1-1B, BAC1-1, STA2-1 and STA3-1 have been oriented by matching structures observed in the core with structures identified in oriented pictures of the borehole wall using a workflow described in Nagra (2021a, 2022 a-c). For the matched core section the orientation of the red core orientation line was noted as the reference orientation for structural analyses, allowing for an oriented measurement of occurring structures. Therefore, the up to 1m long core sections were put in a goniometer and rotated until the red core orientation line pointed to the correct direction (Fig. 8). Dip and dip direction of structures were measured with a geological compass. Obtained measurements were then plotted in Schmidt net stereographic projections and used for structural interpretations.

*Fig. 8: Left: Measurements of core structures with a geological compass. The core was oriented according to core orientation lines in the goniometer. Right: Laid-out cores in the Nagra core storage facility Würenlingen.*

Based on occurring structures such as boudins or winged inclusions an estimation of strain was obtained and represented graphically as strain profiles.

To gain exact information about the mineralogical content 22 rock samples were collected from different depths and analysed via X-ray powder diffraction. Based on mineralogical content, grain size and degree of viscous deformation, a rough division of occurring lithologies was made. Obtained information was then visualised in lithological plots for the four analysed bores. A model explaining the evolution of the halite succession was also elaborated.

## 2.1. Drill data

In the course of this master thesis the "Salzlager" unit of the Zeglingen Fm. was studied in the cores of the four boreholes STA2-1, STA3-1, BUL1-1B and BAC1-1. Borehole data and thickness of the respective "Salzlager" unit are displayed in Table 1.

*Table 1: Borehole location and structural data base (Nagra 2021a, 2022a, 2022b, 2022c). *m below ground level*

| borehole | coordinates LV95 | drilling period | final depth [m] | core depth of Zeglingen Fm. [m] | core depth of "Salzlager" [m] | thickness of "Salzlager" [m] |
|---|---|---|---|---|---|---|
| STA2-1 | 2'677'447.617/ 1'265'987.019 | 25.01.2021-08.07.2021 | 1288.87 | 1116.01-1184.72 | 1151.45-1178.88 | 27.43 |
| STA3-1 | 2'678'792.885/ 1'267'161.988 | 17.12.2020-07.07.2021 | 1280.88 | 1099.03-1178.43 | 1135.31-1174.87 | 39.56 |
| BUL1-1B | 2'681'446.028/ 1'266'298.472 | 15.04.2019-27.11.2019 | 1370.19 | 1204.73-1267.94 | 1245.50-1260.31 | 14.81 |
| BAC1-1 | 2'674'769.089/ 1'264'600.698 | 10.09.2021-23.04.2022 | 1306.26 | 1125.75-1202.03 | 1160.56-1195.79 | 35.23 |

## 2.2. Structures

During the recording of the "Salzlager" unit of the cores, structures that allow conclusions to be drawn about kinematics and strain were particularly focused on.

### 2.2.1. Boudins

Boudins are structures formed in an extensional regime. The term boudinage describes the formation process of these extensional structures by layer parallel extension of originally continuous layers (Fossen, 2010).

Besides boudins so called pinch-and-swell structures may form in an extensional stress regime under layer parallel-extension, in a process referred to as necking. As the name implies pinch-and-swell structures are characterised by the typical pinch and swell features of an extended competent layer. Contrary to boudins the single pinch-and-swell pieces are still connected at the swell-parts, so called necks, by various extents (Gardner et al., 2016).

Boudins are separate fragments of a former single competent layer, extended by brittle or ductile deformation mechanisms or a combination of both. The matrix surrounding boudins compensates stress by ductile deformation.

Individual boudins can either be separated by extension, shear fractures or narrow shear bands. Shear fractures may be asymmetrical or symmetrical (Goscombe et al., 2004). The appearance of boudins differs depending on the fracture type separating individual boudins and on the predominant deformation mechanism (Fig. 9) (Fossen, 2010).

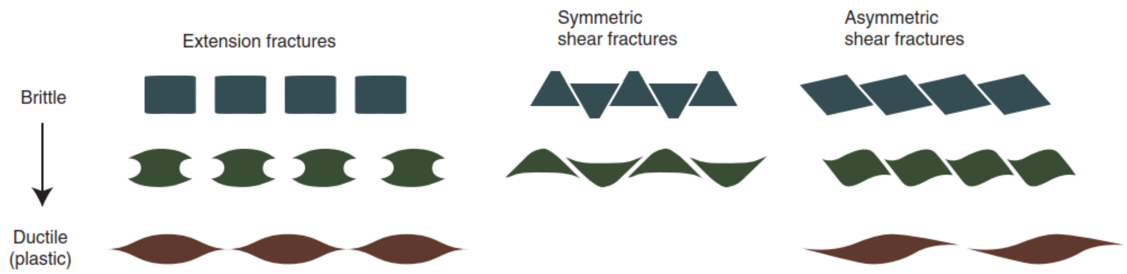


*Fig. 9: Geometry of boudins (Fossen, 2010).*

Boudins may be characterised by their length, width and the separation length between individual boudins. Other than boudin ratios, the separation length is mostly dependent of strain, especially of layer-parallel extension. The separation is not influenced by the viscosity contrast of boudins and the adjacent matrix. The aspect ratio of boudins is characteristic with ranges between 2-4. Further extension will only result in higher separation lengths with consistent boudin aspect ratios (Fossen, 2010).

Non-viscosity-contrast (non-rheology-contrast) dependant boudinage may also occur in foliated rocks and is referred to as foliation boudinage (Platt & Vissers, 1980; Hambrey & Milnes, 1975). At veins, which are often set at high angles to the foliation plane, the foliation gets defflected, formig structures similar to boudin necks (Arslan et al., 2008).

The change of length of the former continuous layer through boudinage can be referred to as stretching or elongation. Stretch or one-dimensional strain e or ε is defined through the relationship $\varepsilon=(l-l_0)/l_0$), where $l_0$ is the length before and l is the length after extension (Fossen, 2010) (Fig. 10).

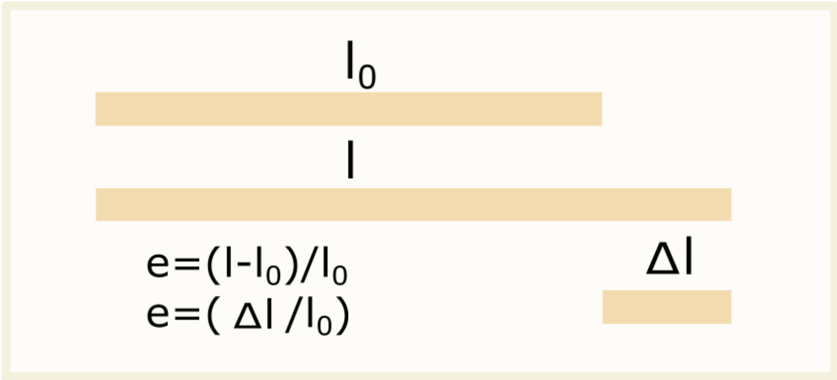


*Fig. 10: Relationship of one-dimensional strain with length before and after deformation.*

### 2.2.2. Winged inclusions

The rework of natural pinch-and-swell structures in simple shear deformation may result in structures, visually resembling delta clasts, so called winged inclusions (Hanmer & Passier, 1991; Hanmer, 1990). Newer studies suggest that the pre-existing core and wings of pinch-and-swell structures rotate out of the shear plane thereby forming winged inclusions. The rotation rate is significantly influenced by the shape of the winged inclusions, the viscosity ratio and the stress exponent (Grasemann & Dabrowski, 2014).

While winged inclusions and delta clasts undergo different development paths, they may visually resemble at some stages of deformation. The main difference between delta clasts and winged inclusions is the position of the wings during the rotation of the core. While for winged inclusions the pre-existing wings rotate along with the core (Hammer & Passier, 1991), the wings of the delta clasts forming at the expense of the core during shearing, stay on the original side throughout the whole rotation process (Fig. 11, a) (ten Brink & Passchier, 1995; Bons et al., 1997; Mandal et al., 2000).

During the rotation process the aspect ratio of winged inclusions decreases thereby influencing the overall rotation rate. The wings rotate at different rates along with the core passing through the field of instantaneous shortening where they may undergo folding. While passing through the field of instantaneous stretching these ptygmatic folds may unfold which results after a rotation of 180° again in a pinch-and-swell structure (Fig. 11, c). Therefore, winged inclusions record equivocal information about the finite strain (Grasemann & Dabrowski, 2014).

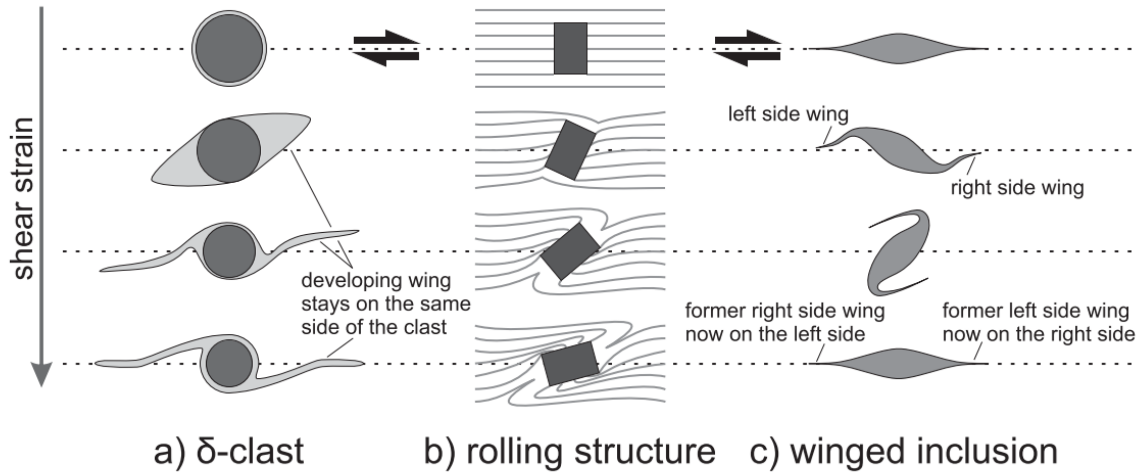


*Fig. 11: Visualisation of different rolling objects undergoing progressive shear (Grasemann & Dabrowski, 2014 and references cited therein).*

Grasemann & Dabrowski (2014) developed a high-strain numerical model for pinch-and-swell structures undergoing simple shear deformation using a two-dimensional finite-element model. The model takes two gaussian curves *c* which enclose the pinch-and-swell object and the viscosity contrast of the object and the surrounding matrix *m* into account, while the shear rate is set to 1 (Fig. 12).

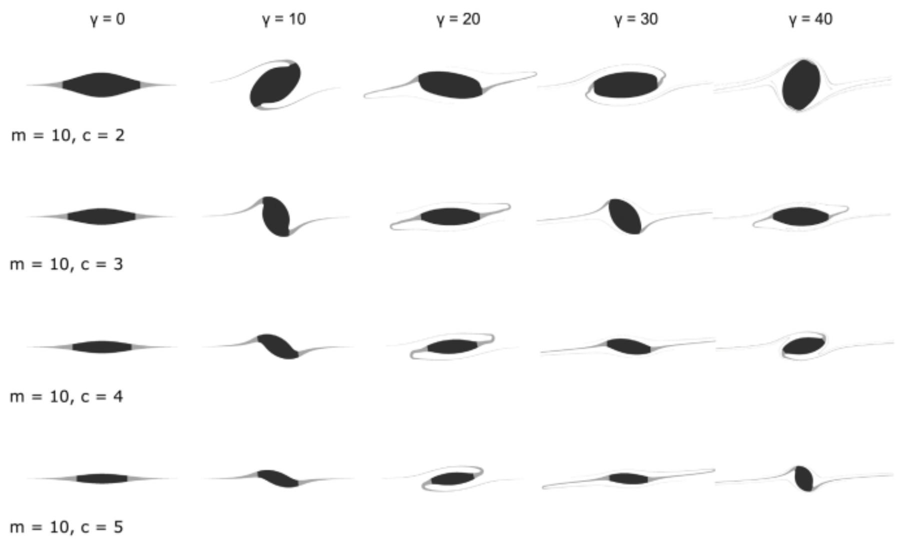


*Fig. 12: Visualisation of the results of 4 linear viscous models with initial shapes c ranging between 2 to 5 and the viscosity ratio of the inclusion and the surrounding matrix m set at 10 (Grasemann & Dabrowski, 2014).*

### 2.2.3. Survivor grains and sigmoids

Survivor grains are rounded, isolated clasts, which escaped the grain size reduction processes and are embedded in a matrix of commuted parent rock. They can be randomly orientated or develop a shape preferred orientation often aligned with the foliation of the surrounding matrix (Cladouhos, 1999). It is assumed that survivor grains develop in mylonites due to their higher resistance to dynamic recrystallisation and deformation than their adjacent matrix (Hanmer, 1990).

Mylonites are foliated rocks resulting from dominantly ductile deformation. Plastic strain and breakage lead to a grain size reduction and thereby the development of a foliation. Through ongoing plastic deformation grain aspect ratios of the grains building the matrix increase. Porphyroclasts resist ductile deformation and remain significantly larger than the grains of the surrounding matrix. During the process of mylonitisation porphyroclasts steadily decrease in size due to fracturing or marginal erosion. The differentiation of mylonites into three main classes (protomylonite, mylonite and ultramylonite) is based on the volume percent of porphyroclasts (Sibson, 1977; Robertson, 1999). The amount of porphyroclasts within mylonites can be equated to the degree of deformation and strain, meaning protomylonites experienced less deformation than ultramylonites (Fossen, 2010).

### 2.2.4. Shear bands

Shear bands are three-dimensional zones in which deformation is localised and concentrated. The thickness of shear bands is related to the particle size and can be 10 to 30 times greater than the mean particle size (Kuhn, 2017). In homogeneous materials shear band growth is mainly controlled by strain rates and temperature (Mukhopadhyay et al., 2022). Shear bands often can be used as kinematic indicators (Fossen, 2010).

Former layers or clasts, dissected and displaced by shear bands, thereby forming strain markers make a direct measurement of the offset across the shear band feasible and therefore allow quantifying the shear strain (Fossen, 2010). Assuming simple shear, strain $\gamma$ can be defined as the tangent of the shear angle $\psi$ (Fig. 13) (van der Pluijm & Marshak, 2004).

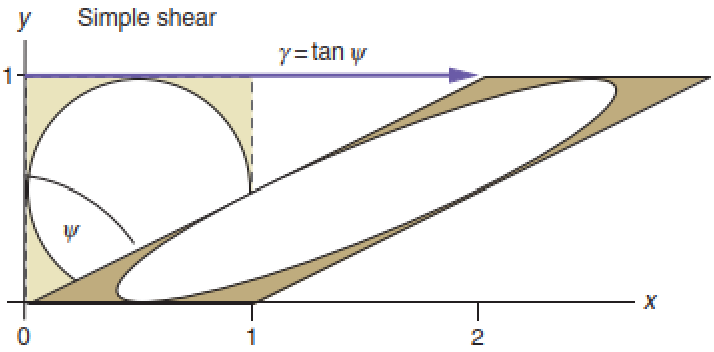


*Fig. 13: The concept of simple shear deformation (Fossen, 2010).*

### 2.2.5. S-C-Mylonites

The accumulation of strain can lead to the formation of narrow shear bands or slip surfaces parallel to the margin of the shear zone, called C. The foliation S is influenced by these small-scaled shear zones and curves into and out of them. The sense of the deflection of the curved foliation reflects the shear sense of the entire shear zone (Fig. 14). The angle between S and C usually varies between 25°- 45°. For high shear strain (above 10) the angle between S and the shear zone gradually decreases until S and C align thereby building a composite foliation. Higher shear strains subsequently lead to the formation of a new set of shear bands, oblique to the shear zone margins (Fossen, 2010).

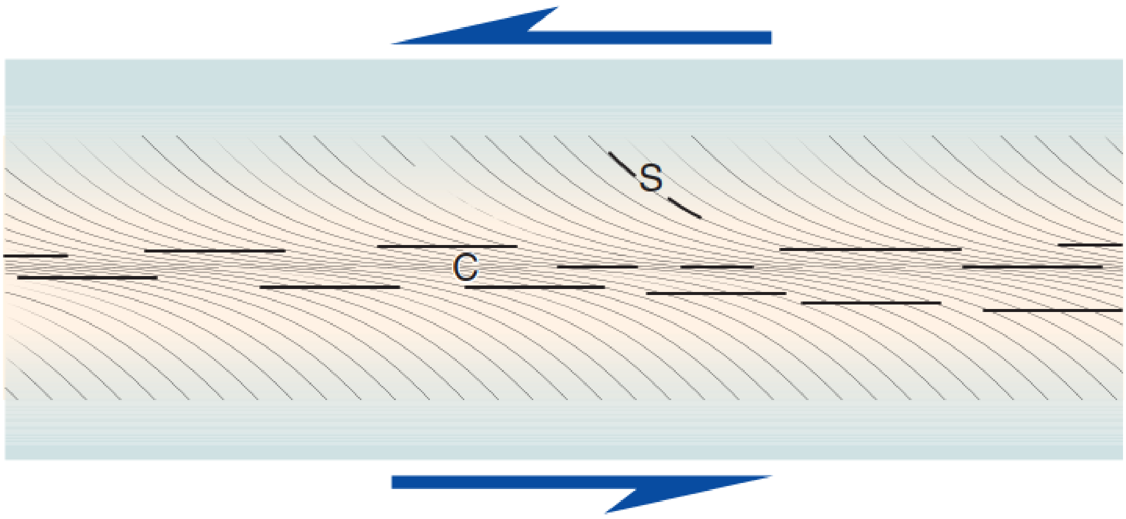


*Fig. 14: Schematic illustration of a S-C pattern in a dextral shear zone. C are shear zone surfaces parallel to the shear zone margins. S is the new-formed foliation which gets cut by C (modified after Fossen, 2010).*

### 2.2.6. `V´-pull-aparts

`V´-pull-apart structures are a result of rigid-body rotation of one fragment relative to another fragment of the originally same clast and occur beside active shear planes. Their structure is characterised by v-shaped gaps occurring due to the development of asymmetric pull-apart microstructures within the clast. The overall shear sense can be derived from the asymmetry of `V´-pull-aparts. The fracture wall which is at lower angle to the shear plane indicates which fragment has rotated synthetically with respect to the adjacent shearing (Fig. 15, Hippertt, 1993).

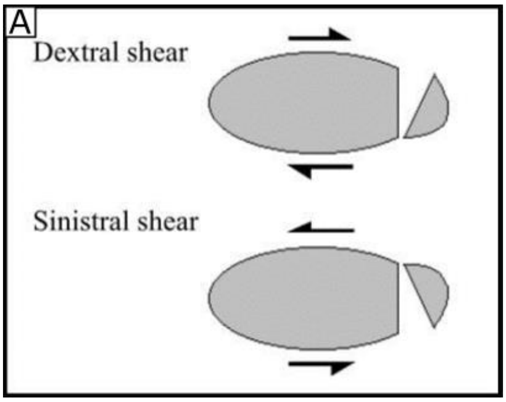


*Fig. 15: : Development of `V´-pull-aparts in dextral and sinistral shear (Samanta et al., 2001 after Hippertt, 1993).*

## 2.3. Mineralogical composition

The determination of the mineralogical composition was carried out via X-ray powder diffraction. Therefore 22 samples collected from different depths of the 4 cores were pulverised and analysed. The collected samples were roughly crushed with a geological hammer and afterwards pulverised in a rock mill and an agate mortar. Thereby the total amount of time spend in the rock mill varied greatly between the samples. A few grams of the pulverised material were transferred to the unit cells and analysed in the X-ray diffractometer of the University of Vienna. X-ray powder diffraction is based on Bragg's law. Peaks only result from constructive interferences of monochromatic X-rays when these X-rays hit the crystal lattice at a specific angle theta. The angle at which X-rays hit the surface of the pulverised sample varies during the measurement period resulting in a characteristic diffraction pattern. In order to assign measured peaks to specific minerals, the diffraction patterns were afterwards compared with a database.

# 3. The Halite Succession

Based on the lithological and structural information obtained in the core analysis process of the four bores a model presenting a possible development of the evaporitic succession was elaborated. Both the lithological content and the intensity of viscous deformation have been incorporated into the model presented in the following chapter.

## 3.1. Main lithotypes of the "Salzlager" of the Zeglingen Formation

### 3.1.1. Undeformed anhydrite and clay

Undeformed anhydrite and clay layers still show sedimentary structures like bedding, laminae or ripples. Anhydrite slumps, with erosional surfaces on top proving their syn-sedimental origin, are preserved. Undeformed Hopper crystals can be seen in some parts of the undeformed anhydrite sections. Undeformed isometric clay and anhydrite grains can be observed at bedding-parallel core cuttings (Fig. 16).

### 3.1.2. Deformed anhydrite and clay layers

Anhydrite and clay layers are not solely undeformed as comparably small parts of the sections show signs of deformation. Sedimentary structures are still visible, but some layers are cut by tension gashes and boudins. Halite has partly crystallised in necks between boudins. At bedding-parallel core cuttings clay and anhydritic grains are no longer isometric but slightly elongated (Fig. 17).

### 3.1.3. Authigenic halite breccia

Authigenic halite breccias are build up from anhydrite and claystone clasts and authigenic halite which grows in and between these clasts. The extend of halite growth and therefore the clast to halite ratio varies within the breccia. Parts of the breccia contain practically no authigenic halite growth (Fig. 18, B), whereas other sections equally consist of halite and anhydrite clasts and/or claystone clasts (Fig. 18, C, D) or are even dominated by growing halite (Fig. 18, A). The clasts mainly consist of layered anhydrite and clay and are not affected by viscous deformation, therefore sedimentary structures as laminae or ripples are still preserved. Between the undeformed anhydrite and claystone layers halite begins to grow. At the start of the growth process, when the layers are still close together, halite grains are elongated to fibrous and the growing direction of halite is observable. In most cases halite growth is vertical to the anhydrite and claystone layering. With higher distances between clasts it gets more difficult to identify the growing direction, as halite grains appear to get more isometrical the farther away they are from clasts. Grain sizes range from mm to a couple

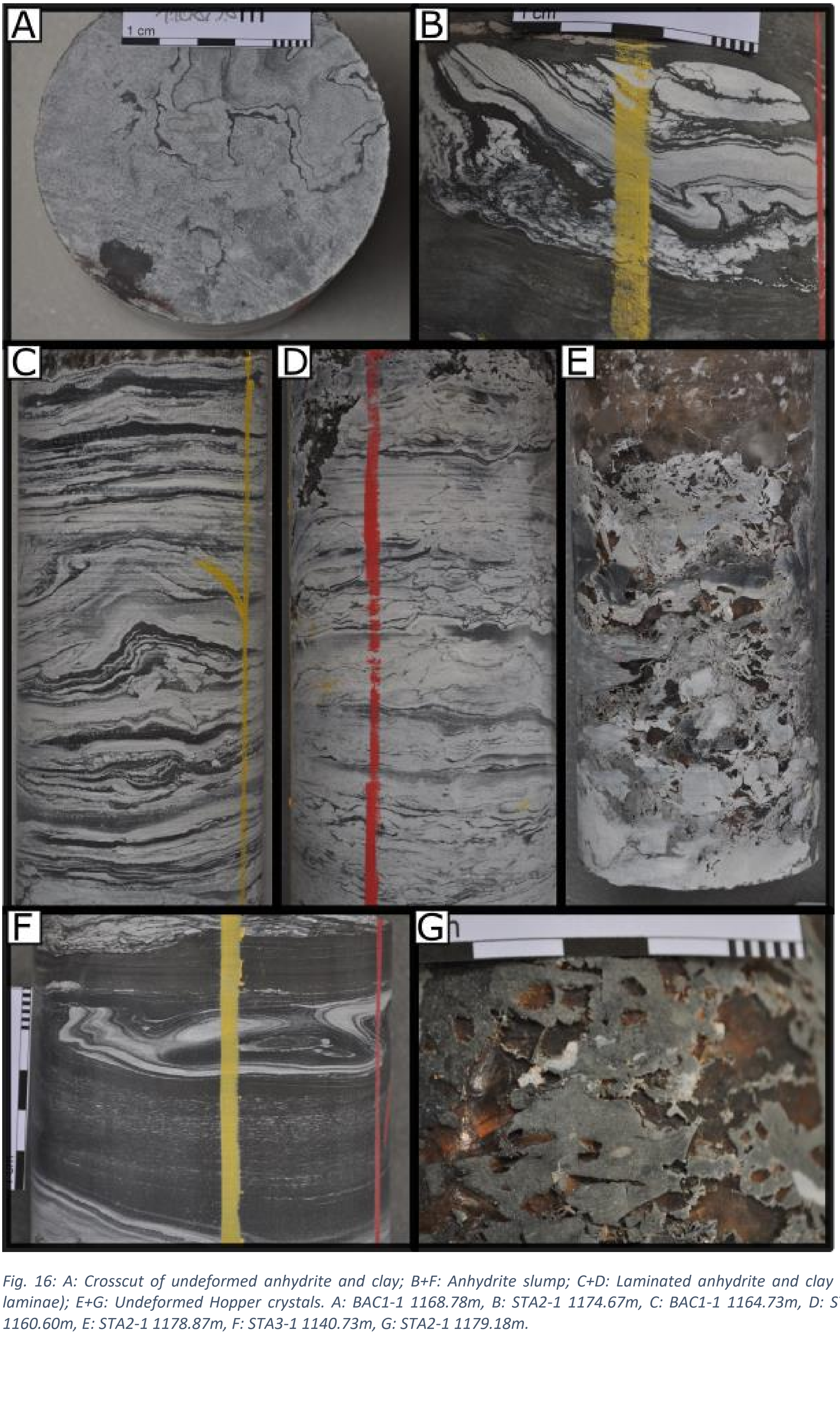


*Fig. 16: A: Crosscut of undeformed anhydrite and clay; B+F: Anhydrite slump; C+D: Laminated anhydrite and clay (algal laminae); E+G: Undeformed Hopper crystals. A: BAC1-1 1168.78m, B: STA2-1 1174.67m, C: BAC1-1 1164.73m, D: STA2-1 1160.60m, E: STA2-1 1178.87m, F: STA3-1 1140.73m, G: STA2-1 1179.18m.*

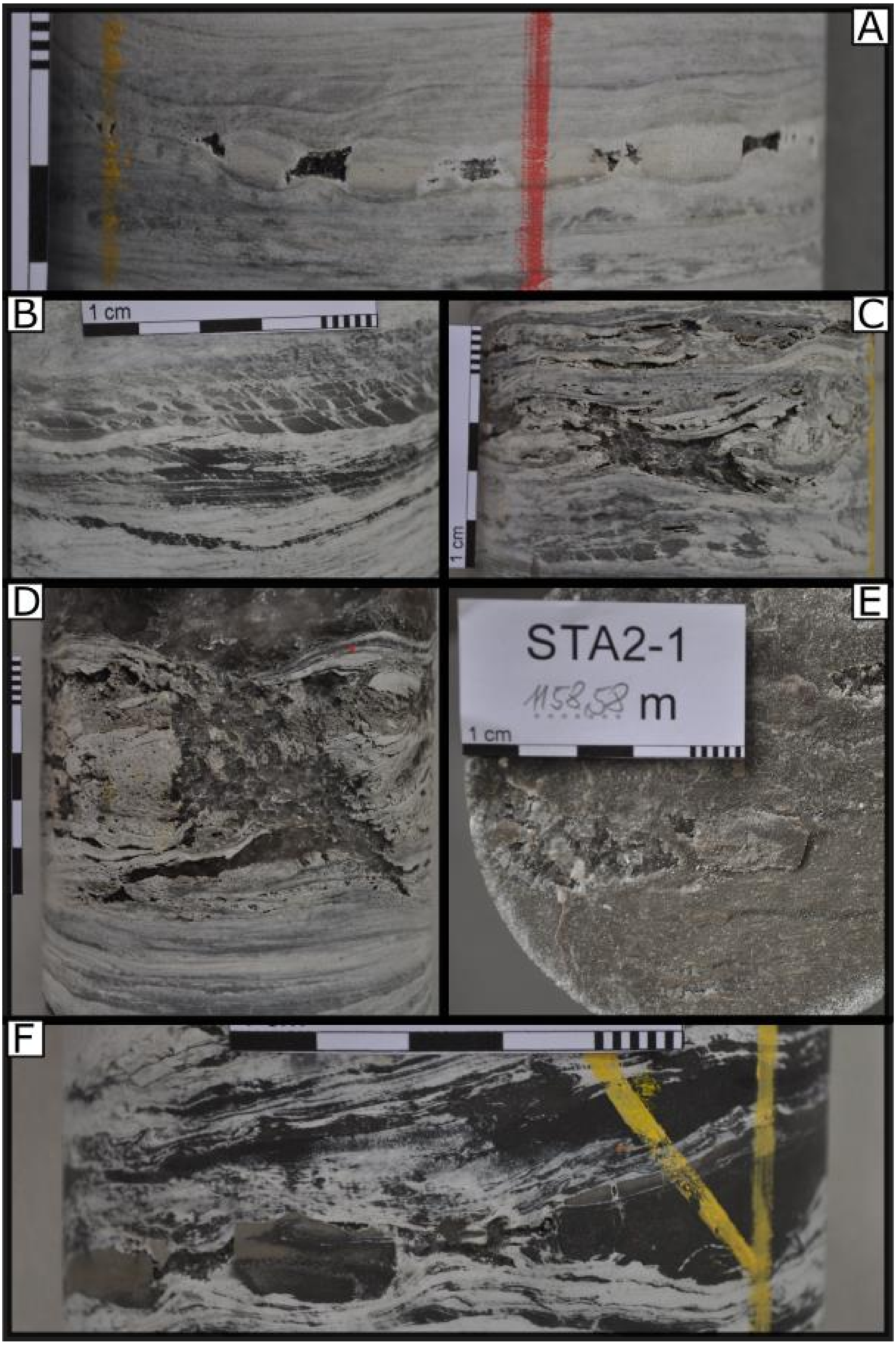


*Fig. 17: A-D+F: Anhydrite and clay boudins as a result of viscous deformation; E: Elongated grains at a core crosscut. A: STA2-1 1166.38m, B: STA2-1 1155.67m, C: STA2-1 1154.33m, D: STA2-1 1154.17m, E: STA2-1 1158.58m , F: STA2-1 1155.81m.*

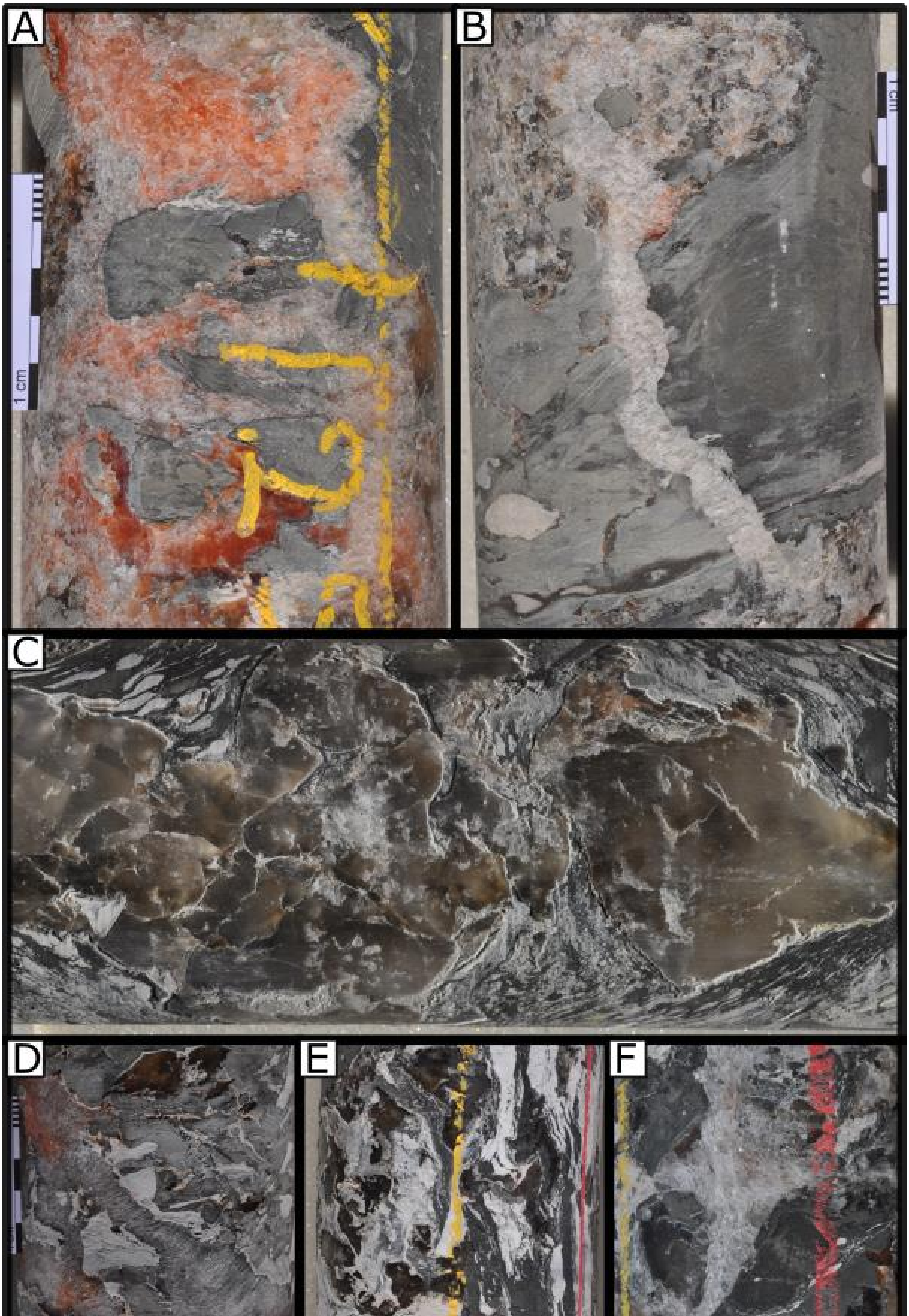


*Fig. 18: A,B,E: Fibrous authigenic halite in tension gashes; C-E: Authigenic halite between anhydrite and clay clasts. A: BUL1-1B 1257.50m, B: BUL1-1B 1257.50m, C: BAC1-1 1179.27m, D: STA3-1 1174.85m, E: STA3-1 1158.65m, F: STA3-1 1156.08m.*

of cm. Fibrous halite grows in cracks of clasts (Fig. 18, B, D). The colour of halite varies from brown and orange tones to clear crystals.

### 3.1.4. Low viscous deformed breccia

This type of breccia is characterised by its relatively high proportion of anhydrite and clay clasts. The clasts vary in sizes from a couple of cm up to core diameter (Fig. 19, A-C). Sedimentary layering is frequently still visible within the clasts (Fig. 19, C, F, G). The matrix surrounding the clasts is build up from fine grained halite. The grains display a shape preferred orientation, which results in a non-penetrative foliation. The orientation of the foliation is not uniform throughout the whole section, as it is deflected by bigger clay or anhydrite clasts (Fig. 19, A-C). There are practically no shear bands in this kind of breccias and if there are, they are often not measurable. At core breaks parallel to foliation stretching lineations can rarely be observed, but they are difficult or even impossible to measure in terms of plunge and plunge direction (Fig. 19, D, E).

Besides fine grained halite, coarse grained halite is present as cm sized survivor grains. Early diagenetic fibrous halite preserved in cracks of anhydrite and clay clasts further proves that deformation of this type of breccia is very low.

### 3.1.5. Viscous deformed breccia

Viscous deformed breccias are mainly build up from fine grained halite crystals, which are mostly elongated, by a roughly 3:1 ratio. For the most parts, a penetrative foliation is observable, even though it is deflected by larger angular, rounded or rotated clay clasts. The overall content of clasts is smaller compared to other halite types (Fig. 20). Comparably narrow shear bands, with widths up to 1.5cm and lengths up to core diameter stand out by their distinctive foliation, which in contrast to the surrounding foliation can be measured in terms of dip and dip direction. Some larger grains or clasts are dissected by shear bands, leading to a displacement of up to 2cm (Fig. 20, C). Core breaks that often occur along and within these seemingly weaker shear bands expose surfaces with a measurable stretching lineation (Fig. 20, E). Shear bands are spaced at distances of approximately 10cm, even though not all are inevitably of the same size and degree of deformation.

*Fig. 19: (following page) A-C: Low viscous deformed halite breccia with large lithoclasts; D+E: Core-cross section: halite grains are partly elongated, but there is no stretching lineation. Larger survivor grains still occur. F: Close up of A: Clay and anhydrite lithoclast, the non-penetrative foliation bends around the lithoclasts; G: Close up of C: large clay and anhydrite lithoclast within*

*the non-penetrative foliation, boudinage within the lithoclast. A: BUL1-1B 1245.55m, B: BUL1-1B 1249.50m, C: STA3-1 1157.70m, D: BUL1-1B 1251.96m, E: BUL1-1B 1255.49m, F: BUL1-1B 1245.55m, G: STA3-1 1157.70m.*

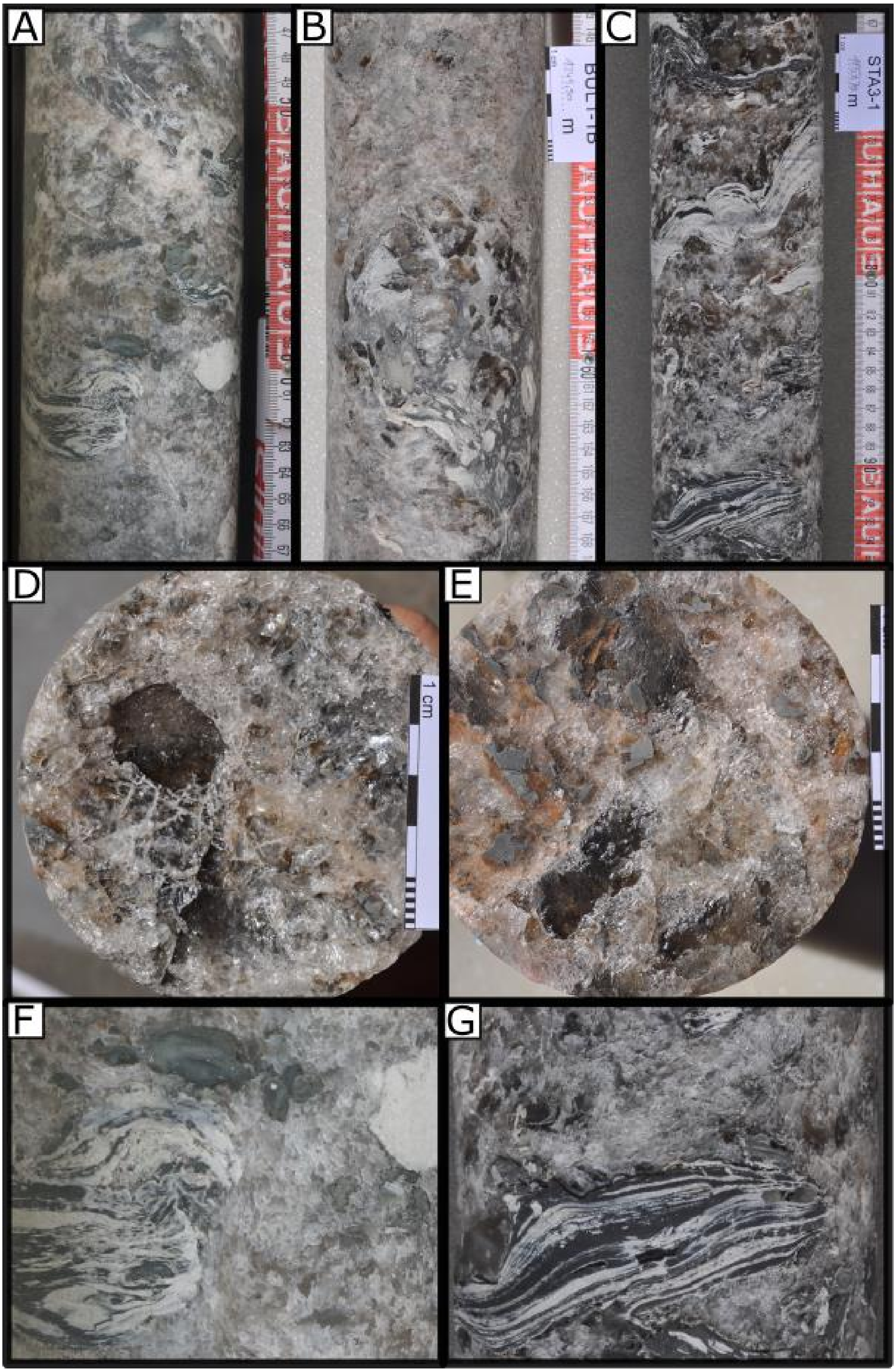

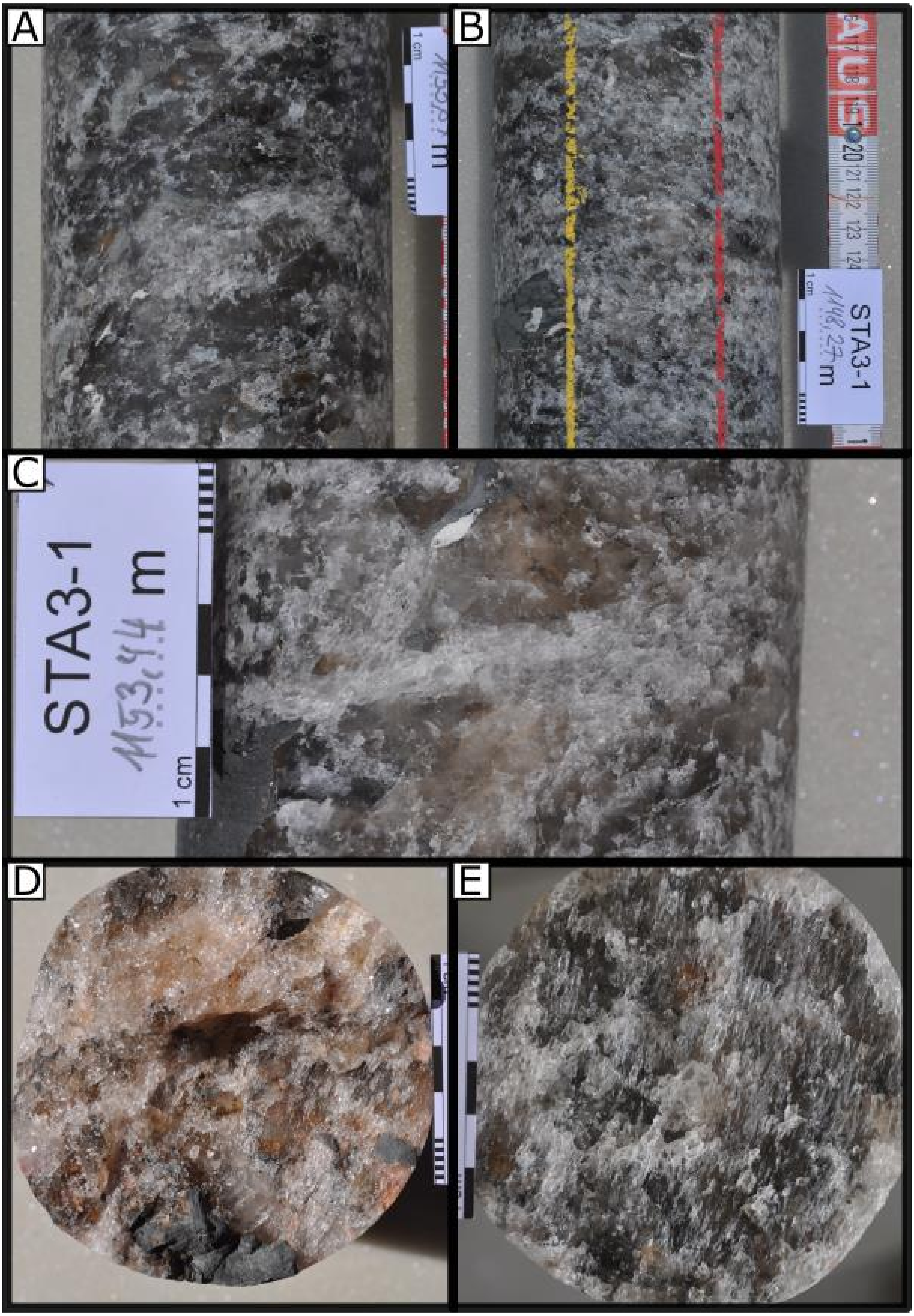


*Fig. 20: A+B: Viscous deformed breccia with clay and anhydrite lithoclasts and shear bands, larger survivor grains are still observable in some sections; C: Shear band displacing a survivor grain; D+E: Core breaks with stretching lineation. A: STA3-1 1153.87m, B: STA3-1 1148.27m, C: STA3-1 1153.44m, D: BUL1-1B 1255.69m, E: STA3-1 1150.89m.*

Larger halitic survivor grains are not as abundant as in lower deformed lithological groups but can often be used as shear sense indicators. In some cases survivor grains are not aligned with the halite matrix and are randomly oriented (Fig. 20, A, B).

### 3.1.6. Undeformed coarse-grained halite

Small sections of the halite cores are completely undeformed. Even though the average grain size of halite is about 5cm, grains often exceed core diameter, thus have sizes over 10cm. They are idiomorph and completely clear and see-through (Fig. 21). At core breaks the cleavage of halite is visible (Fig. 21, C, E). Fracture surfaces are not planar but follow the cleavage planes of halite grains. There are little to no clay or anhydrite components in these core sections.

### 3.1.7. Viscous undeformed halite with seams of clay

This type consists mainly of halite. Clay is present as seams between halite grains or like anhydrite in lithoclast which may vary in sizes. The overall anhydrite and clay content is comparably small in contrast to other types discussed. The size of halite grains varies between 1 to 3cm, no shape preferred orientation is observed. In contrary, some grains are even isometric. Halite crystals are clear, even though they appear to have a brown to greyish undertone, due to clay components between grains (Fig 22).

### 3.1.8. Halite with stylolithic clay layers

These type of halitic sections are characterised by stylolithic clay layers within the halite (Fig. 23). The halite grains are mostly sized between 1 to 2cm, even though larger grains are also present. Halite grains are clear with a brownish or greyish undertone. They show no signs of viscous deformation, and are in general not oriented in a shape preferred orientation. Even though the overall section is viscous undeformed, they may contain narrow shear bands with halite grains sized between 1 to 4mm and shape preferred orientation.

Stylolithic clay layers are intercalated with pure halite, thereby separating the rock salt layers. Clay layers are to a greater extent evenly spaced with an average distance of about 5cm (Fig. 23, A, C, F). All are more or less horizontal. Beside stylolithic clay, clay layers devoid of evidence of pressure solution are also visible. In areas where clay layers are more abundant, smaller, vertical oriented halite grains can be observed between clay layers (Fig. 23, D, E).

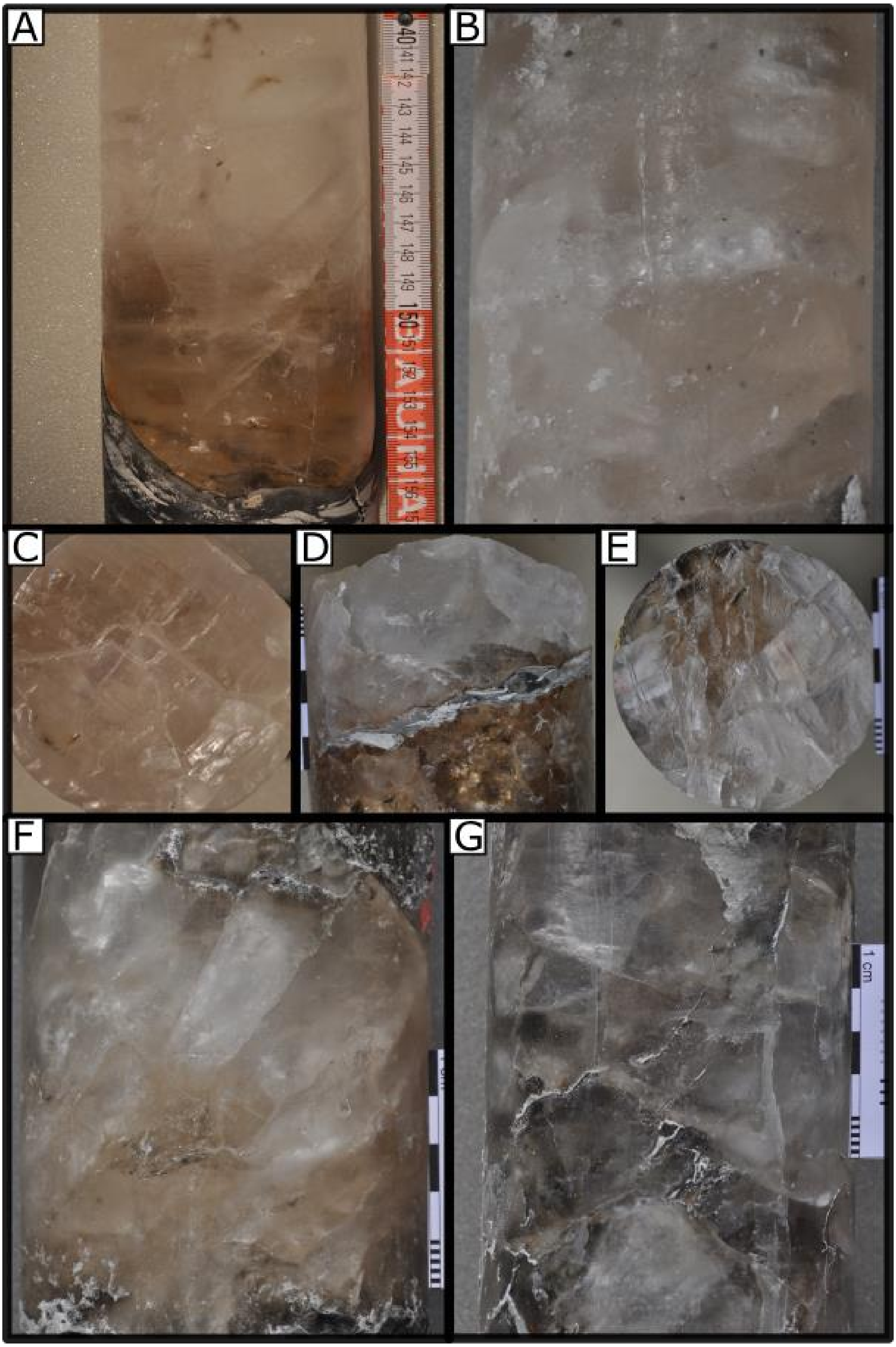


*Fig. 21: A-G: Undeformed halite; C+E: Idiomorph halite grains at core breaks.. A: BAC1-1 1175.37m, B: STA2-1 1168.50m, C: BAC1-1 1175.37m, D: STA3-1 1169.70m, E: STA3-1 1169.70m, F: STA2-1 1152.95m, G: STA3-1 1171.70m.*

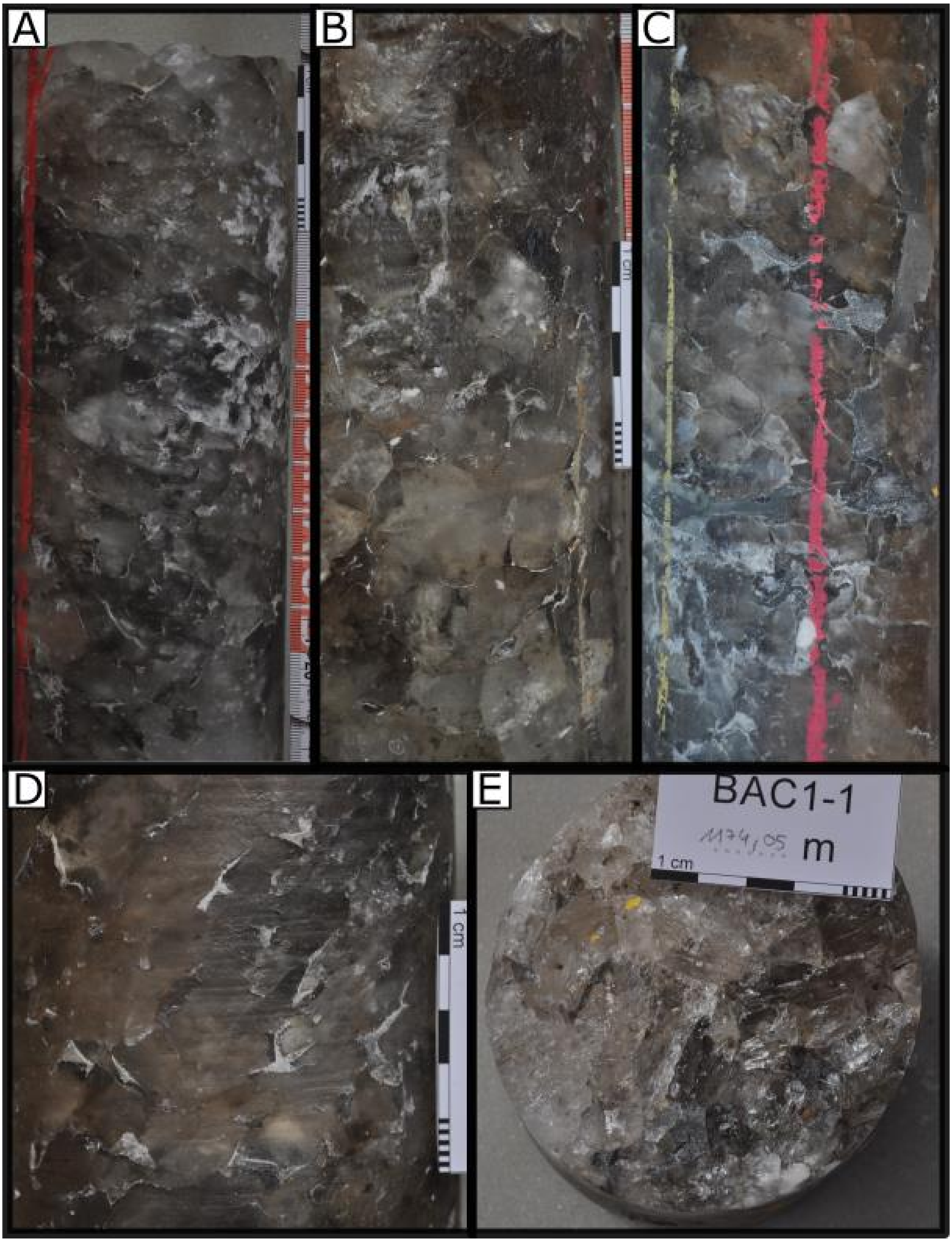


*Fig 22: A-C: Core sections of undeformed halite; D: Closeup of halite grains, with clay seams between grains; E: Core cross-section. A: BAC1-1 1173.02m, B: BAC1-1 1169.75m, C: BAC1-1 1190.16m, D: BAC1-1 1174.25m, E: BAC1-1 1174.05m.*

*Fig. 23: (following page) A-C, F+G: Undeformed halite with stylolithic clay. Clay layers are more or less horizontally oriented and spaced between 3 to 10cm, D+E: Halite grains pushing anhydrite and clay further apart, halite grains are oriented vertically to the direction of growth. A: STA3-1 1135.30m, B: STA2-1 1152.00m, C: BAC1-1 1164.00m, D: BAC1-1 1185.22m, E: BAC1-1 1184.42m, F:BAC1-1 1187.20m, G: STA3-1 1135.74m.*

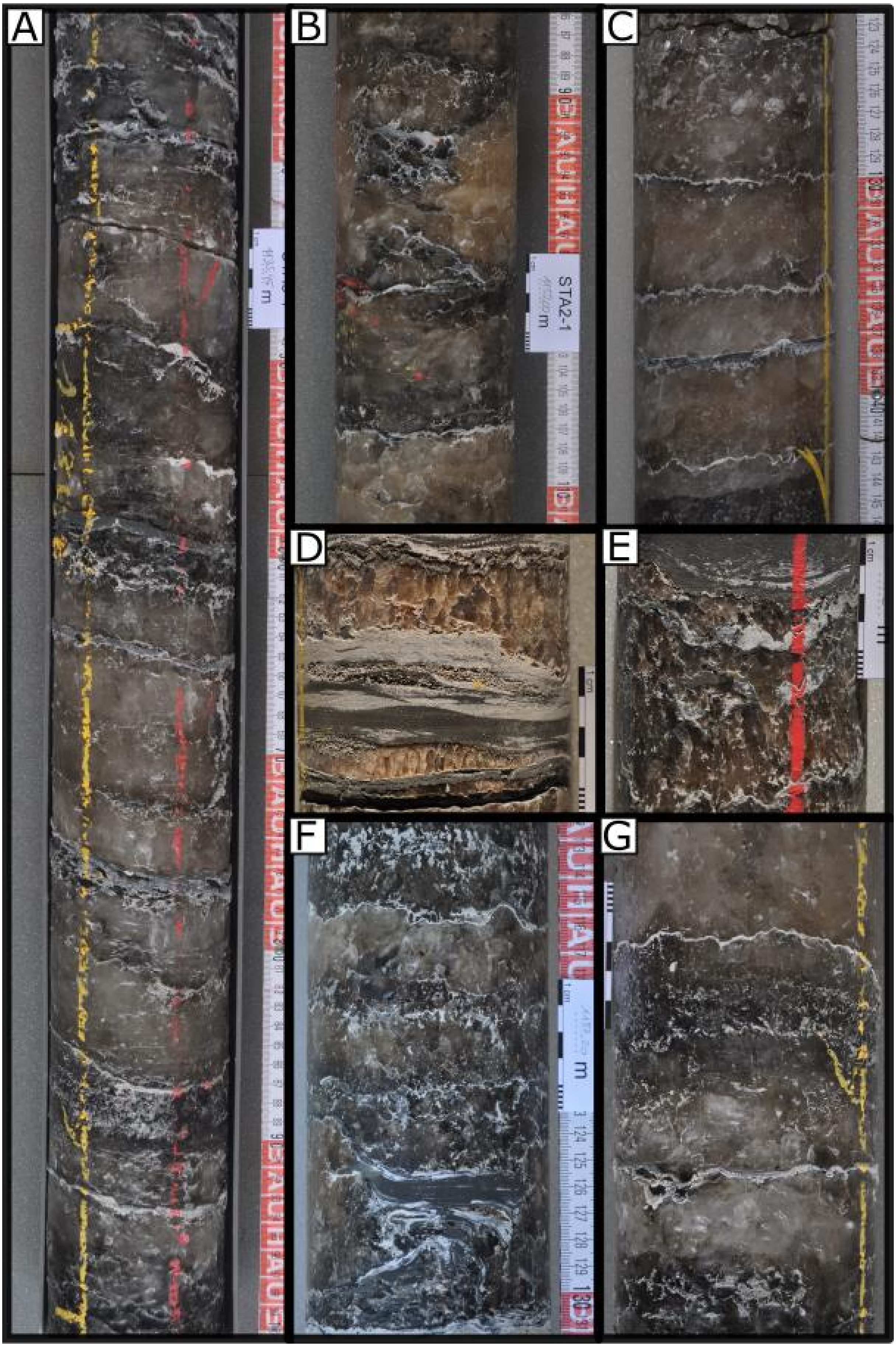
A
B
C
D
E
F
G
STA2-1
m

### 3.1.9. Halite mylonite

Mylonitic halite differs optically from the other described types due to its fine grained halite matrix which is the main constituent of these sections. The mylonitic grains are sized between 1 to 3mm, with an aspect ratio of 3:1 to 2:1 (length : width) and show a shape preferred orientation, thereby forming a penetrative foliation (Fig. 24). Dip and dip direction of the foliation is easily measured. The stretching lineation associated with the mylonitic foliation can be seen and measured at foliation-parallel core breaks (Fig. 24, A, B).

Beside mylonitised halite, coarser sized halite grains may still be present. The size of these survivor grains reaches up to a few cm (Fig. 24, J). If survivor grains are present, their length axis is often oriented oblique to the penetrative mylonitic foliation. Such sigmoid clasts can therefore be used as shear sense indicators. The amount and size of survivor grains varies within the mylonitic sections.

Clay and anhydrite are only present as lithoclasts. The sizes of clasts vary but are relatively small compared to types displaying a lower grade of viscous deformation, with dimensions varying between millimeters and a couple of centimeters in length and width. Clasts can be rounded or angular. Rounded and rotated clasts within the foliation can be used to estimate the shear strain, which lead to the formation of the mylonitic foliation (Fig. 24, D-F).

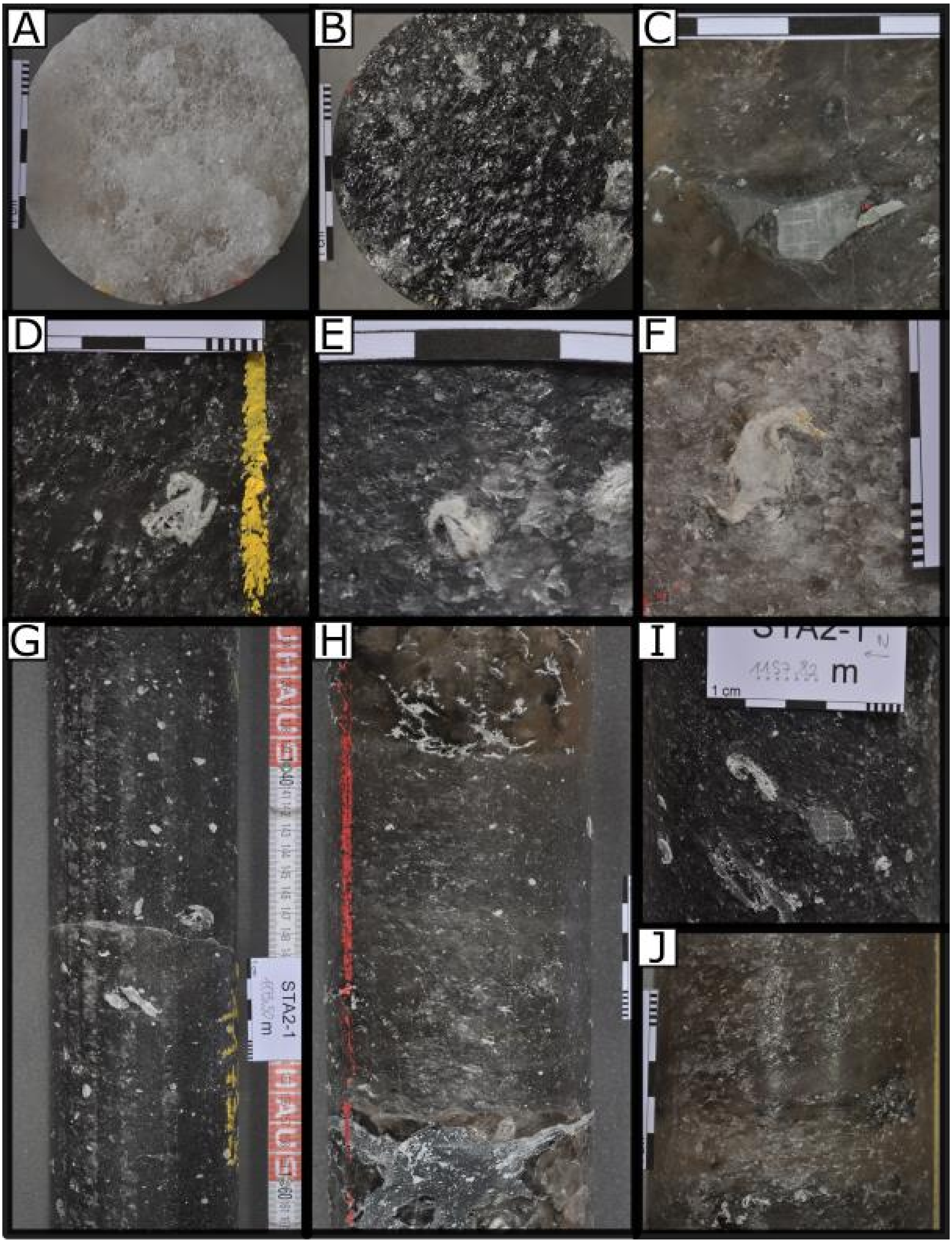


*Fig. 24: A+B: Core cross section with stretching lineation; C: `V´-pull-apart; D-F: Winged inclusions in mylonitic foliation; G-I; Mylonitic halite with different sized and shaped clay clasts; J: Halitic survivor grain oriented with the mylonitic foliation. A: STA2-1 1163.45m, B: STA2-1 1154.13m, C: STA2-1 1165.18m, D: STA2-1 1157.89m, E: STA2-1 1173.64m, F: BUL1-1B 1247.59m, G: STA2-1 1173.50m, H: STA2-1 1153.45m, I: STA2-1 1157.82m, J: STA2-1 1153.75m.*

## 3.2. The development of the evaporitic succession

The evaporitic sequence of the "Salzlager" of the Zeglingen Fm. consists of an alternation of viscous deformed and undeformed anhydrite and halite. Nine main groups can be distinguished in terms of their mineralogical composition and the grade of viscous deformation.

Between the halitic sections, anhydrite and clay are present as either undeformed or deformed layers. Undeformed sections still show depositional structures, as depositional laminae or ripples, whereas deformed layers show characteristic signs of viscous deformation like foliation, stretching lineation or boudinage. Undeformed Hopper crystals can be seen in some parts of the undeformed anhydritic sections.

Authigenic halite breccia develops when halite grows in the joints of anhydrite rocks. In some sections authigenic halite growth seems to push layers of anhydrite and clay further apart (Fig. 18). This type of breccia is viscous undeformed and halite may still display the original direction of growth.

Deformation leads to the formation of a more or less penetrative foliation within the halite-breccia, partially deflected by clay and anhydrite lithoclasts (Fig. 19; Fig. 20). Several up to 1cm wide shear bands with lengths often exceeding core diameter are observable in the more deformed sections. The breakage of the core during drilling processes or core handling along and within the shear bands indicates the weakness of these deformed rocks compared to the undeformed breccia. Measurable stretching lineations occur on these core break surfaces.

Further growth of halite in viscous undeformed authigenic halite breccia leads to the formation of a halite type characterised by 1 to 2cm sized halite gains partly separated by thin seams of clay located along grain boundaries (Fig 22). Larger amounts of clay and anhydrite are still existent in the form of lithoclasts. Evidence of viscous deformation neither can be seen in halite nor in the anhydritic lithoclasts. Therefore, these sections are in the context of this study assumed to be undeformed.

Through ongoing diagenesis, accompanied by compaction, clay is primarily no longer present as clasts or as filler between halite grains, but forms up to 0.5cm wide layers displaying stylolithic bedding. The overall grain size of halite is roughly the same as before, even though smaller grains can be observed in some parts. Although this type, as the previous, is characterised by the lack of viscous deformation, it is observable that viscous deformation localises in these undeformed halite sections (Fig. 23)

Viscous deformation of the former stylolithic clay layers results in stretching and disintegration of clay layers which then are present as mm to cm sized clay clasts in a halite matrix. With higher grade of viscous deformation the clasts are no longer angular but rounded and may show signs of rotation out of the shear plane. These so-called winged inclusions allow for an interpretation of the finite strain (Grasemann & Dabrowki, 2014). Halite grains show shape preferred orientation thereby forming a penetrative mylonitic foliation, with related stretching lineations being measurable at core breaks. The average size of halite grains has reduced to 4mm and the grains are elongated, whereby the grain aspect ratio varies between 3:1 to 2:1 (length : width).  Even though overall grain size is in the millimeter range larger survivor grains up to several cm are still present in the mylonitic sections. Survivor grains may display a shape preferred orientation as well (Fig. 24).

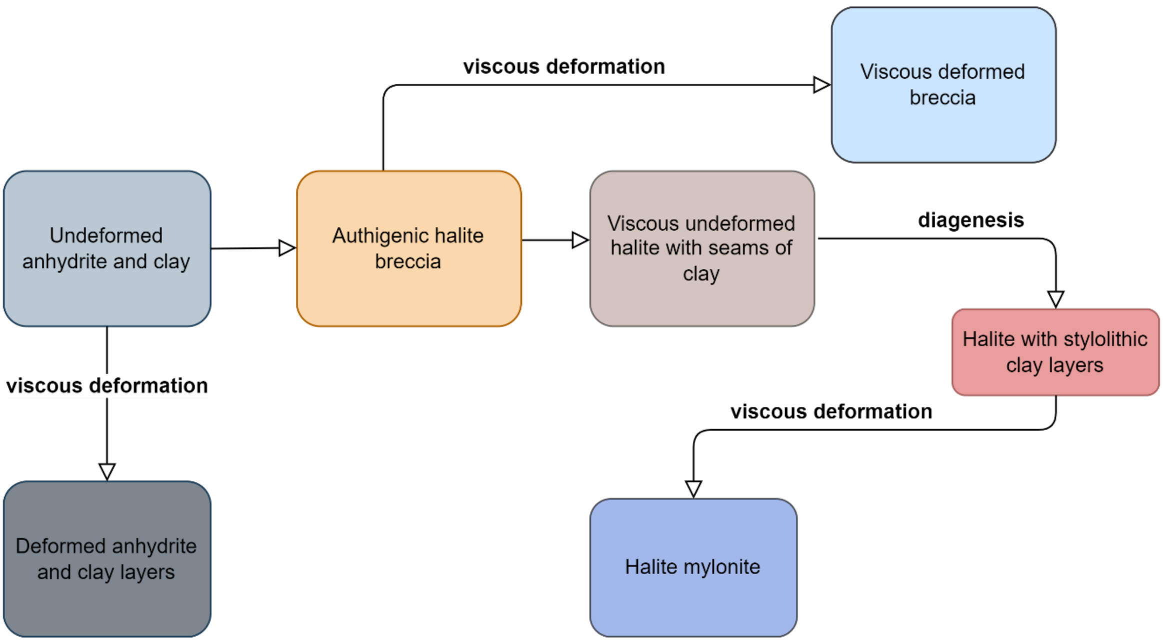


*Fig. 25: Diagenetic and deformational evolution of the evaporite lithotypes.*

## 3.3. Lithological profiles

The lithological profiles are based on the assignment of core sections into the groups presented in the previous chapter. For a more detailed recording of the cores an intermediate link between viscous undeformed halite and halite mylonite was implemented as low viscous deformed halite. A total of 121.75m core section of the four investigated boreholes was recorded and categorised.

### 3.3.1. STA2-1

The cores of STA2-1 consist approximately to 1/3 of anhydrite and clay and to 2/3 of halite in different facies and grades of viscous deformation. The anhydrite and clay sections are in equal parts deformed and undeformed. About 8m of the cores are halite mylonites which, however, differ by the occurrence and abundance of larger survivor grains. With a length of 0.33m only a small part of the cores consists of undeformed, idiomorph halite crystals. Low viscous deformed halite breccia makes up roughly 3.5m of the cores. Halite with stylolithic layers of clay, halite with seams of clay and low viscous deformed halite are the remaining sections of the core, with a length of about 6m (Fig. 26).

### 3.3.2. STA3-1

The analysed cores of STA3-1 have an overall length of about 40m. Approximately 1/4 of the cores are anhydrite and clay layers with authigenic halite. Anhydrite and clay layers without halite have an accumulated thickness of 5m. Compared to the cores of STA2-1 the amount and thickness of mylonitic sections is smaller. However, sections of viscous deformed breccia at a total length of 10m are more abundant than in STA2-1. Halite with seams of clay occur at an accumulated thickness of 7.7m (Fig. 27).

### 3.3.3. BUL1-1B

With a total length of 16m, the evaporitic section of BUL1-1B has the smallest thickness of the four investigated boreholes. The cores mainly consist of low viscous deformed breccia. Beside breccias smaller amounts of halite mylonites occur. Undeformed anhydrite and clay layers with and without authigenic halite appear in comparably narrow sections (Fig. 28).

### 3.3.4. BAC1-1

The cores of BAC1-1 are partly build up from a viscous undeformed breccia consisting of equal amounts of authigenic halite and anhydrite and clay. Beside in BAC1-1 this type can only be seen in a narrow section in the cores of BUL1-1B. However, viscous deformed breccias cannot be observed in BAC1-1. Halite mylonite and low viscous deformed halite occur at a total length of 9m. Viscous undeformed layers of anhydrite and clay appear at an accumulated length of about 10m (Fig. 29).

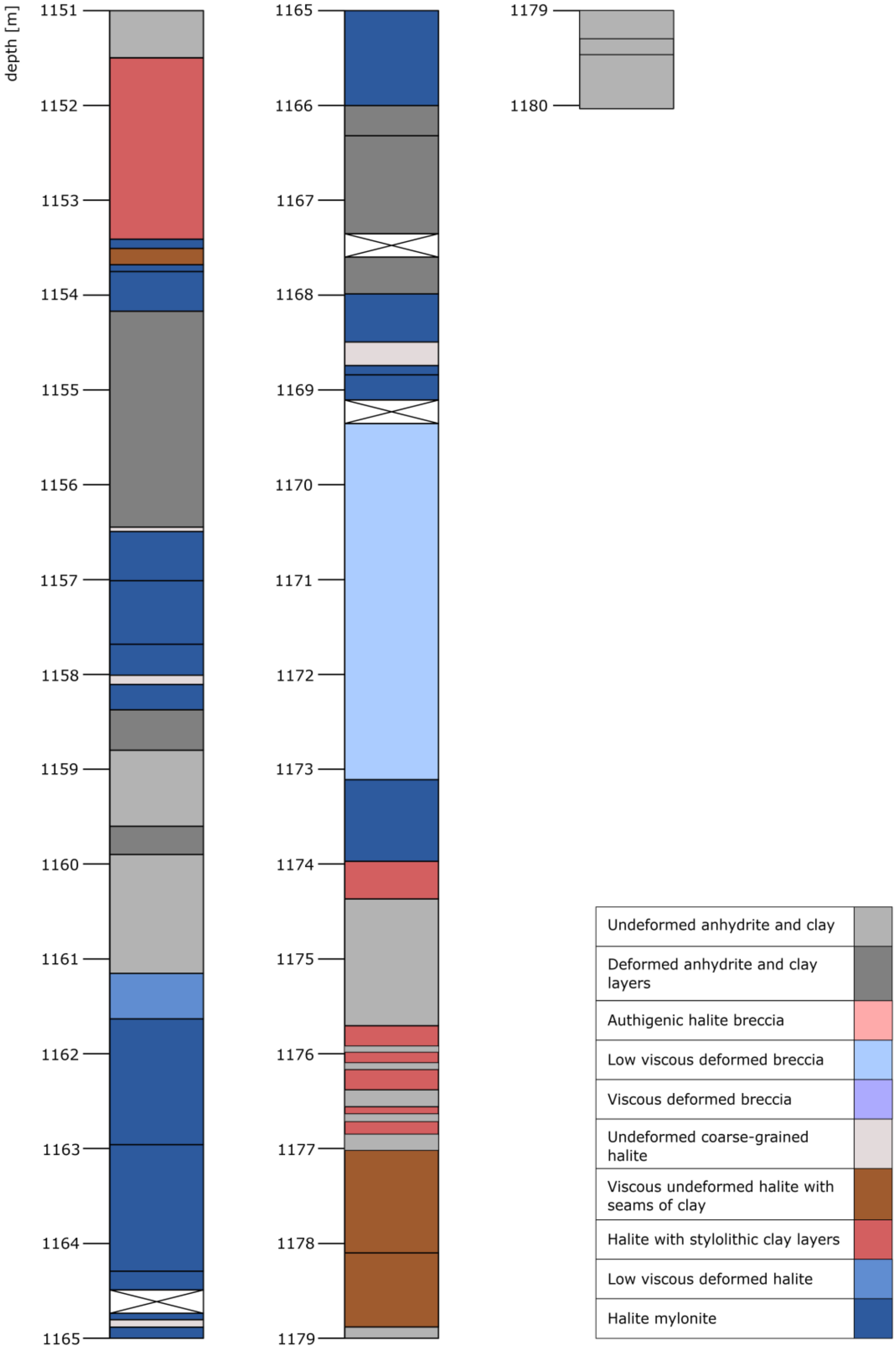


*Fig. 26: Lithological profile of STA2-1. Crossed sections represent core loss.*

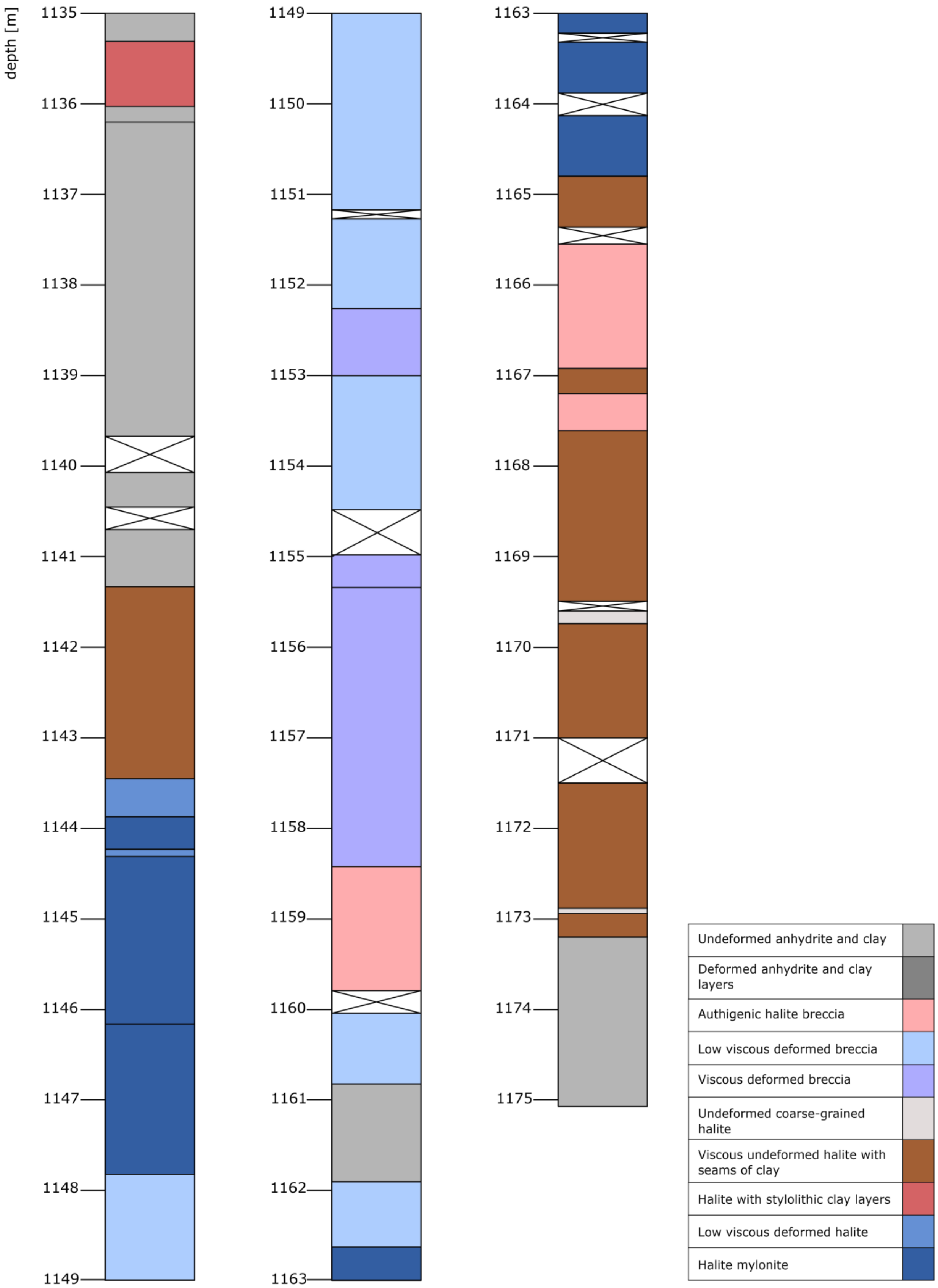


*Fig. 27: Lithological profile of STA3-1. Crossed sections represent core loss.*

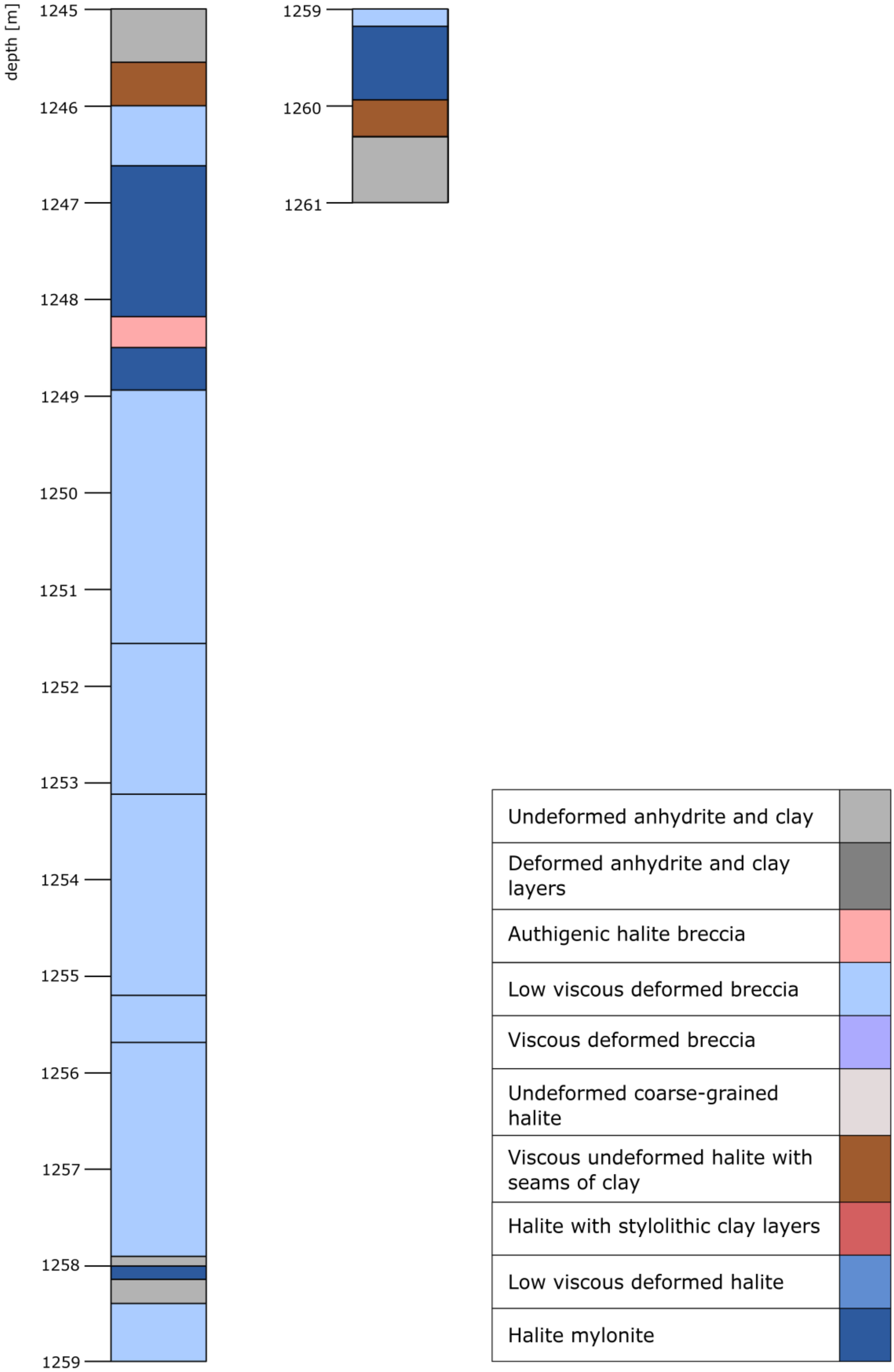


*Fig. 28: Lithological profile of BUL1-1B.*

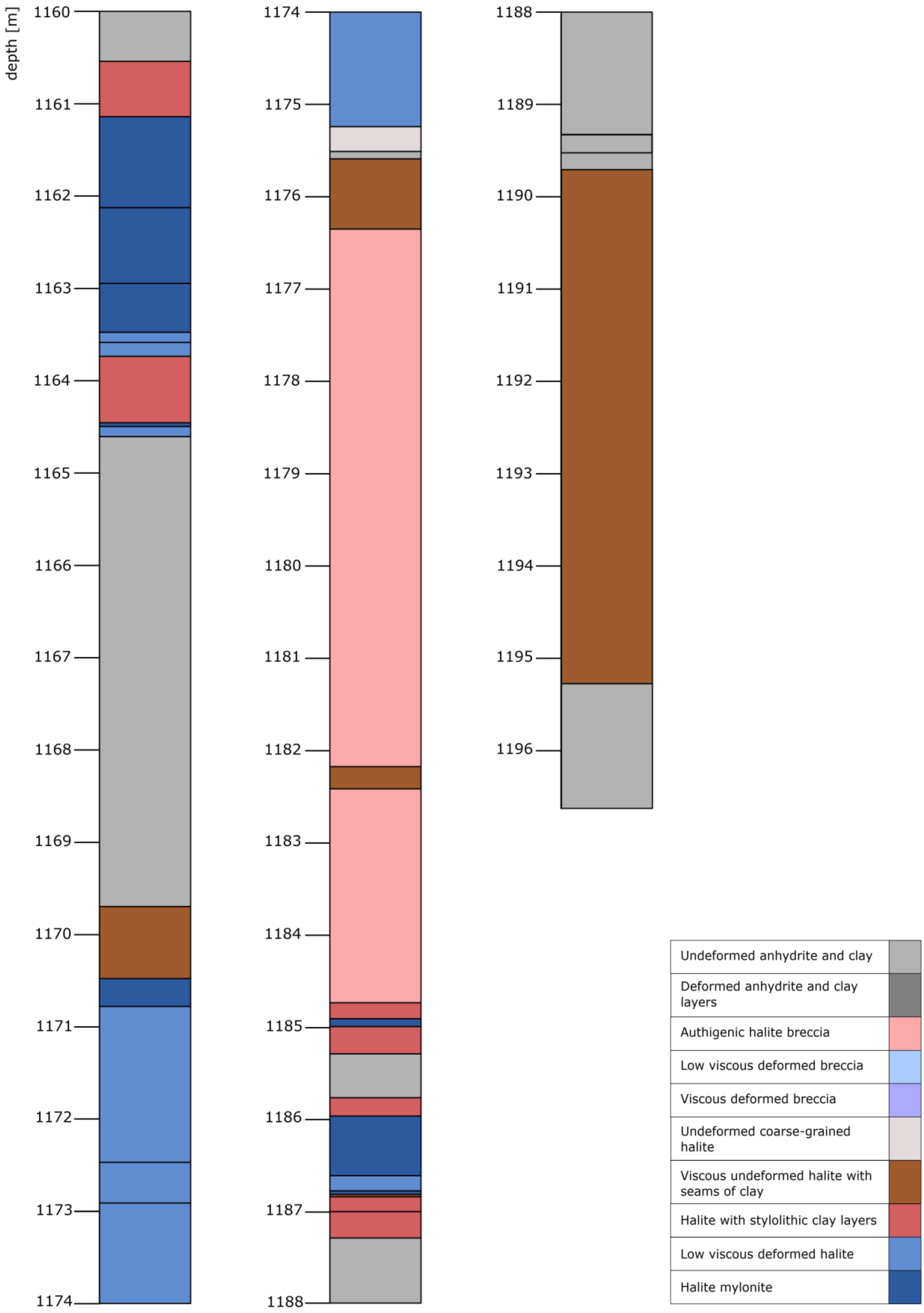


*Fig. 29: Lithological profile of BAC1-1.*

# 4. Determination of the mineralogical composition

The determination of the mineralogical composition was carried out via X-ray powder diffraction. Therefore 22 samples (Table 2, Fig. 30) collected from different depths of the 4 cores were pulverised and analysed at the University of Vienna. Several samples from the main lithological groups were analysed to investigate the mineralogical composition of the different rock types especially focusing on rock salt matrix and lithoclasts, as rheological contrast of matrix and clasts are of crucial importance for the determination of strain.

*Table 2: Material and lithological content of 22 samples of the four boreholes analysed via X-ray powder diffraction.*

| **Nr.** | **Borehole** | **Depth [m]** | **Pulverised material** | **Lithological group** |
|---|---|---|---|---|
| 1 | STA2-1 | 1151.66 | Halite | Halite with stylolithic clay layers |
| 2 | STA2-1 | 1153.10 | Halite | Halite with stylolithic clay layers |
| 3 | STA2-1 | 1159.01 | Anhydrite | Undeformed anhydrite and clay |
| 4 | STA2-1 | 1161.17 | Halite | Low viscous deformed halite |
| 5 | STA2-1 | 1163.39 | Halite | Halite mylonite |
| 6 | STA2-1 | 1167.99 | Anhydrite layers, halite in boudin neck | Deformed anhydrite and clay layers |
| 7 | STA2-1 | 1173.09 | Halite and lithoclasts | Halite mylonite |
| 8 | STA2-1 | 1173.50 | Halite | Halite mylonite |
| 9 | STA2-1 | 1175.75 | Anhydrite and halite | Halite with stylolithic clay layers |
| 10 | STA2-1 | 1177.11 | Halite with seams of anhydrite and clay | Viscous undeformed halite with seams of clay |
| 11 | STA2-1 | 1177.54 | Halite | Viscous undeformed halite with seams of clay |
| 12 | STA2-1 | 1178.15 | Halite | Viscous undeformed halite with seams of clay |
| 13 | STA3-1 | 1145.05 | Halite and lithoclasts | Halite mylonite |
| 14 | STA3-1 | 1156.56 | Halite and lithoclasts | Viscous deformed breccia |
| 15 | STA3-1 | 1164.38 | Halite and lithoclasts | Halite mylonite |
| 16 | STA3-1 | 1164.38 | Halite and lithoclasts | Halite mylonite |
| 17 | BUL1-1B | 1248.94 | Halite and lithoclasts | Halite mylonite |
| 18 | BUL1-1B | 1248.94 | Halite and lithoclasts | Halite mylonite |
| 19 | BUL1-1B | 1249.83 | Lithoclasts and halite | Low viscous deformed breccia |
| 20 | BAC1-1 | 1177.10 | Lithoclasts and halite | Authigenic halite breccia |
| 21 | BAC1-1 | 1186.08 | Halite | Halite mylonite |
| 22 | BAC1-1 | 1188.30 | Halite from tension gash | Undeformed anhydrite and clay |

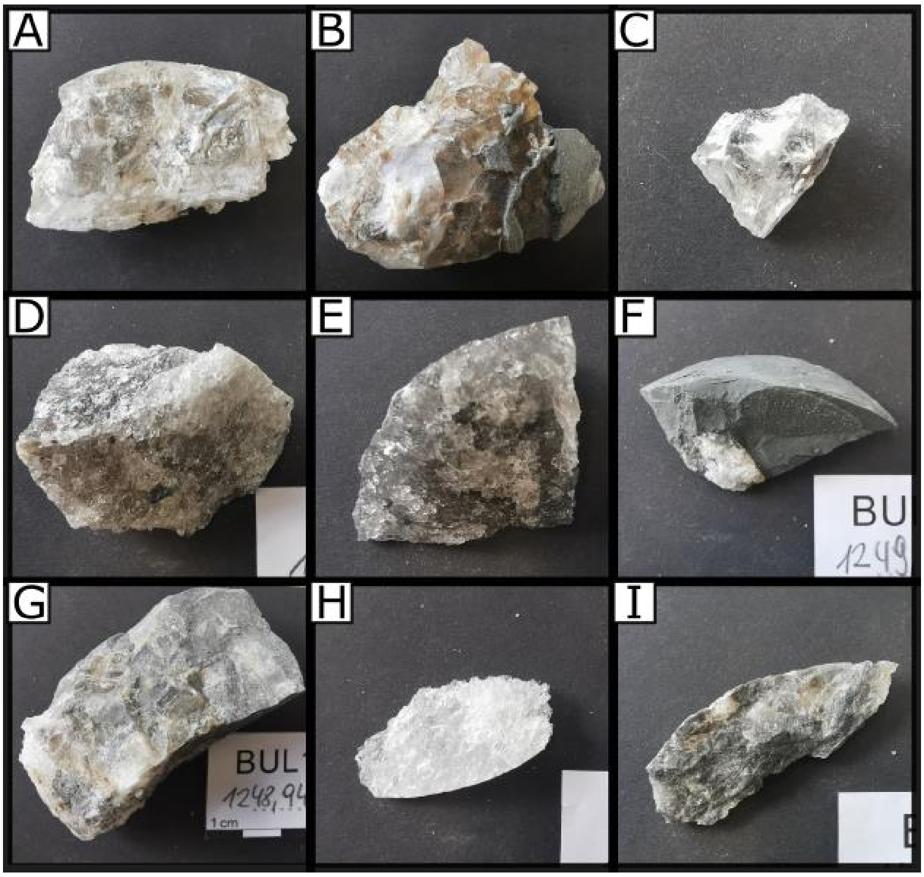


*Fig. 30: XRD-samples; A: Nr.11, STA2-1 1177.54m, halite; B: Nr.10, STA2-1 1177.11m, halite, anhydrite and clay; C: Nr.4, STA2-1 1161.17m, halite; D: Nr.15, STA3-1 1164.38m, halite and anhydrite; E: Nr.16, STA3-1 1164.38m, halite and anhydrite; F: Nr.19; BUL1-1B 1249.83m, halite, anhydrite and clay; G: Nr.18, BUL1-1B 1248.94m, halite and anhydrite; H: Nr.21, BAC1-1 1186.08m, halite; I: Nr.20, BAC1-1 1177.10m, halite, anhydrite and clay.*

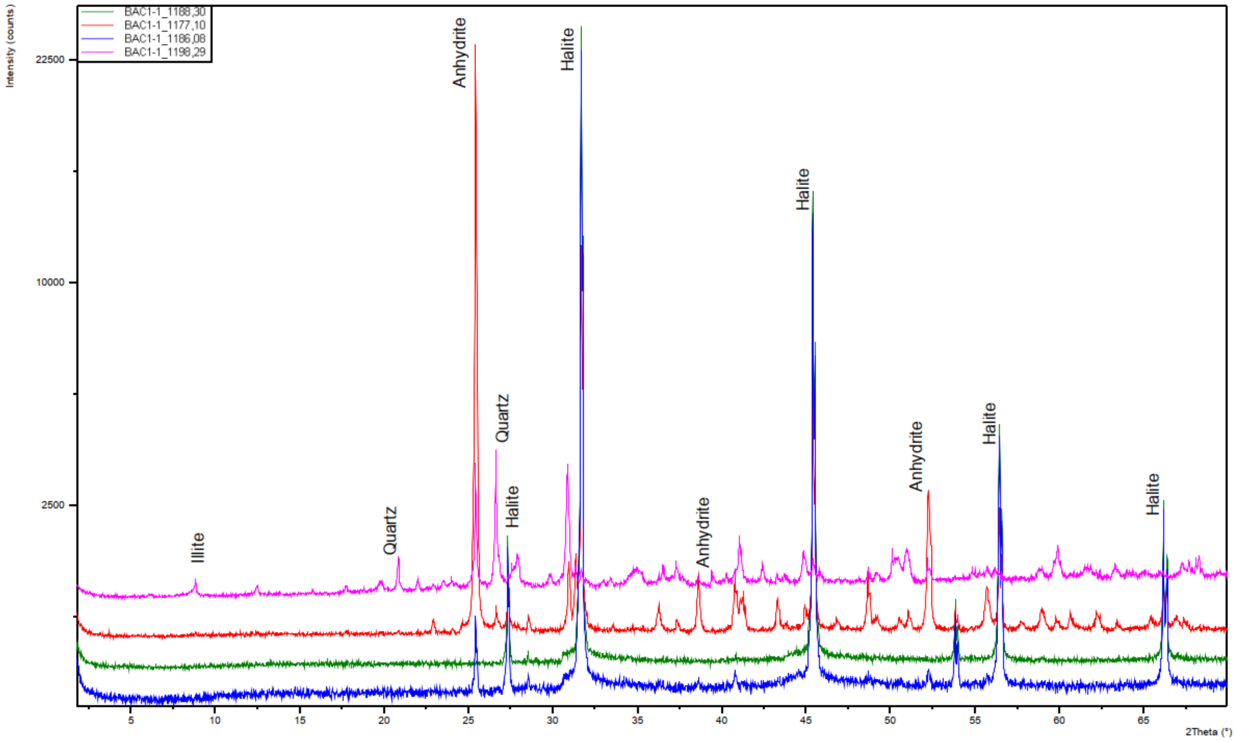


*Fig. 31: X-ray diffractogram of BAC1-1.*

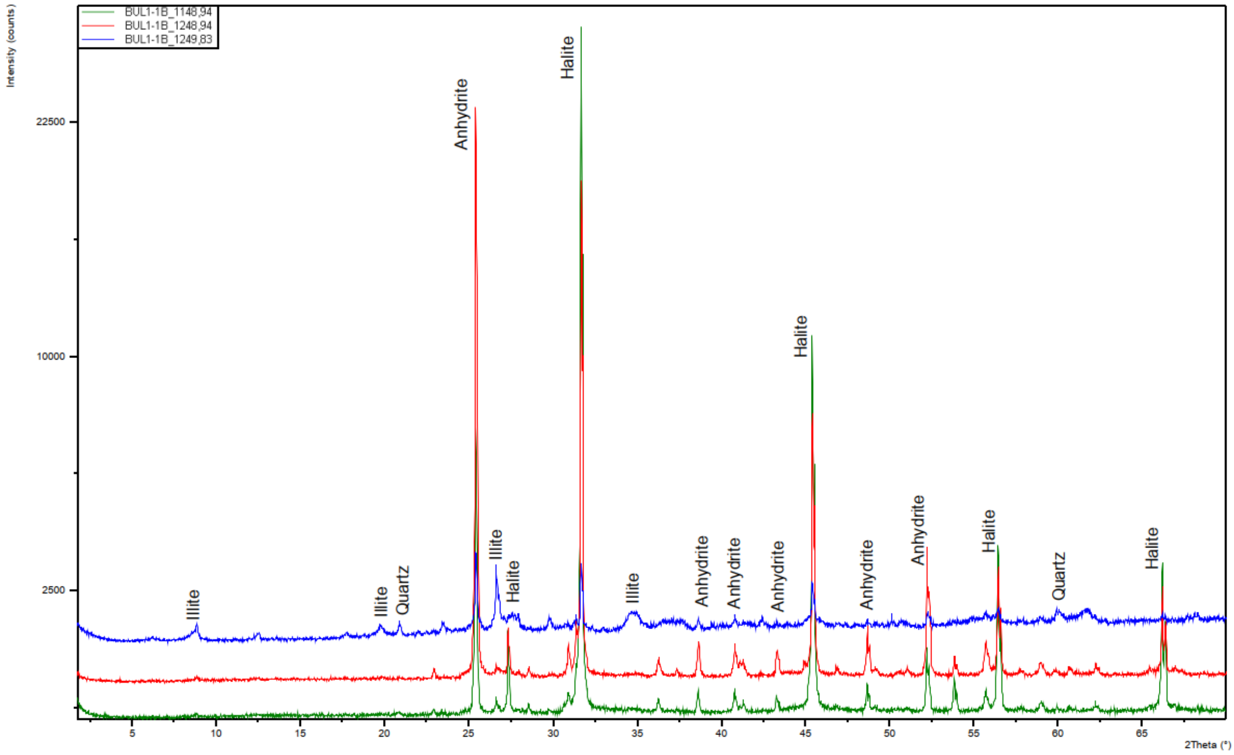


*Fig. 32: X-ray diffractogram of BUL1-1B*

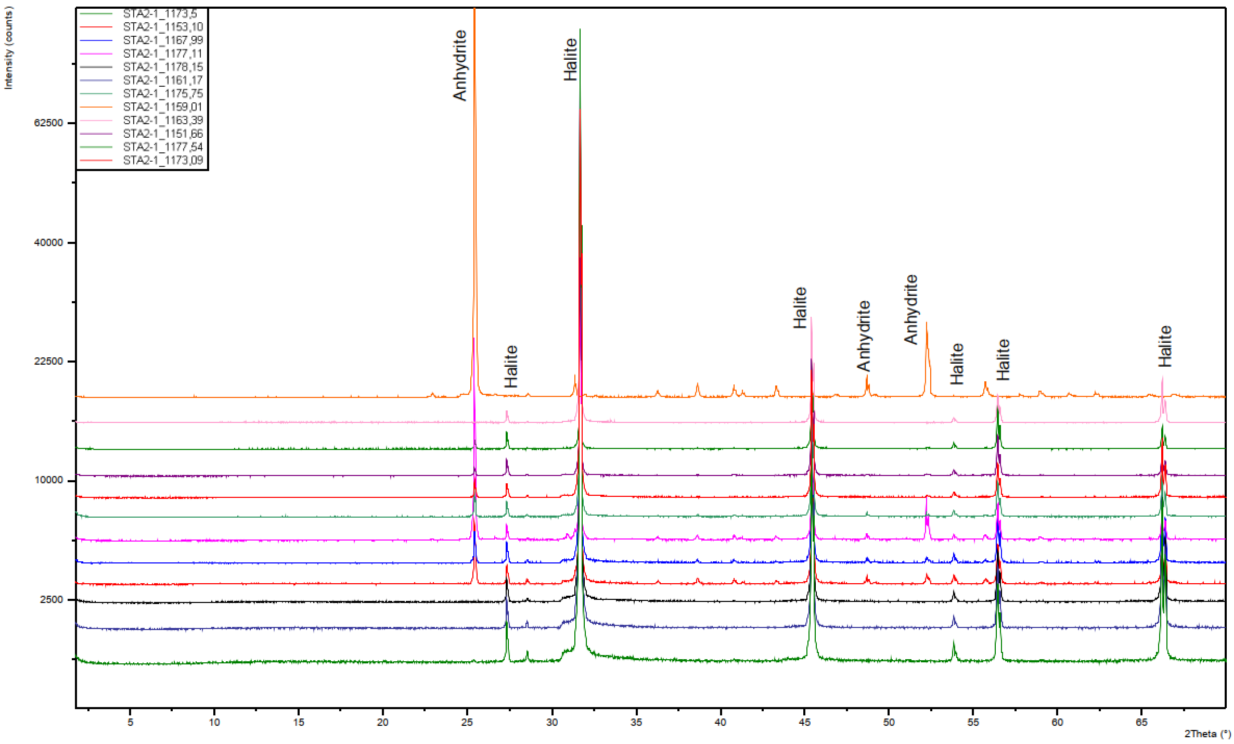


*Fig. 33: X-ray diffractogram of STA2-1.*

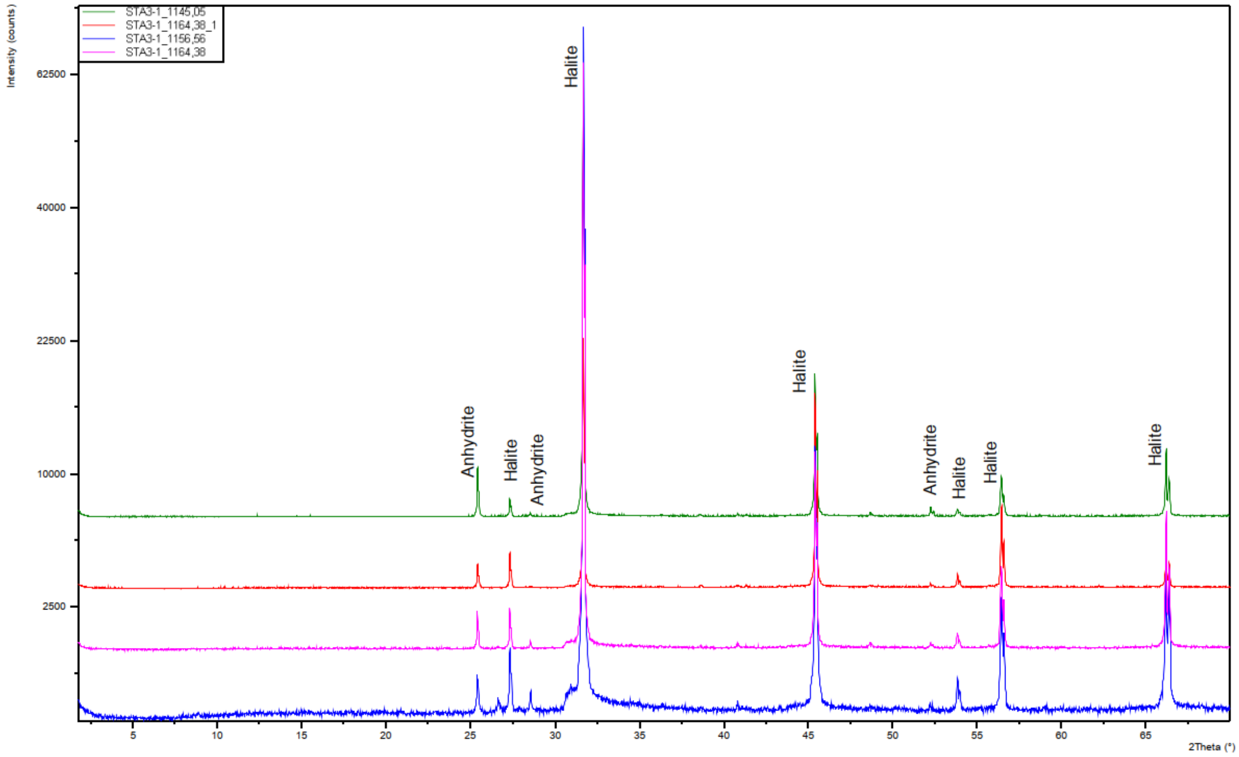


*Fig. 34: X-ray diffractogram of STA3-1.*

The diffraction patterns of all samples show similar results, displaying mainly peaks of halite, anhydrite and frequently illite. Only two samples of BAC1-1 (Fig. 31) and BUL1-1B (Fig. 32) include small amounts of quartz.

The results of the X-ray powder diffraction therefore confirm and are consistent with the visual classification of minerals carried out directly at the cores.

# 5. Determination of strain based on structures

## 5.1. Boudins

The studied cores of STA2-1 contain boudins (Fig. 35, A, C) as well as foliation boudins (Fig. 35, B, C). The boudins are mostly localised in the lithological group deformed anhydrite and clay layers. Non-viscosity-contrast dependant boudinage, resulting in foliation boudinage, as well as contrast dependant boudinage, leading to seperated individual boudins, occur in these layered anhydrite and clay sections. Precipitated halite partly occurs between separated boudins or in boudin necks (Fig. 35).

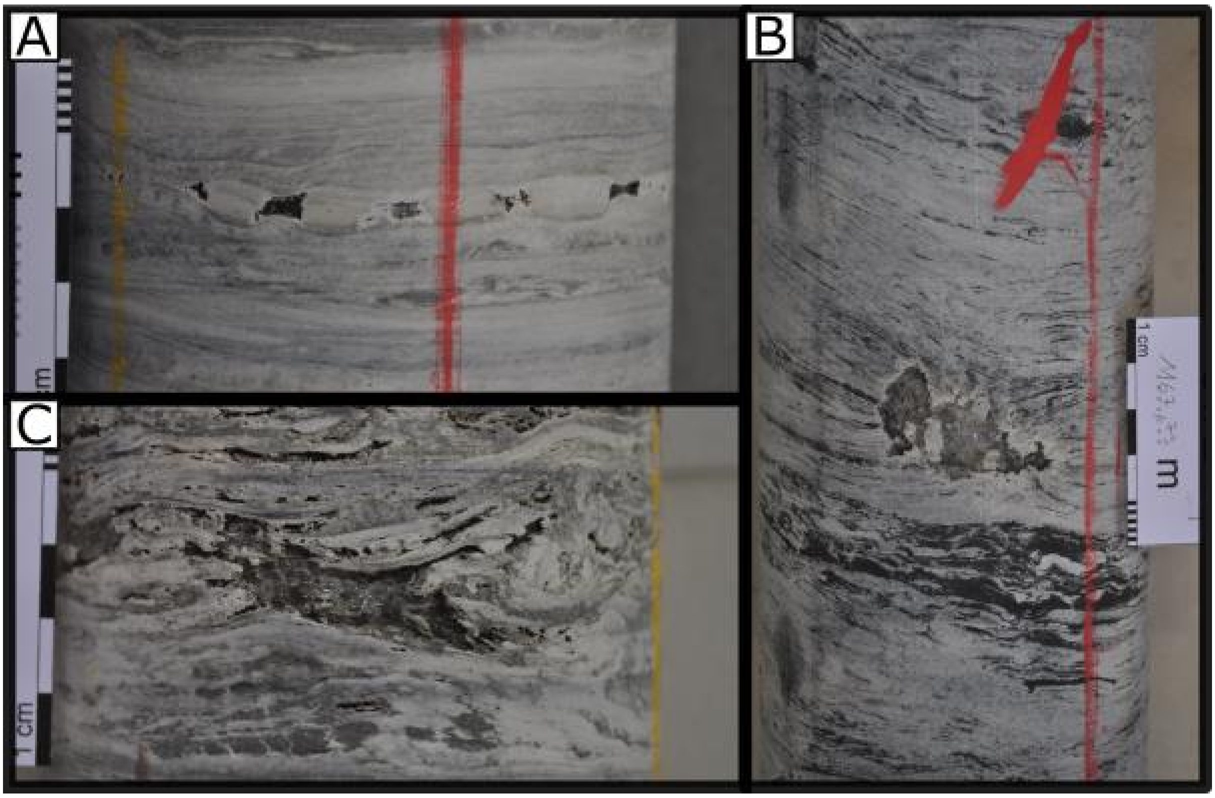


*Fig. 35: A: Boudins STA2-1 1166.38m; B: Foliation boudin STA2-1 1167.73m; C: Boudin and foliation boudin STA2-1 1154.33m.*

A thin section of deformed anhydrite and clay layers of STA2-1 at a depht of 1155.50m in section perpendicular to the boudin axis was prepared in order to determine the aspect ratio of micro-scale boudins (Fig. 38). In this section the boudins constist of former clay layers and the matrix is composed of anhydrite. A total number of 89 boudins from different stretched layers within the section were measured in terms of length and width and plotted. The slope can be roughly described by a linear trend, with some dispersions (Fig. 36, a). Boudin aspect ratios <2.5 at a relative frequency of ~41% are approximately equally common as aspect ratios of 2.5 to 3.5 with a relative frequency of ~39%. Aspect ratios >3.6 occur at a relative frequency of ~20% (Fig. 36, b).

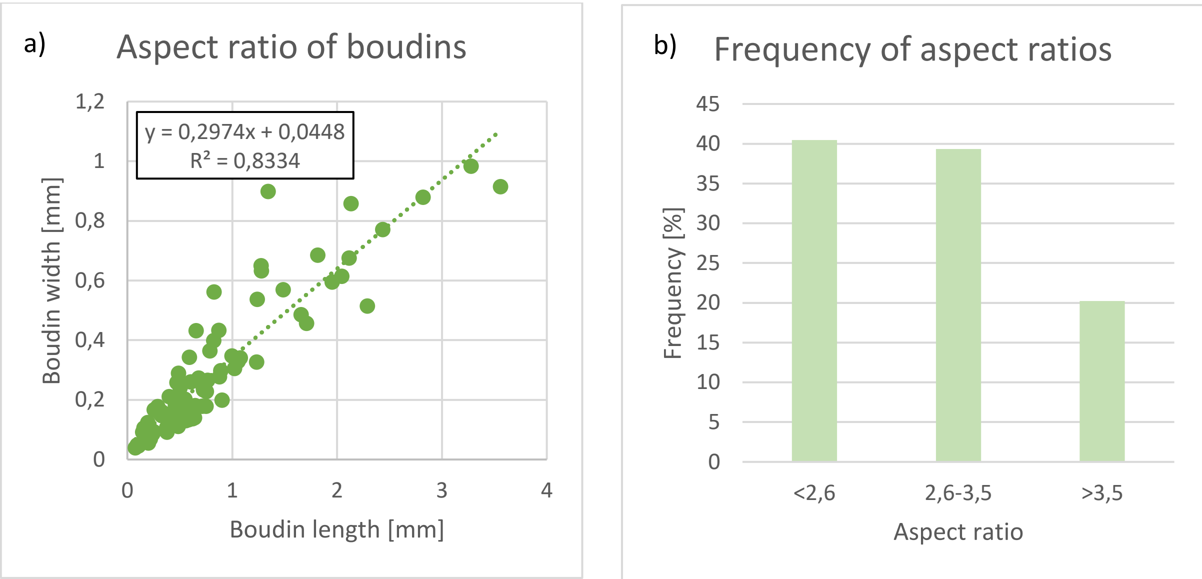


*Fig. 36: a) Aspect ratios of 89 boudins measured in a thin section of STA2-1 1155.50m (Fig. 38); b) According to their aspect ratio boudins were divided into groups (<2.6, 2.6-3.5, >3.5). Columns represent the frequency at which aspect ratios (assigned into the three groups) occur as a percentage of 89.*

The length of boudins and of their associated stretched layer were measured in a core cross-section (Fig. 37) of STA2-1 at depth of 1158.75m and in a thin section (Fig. 38) of STA2-1 at a depth of 1155.50m. Elongation ($\Delta l/l_0$) or linear strain calculated from boudins of the core section is 0.25. Elongation determined from the thin section is slightly higher at 0.85.

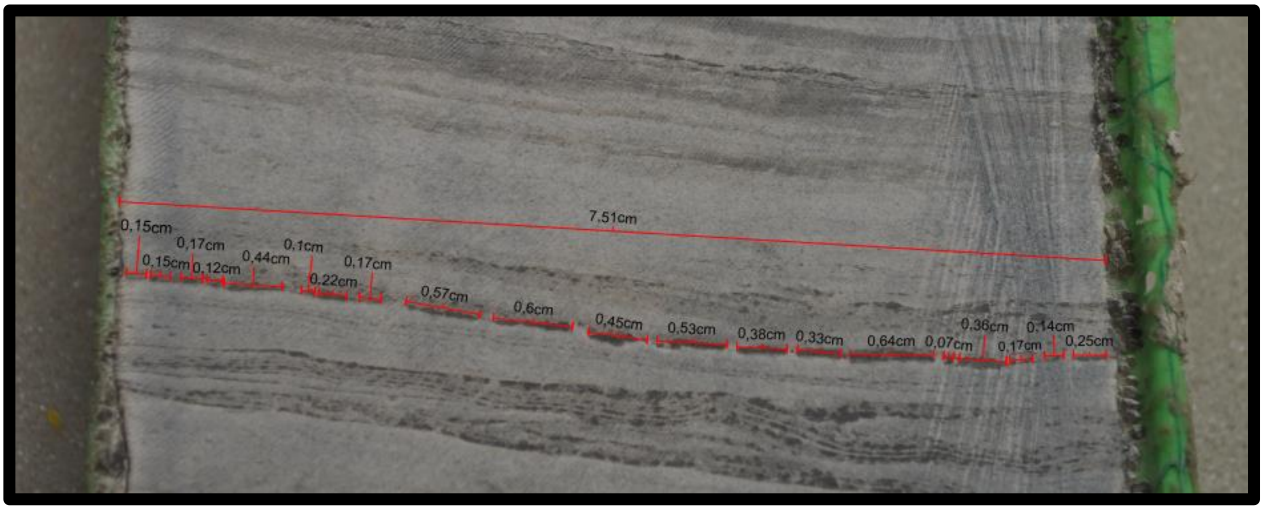


*Fig. 37: Boudinage in anhydrite. Accumulated boudin length ($l_0$): 6.01cm, length of the layer after boudinage (l): 7.51cm; STA2-1 1158.78m.*

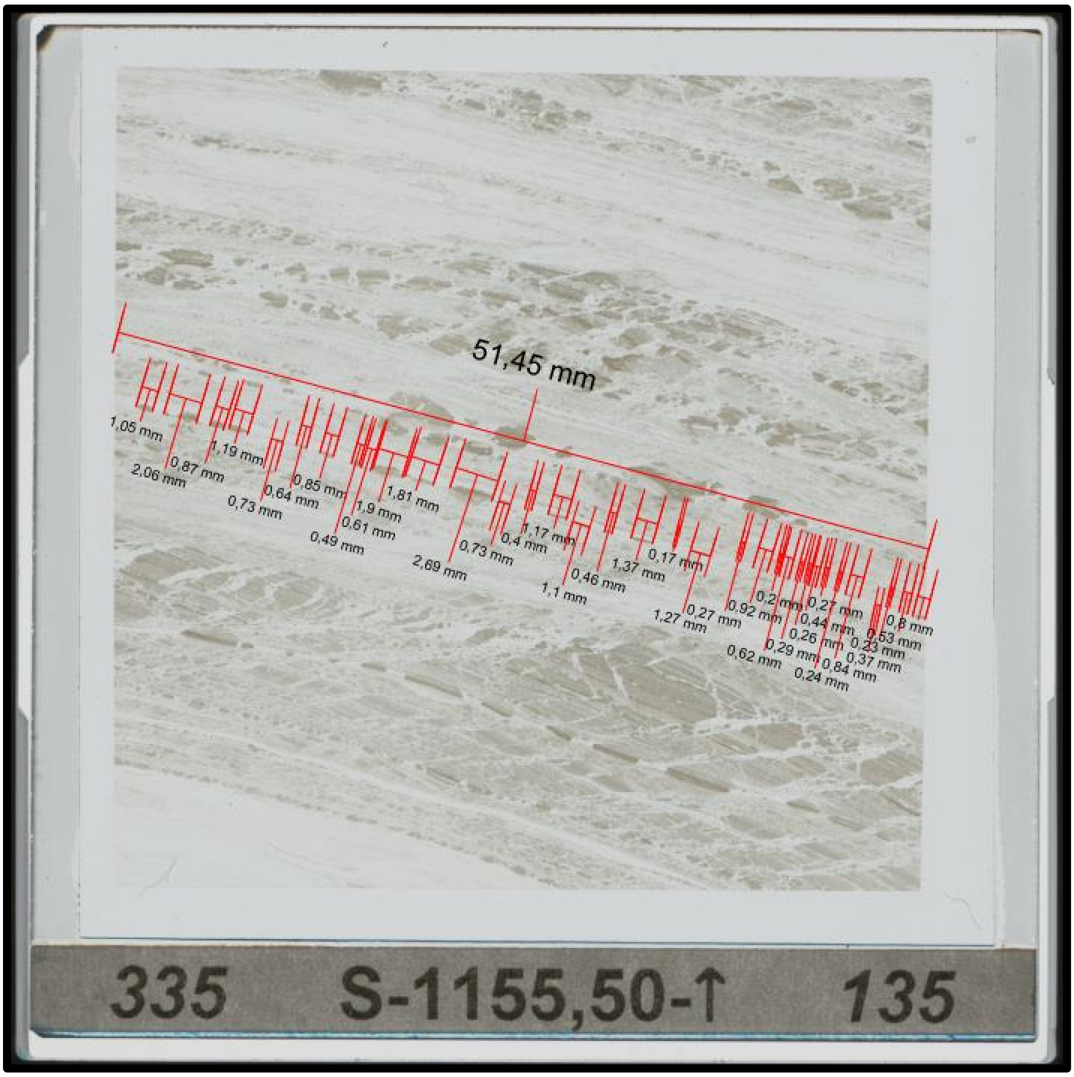


*Fig. 38: Boudinage in anhydrite. Accumulated boudin length ($l_0$)= 27.84mm, length of the layer after boudinage (l)= 51.45mm; STA2-1 1155.50m.*

## 5.2. Winged inclusions

Using the high-strain numerical model for pinch-and-swell structures developed by Grasemann & Dabrowski (2014) winged inclusions are usable to estimate finite shear strain.

In the studied cores, the winged inclusions consist of anhydrite and clay and are embedded in a halite matrix (Fig. 39). The viscosity contrast *m* of anhydrite and halite ranges between 10 to 30 (Adamuszek et al., 2015).

A visual comparison of the encountered winged inclusions within the halites of the Zeglingen Fm. with the results of the linear viscous models infers shear strains of $\gamma \approx 10$ (Fig. 39, Fig. 40). However, shear strains up to $\gamma \approx 20$ cannot be fully excluded due to the similarities of modelling results. Therefore in the course of this master thesis shear strains of up to $\gamma \approx 15$ are assumed for halite mylonites and thus as well for the subsequent calculations of strain rate and total displacement.

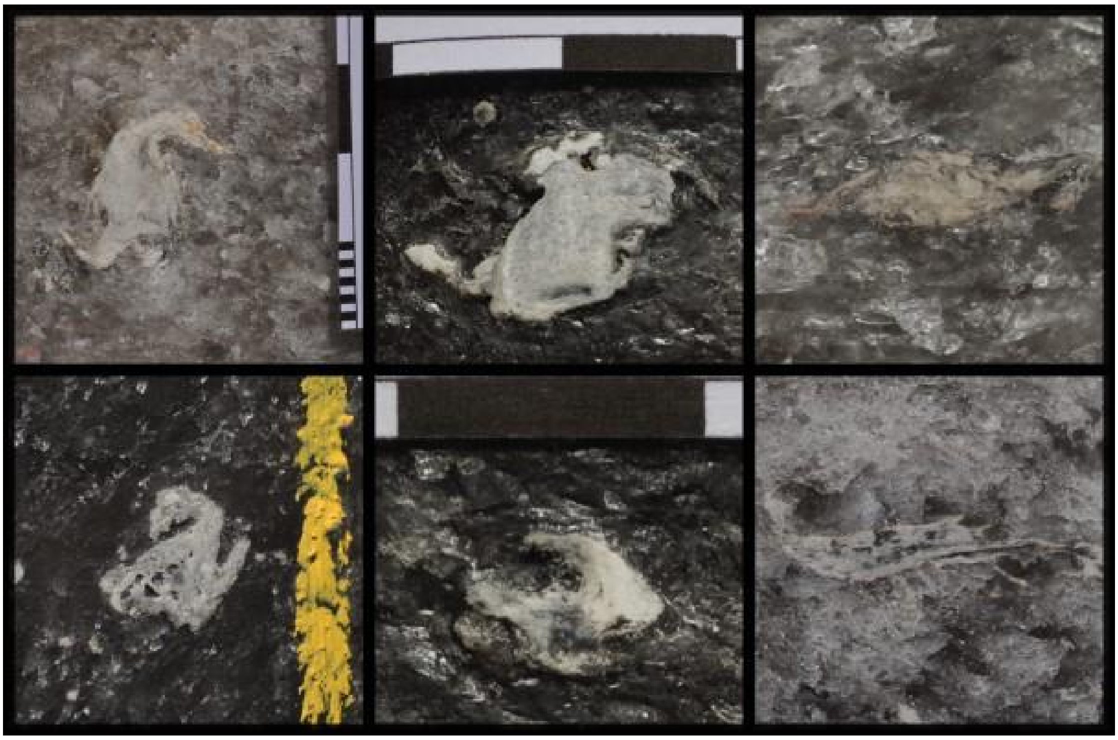

*Fig. 39: Anhydrite winged inclusions in the halite matrix of the Zeglingen Formation; top left to right: BUL1-1B 1247.59m, STA2-1 1173.66m, BAC1-1 1162.92m; bottom left to right: STA2-1 1157.89, STA2-1 1173.72m, BUL1-1B 1248.01m.*

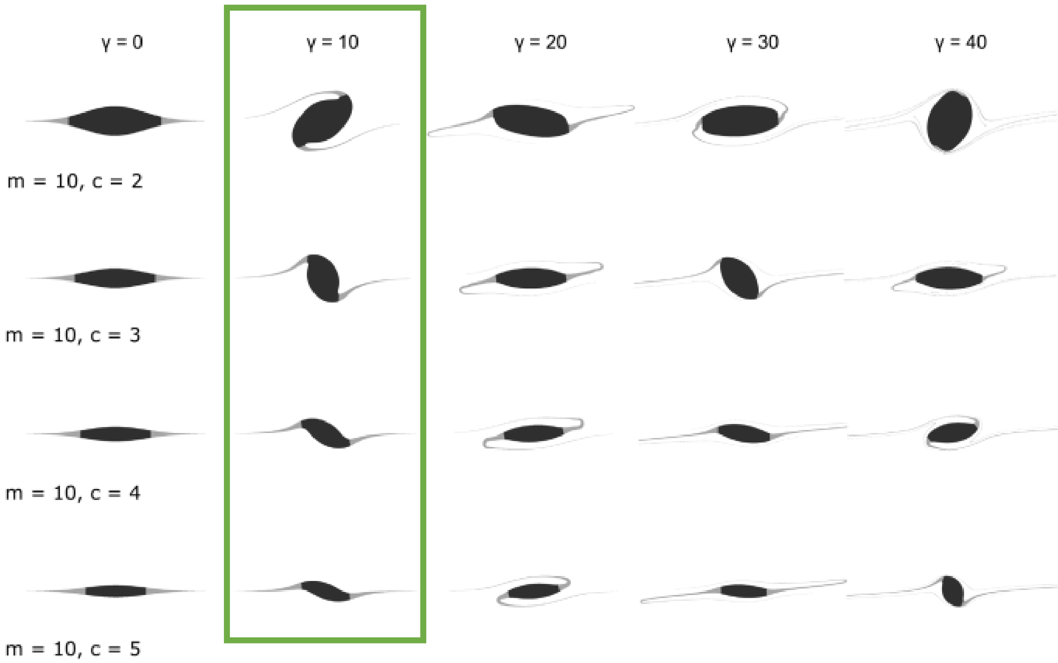


*Fig. 40: Visualisation of the results of 4 linear viscous models with initial shapes c ranging between 2 to 5 and the viscosity ratio of the inclusion and the surrounding matrix m set at 10 (Grasemann & Dabrowski, 2014).*

## 5.3. Survivor grains and sigmoids (sigma clasts)

In the studied bore cores halite survivor grains are located in the halite mylonites and halite breccia of the Zeglingen Fm. (Fig. 41). The amount and size of survivor grains varies throughout the mylonites and breccia. The survivor grains partially developed a shape preferred orientation in the form of sigmoidal structures. Sigma clasts generally consist of a core and recrystallised material in the shape of tails and can be used as kinematic indicators (Simpson & Passier, 1985).

The amount of porphyroclasts within mylonites can be equated to the degree of deformation and strain, meaning protomylonites experienced less deformation than ultramylonites (Fossen, 2010). A larger number of survivor grains is therefore indicative of moderate shear strain.

The mylonitic grains of halite mylonite are sized between 1 to 3mm, with an aspect ratio of 3:1 to 2:1 (length : width) and show a shape preferred orientation, thereby forming a penetrative foliation. Coarser sized halite grains may still be present as survivor grains with sizes of up to a few cm (Fig. 41). The length axis of the survivor grains is often oriented oblique to the penetrative mylonitic foliation.

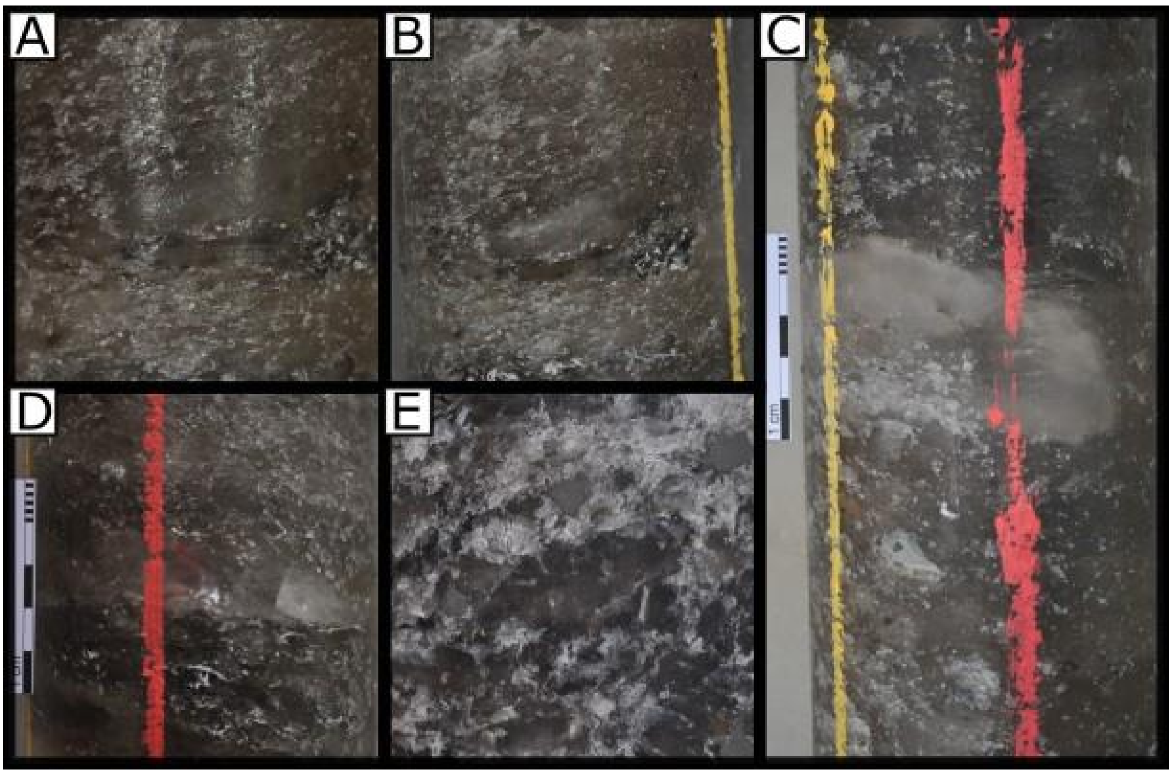


*Fig. 41: A-D: Halite survivor grains in halite matrix. E: Halite sigma clast in halite breccia, trend: top to NE; A: STA2-1 1153.75m, B: STA2-1 1153.74m, C: STA2-1 1165.35, D: STA2-1 1153.92m, E: STA3-1 1153.26m.*

Halite survivor grains in mylonites of the four cores were systematically measured in terms of length, width and dip (Fig. 42). The amount of survivor grains varies between the cores, whereas the aspect ratios are more or less in the same order of magnitude. The mylonites of BUL1-1B contain notably less survivor grains than the mylonitic sections of the other cores. A comparison of the amount of survivor grains with the percentage of mylonites of the overall mylonite thickness (Fig. 43) suggests that the mylonitic sections of BUL1-1B underwent more deformation than the mylonites of STA2-1 or STA3-1. The number of survivor grains per meter halite mylonite, with a value of 2.2 for BUL1-1B and 8.2 for STA2-1, allows similar conclusions to be drawn. The displayed calculations therefor allow for a relative division of the cores in terms of amount of deformation and strain within the mylonitic sections increasing from STA2-1 to STA3-1 to BAC1-1 and BUL1-1B.

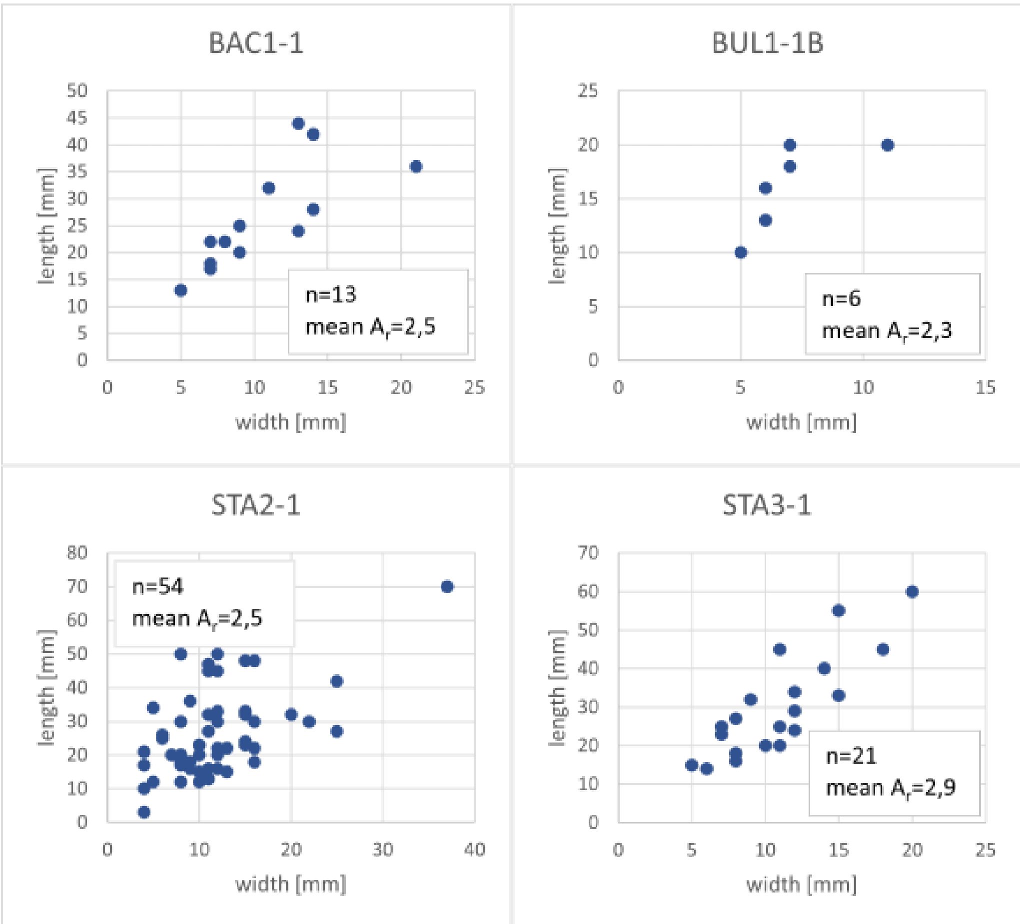


*Fig. 42: Aspect ratios of halite survivor grains in halite mylonites. The total number of measured survivor grains throughout the mylonitic sections of the respective borehole is represented by n. $A_r$ is the mean aspect ratio of survivor grains calculated for each individual core.*

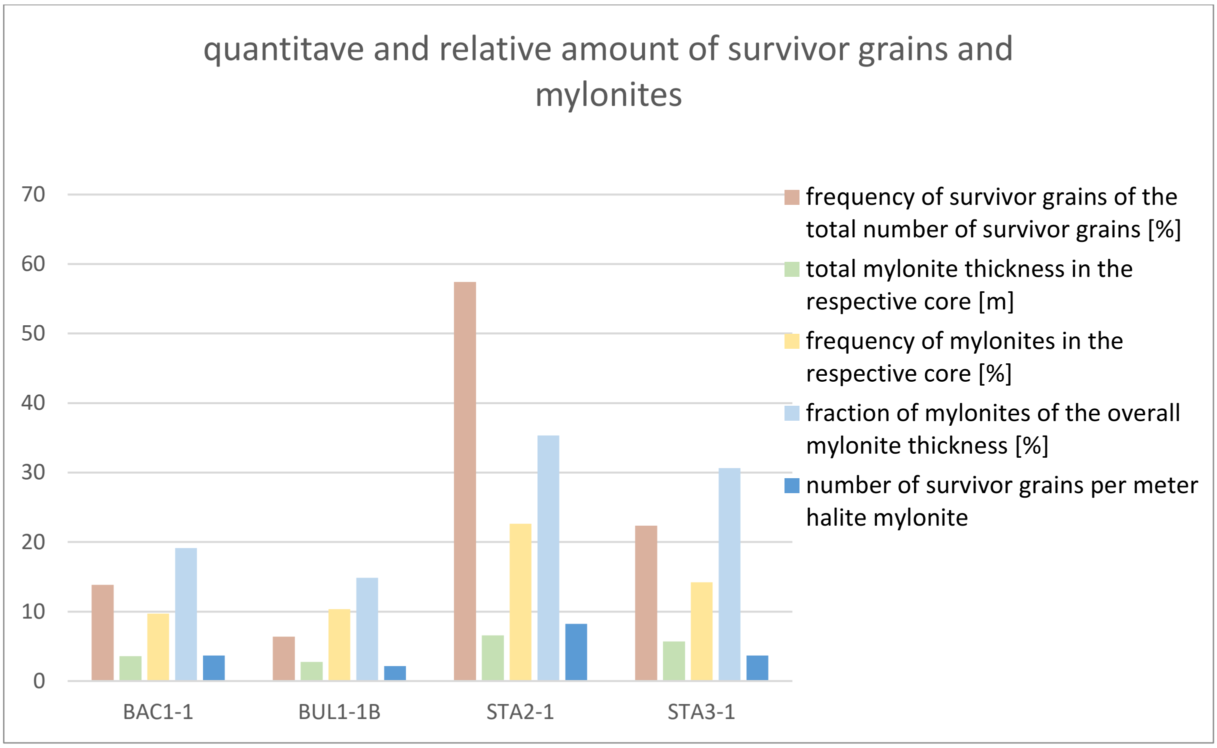


*Fig. 43: Brown columns show the frequency of survivor grains of individual cores as a percentage of the total number of survivor grains of all four cores. Green columns represent the total thickness of halite mylonite within each borehole in meters. Yellow columns display the frequency of halite mylonites compared to the total thickness of the analysed evaporite section of the "Salzlager". Light blue columns represent the frequency of mylonites within an individual core compared to overall mylonite thickness between all four cores. Dark blue columns represent the ratio of total number of survivor grains per meter halite mylonite of each core.*

## 5.4. Shear bands

The length and thickness of shear bands, starting and terminating within the core, localized in halite breccias of STA3-1 in depths of about 1153m were measured as well as the dip and dip direction (Fig. 44). The mean aspect ratio of 7 measured shear bands has a value of 10.75. The grain size of the halite matrix in the section of interest varies between 2 to 6mm. Based on the measured orientations of 15 shear bands two groups of kinematic regimes can be distinguished. Purple-bluish great circles (Fig. 44, b) represent shear bands in a kinematic regime of top NE, which was also confirmed by the presence of sigma clasts showing the same trend (Fig. 41, E). Green great circles (Fig. 44, b) imply a transport direction of top-NW, which, however could not be confirmed by other kinematic indicators within the respective core section.

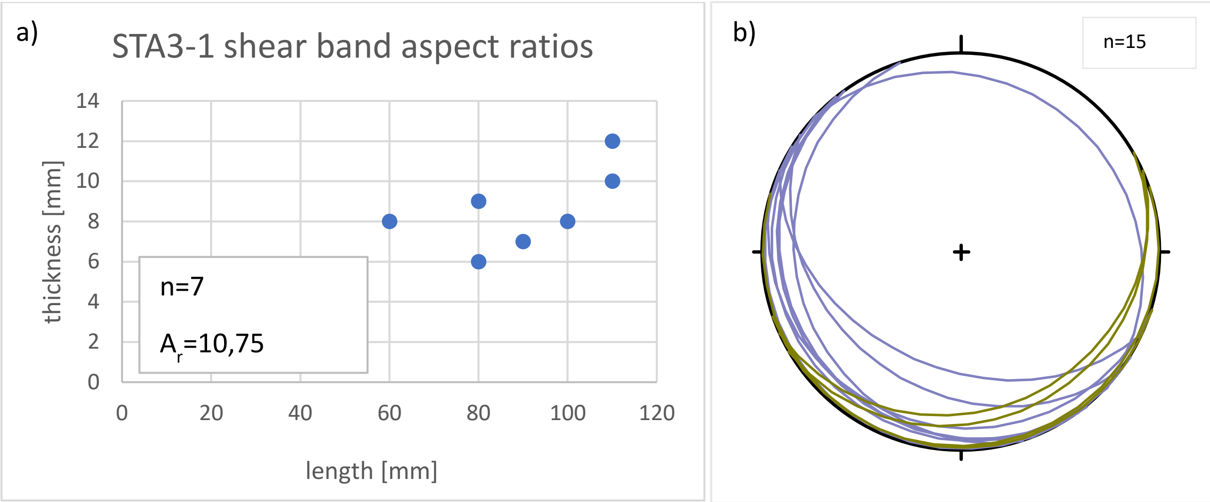


*Fig. 44: Plot of thickness and length (a) and the orientation (b) of shear bands in the cores of STA3-1 in a depth of approximately 1153m.*

In the halite breccia of STA3-1 (1153.44m) a halite survivor grain was dissected and offset by a narrow shear band (Fig. 45). The halite grain therefore can be used as a strain marker to determine the vertical and horizontal offset and subsequently the shear strain. The horizontal offset has a measured value of about 11mm and the vertical offset of approximately 6.5mm. The shear angle has a value of 56.5°. Assuming and applying the concept of simple shear, the shear strain was calculated to be about γ≈1,5. Considering that shear bands are zones of strain concentration, it can be assumed that the overall shear strain in the breccia is even lower.

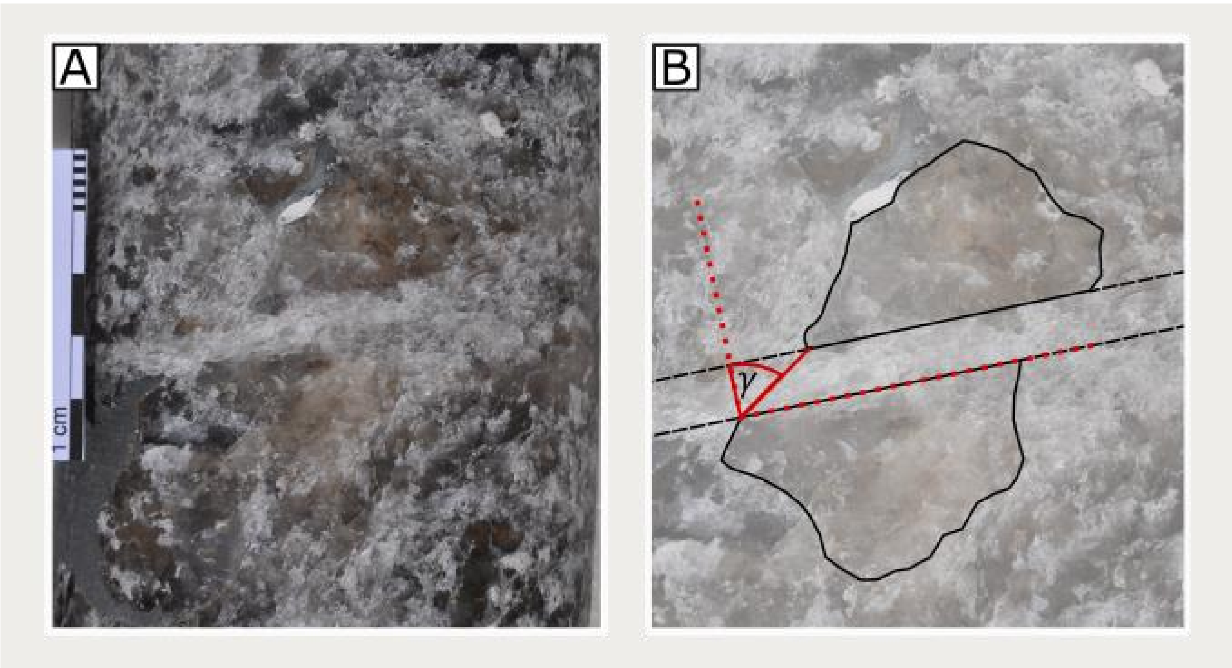


*Fig. 45: A: A halite survivor grain dissected and displaced by a shear band, STA3-1 1153.44m; B: schematic drawing of the vertical and horizontal offset of the two halves of the dissected grain, γ is the shear angle.*

## 5.5. S-C-Mylonites

In S-C-mylonites the angle between S and C varies between 25°- 45°. For shear strain above 10 the angle between S and C gradually decreases until S and C are aligned, resulting in the formation of a composite foliation. Higher shear strains subsequently lead to the formation of a new set of shear bands, oblique to the shear zone margins (Fossen, 2010).

In the cores of STA2-1 S-C structures occurred in halite mylonite sections (Fig. 47). S and C were measured in terms of dip and dip direction (Fig. 46). The dihedral angle between S and C is 26°.

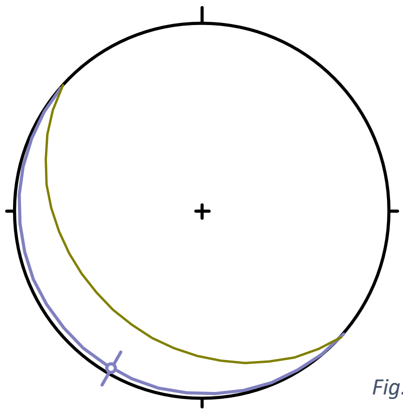

*Fig. 46: Plot of S (green) and C (purple).*

The fact that S and C are not aligned and S is still at an angle to the shear zone margins indicates that the shear strain leading to the formation of the S-C-mylonite was below γ≈10.

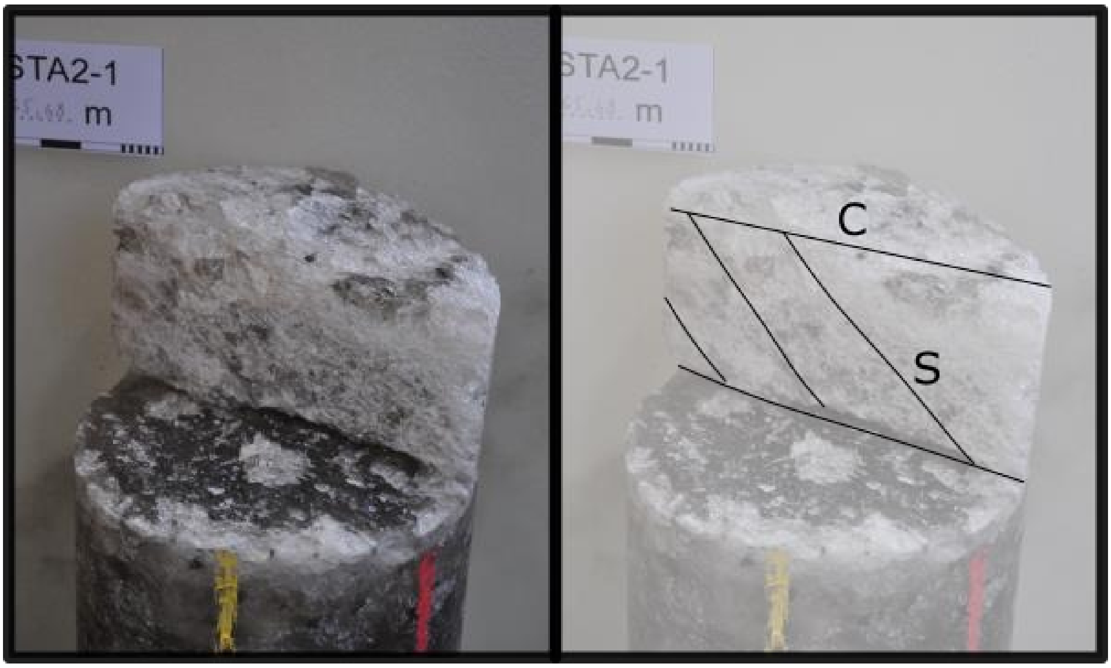


*Fig. 47: S-C pattern indicating a dextral shear zone in halite mylonite of STA2-1 1165.68m.*

# 6. Kinematics and shear-sense indicators

Drill core investigations of the four cores revealed polyphase kinematics with different transport directions, whereby three main transport directions could be identified. Foliation planes and their respective stretching lineations indicate transport top-NW (Fig. 48, a), top-NNE to top-NE (Fig. 48, b) and top-NW (Fig. 48, c).

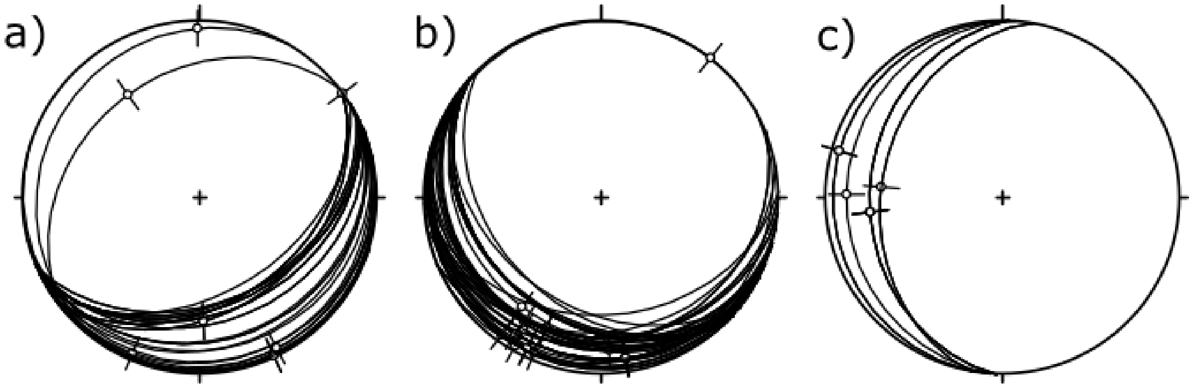


*Fig. 48: Summary stereoplots of stretching lineations on foliation planes of the four investigated boreholes at different depths. a) Stretching lineations indicative of transport top-NW; b) Stretching lineations indicative of transport top-NNE to top-NE; c) Stretching lineations indicating transport top-W.*

A \`V´-pull apart structure could be observed in low viscous deformed halite mylonite of STA2-1 at an approximate depth of 1165.00m. The position of the rotated fragments relative to the shear plane indicate the overall shear sense to be top-NE (Fig. 49).

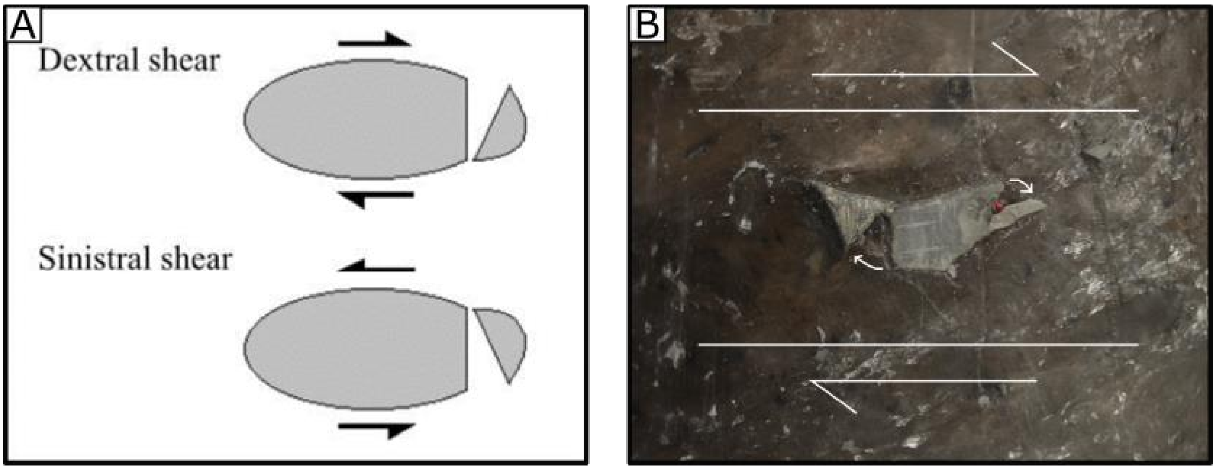


*Fig. 49: A: Development of \`V´-pull-aparts in dextral and sinistral shear (Samanta et al., 2001 after Hippertt, 1993), B: \`V´-pull-apart in halite mylonite of STA2-1 1165.18m, indicating dextral shear, top-NE.*

Opening directions of tension gashes recorded in asymmetric boudins in anhydrite and clay layers of STA2-1 at various depths, reveal both transport top-NNW and transport top-NE (Fig. 50).

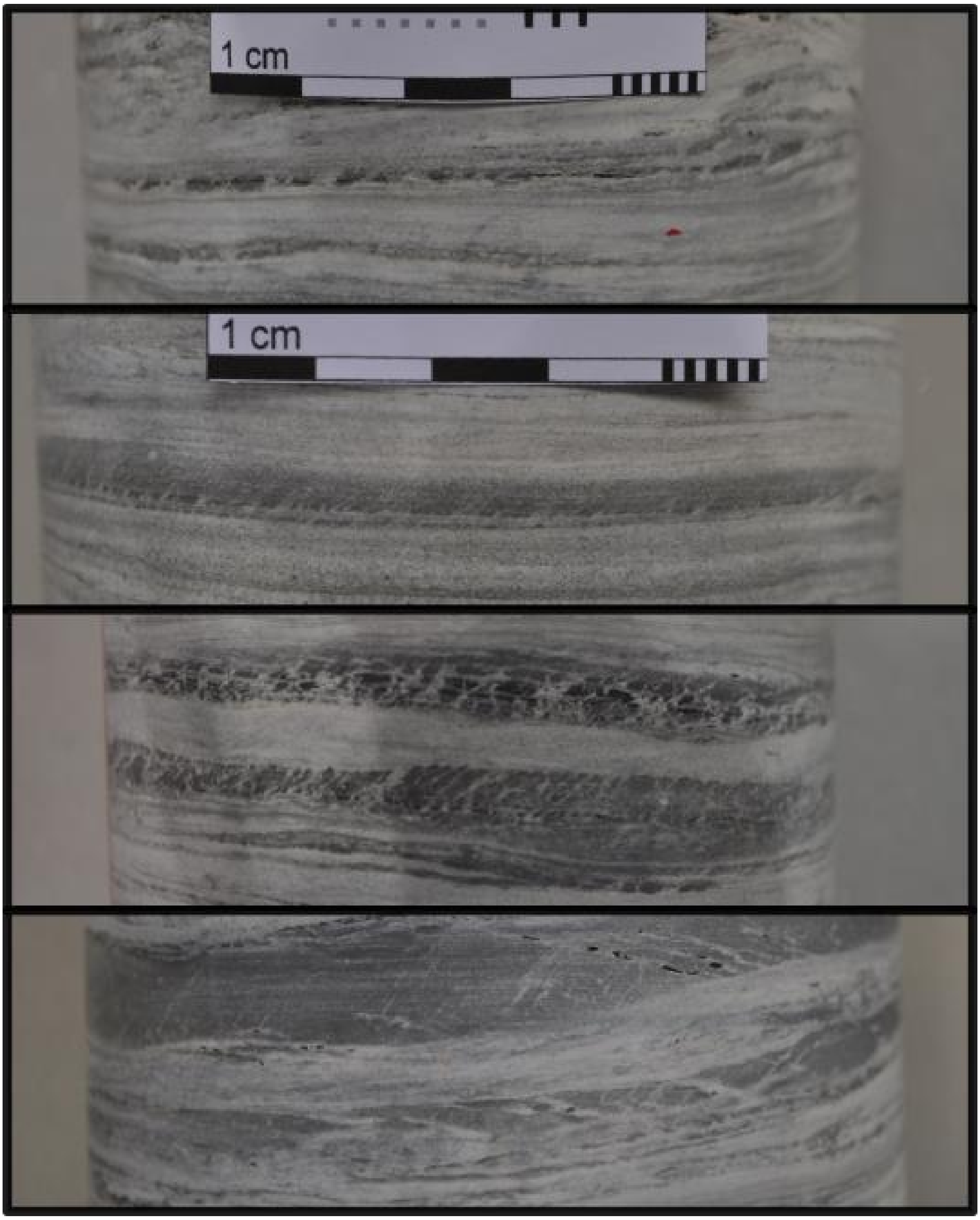


*Fig. 50: Asymmetric boudinage in anhydrite and clay layers. Top 3 indicate transport top-NNW; bottom indicates transport top-NE; top to bottom: STA2-1 1151.36m, STA2-1 1154.50m, STA2-1 1154.95, STA2-1 1166.13m.*

Winged inclusions located in halite mylonite and viscous deformed breccia also show polyphase kinematics with different transport directions. They indicate transport directions of top-NNW (Fig. 51, A), top-N (Fig. 51, B+C), top-NNE (Fig. 51, D), as well as top-NE (Fig. 51, E-H).

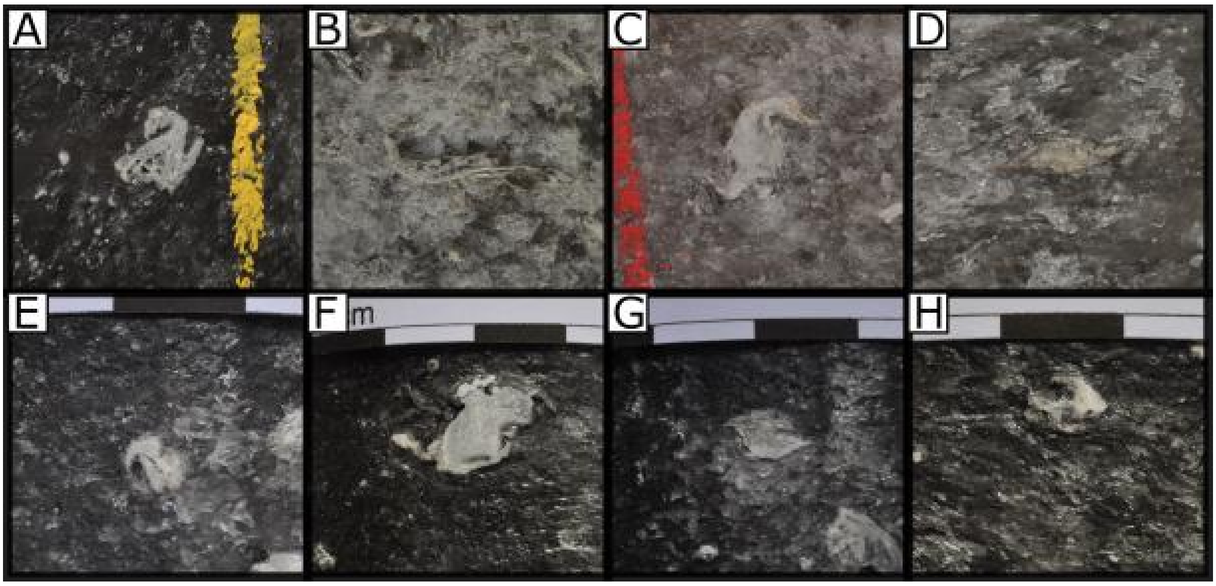


*Fig. 51: Winged inclusions; A: Winged inclusion indicates transport top-NNW, B+C: Winged inclusions indicate transport top-N, D: Winged inclusion indicates transport top-NNE, E-H: Winged inclusions indicate transport top-NE. A: STA2-1 1157.89m, B: BUL1-1B 1247.59m, C: BUL1-1B 1248.01m, D: BAC1-1 1162.92m, E: STA2-1 1173.64m, F: STA2-1 1173.66m, G: STA2-1 1173.67m, H: STA2-1 1173.72m.*

Sigmoidal shaped, cm-sized halite survivor grains, embedded in fine grained halite matrix in the cores of STA3-1 are indicative of transport directions of top-N and top-NW (Fig. 52).


*Fig. 52: Survivor grains, left: sigma clast indicates transport top-N STA3-1 1145.60m, right: sigma clast indicates transport top-NW STA3-1 1153.26m.*

# 7. Shear strain profiles

According to the results gained form the estimations of shear strain presented in the previous chapters a strain profile for each bore was constructed. Core sections were categorised into four groups with shear strain ranging from zero to below fifteen. Thereby strain corresponds to the degree of viscous deformation.

Plots are Schmidt net lower hemisphere projections showing structures as foliations and stretching lineations. Positions in the strain profiles indicate the depths at which the structures were recorded.

## 7.1. STA2-1

Approximately two thirds of the cores of STA2-1 show in different extent signs of viscous deformation. Low to medium degrees of deformation are most frequent. High grades of viscous deformation with strain ranging from $\gamma \approx 7$ to $\gamma \approx 15$ occur only in thin layers of halite mylonites. However, not all mylonites can be equated to high strain as large shares of the mylonitic sections are characterised by the occurrence of abundant and partially large survivor grains, indicating medium strain. Strain analyses carried out on winged inclusions embedded in the mylonitic foliation led to similar conclusions with an estimated strain of approximately $\gamma \approx 10$. One third of the thickness of the "Salzlager" shows no viscous deformation. The respective lithologies are undeformed halite, anhydrite and clay.

Stereonets display dip and dip direction of the mylonitic foliation and if present the plunge and azimuth of the corresponding lineation. Stretching lineations indicate transport top-NNE (1166.00m), top-NNW (1157.50m) as well as top-W (1164.50m) (Fig. 53).

## 7.2. STA3-1

The cores of STA3-1 are in equal parts viscous undeformed and deformed. Other than in STA2-1, however, low to medium grade viscous deformation occurs only approximately twice as frequently as strains of $\gamma \approx 7$ to $\gamma \approx 15$. Shear strain of $\gamma \approx 2$ to $\gamma \approx 7$ is assigned to viscous deformed breccia and mylonites. Undeformed sections consist in large parts of the lithological groups of anhydrite and clay and of halite with seams of clay.

Displayed stereoplots show the orientation of the mylonitic foliation and of the corresponding lineation. Stretching lineations mostly indicate top-NNE (Fig. 54).

### 7.3. BUL1-1B

Nearly all core sections of BUL1-1B are viscous deformed to some degree with strains of $\gamma<2$ being most common. High strains of $\gamma\approx7$ to $\gamma\approx15$ are relatively rare. Only small sections of the cores are viscous undeformed.

As low viscous deformed breccia is the most common lithotype in BUL1-1B foliations are often not penetrative as they get deflected by larger clasts or survivor grains. However, lineations are measurable at core breaks and are displayed in the shown stereoplots (Fig. 55). Stretching lineations indicate both, transport top-NNE (1259.50m) and top-NNW (1255.5m).

### 7.4. BAC1-1

The cores of BAC1-1 are to a great extent undeformed with respect to viscous deformation. The section mostly consists of authigenic halite breccia and undeformed layers of anhydrite and clay. Sections correlating to halite mylonite are viscous deformed with low to medium strain being most common.

Besides mylonitic foliation in the viscous deformed sections, the orientation of stylolithic layers is also presented in the stereoplots of the undeformed sections (1160.50m). Plotting of stylolithic layers in the Schmidt net visualises the shallow dipping of these layers, which are more or less horizontal with dip angles below 5°. Stretching lineations indicate both, transport top-NNE (1186.50) and top-NNW (1170.70) (Fig. 56).

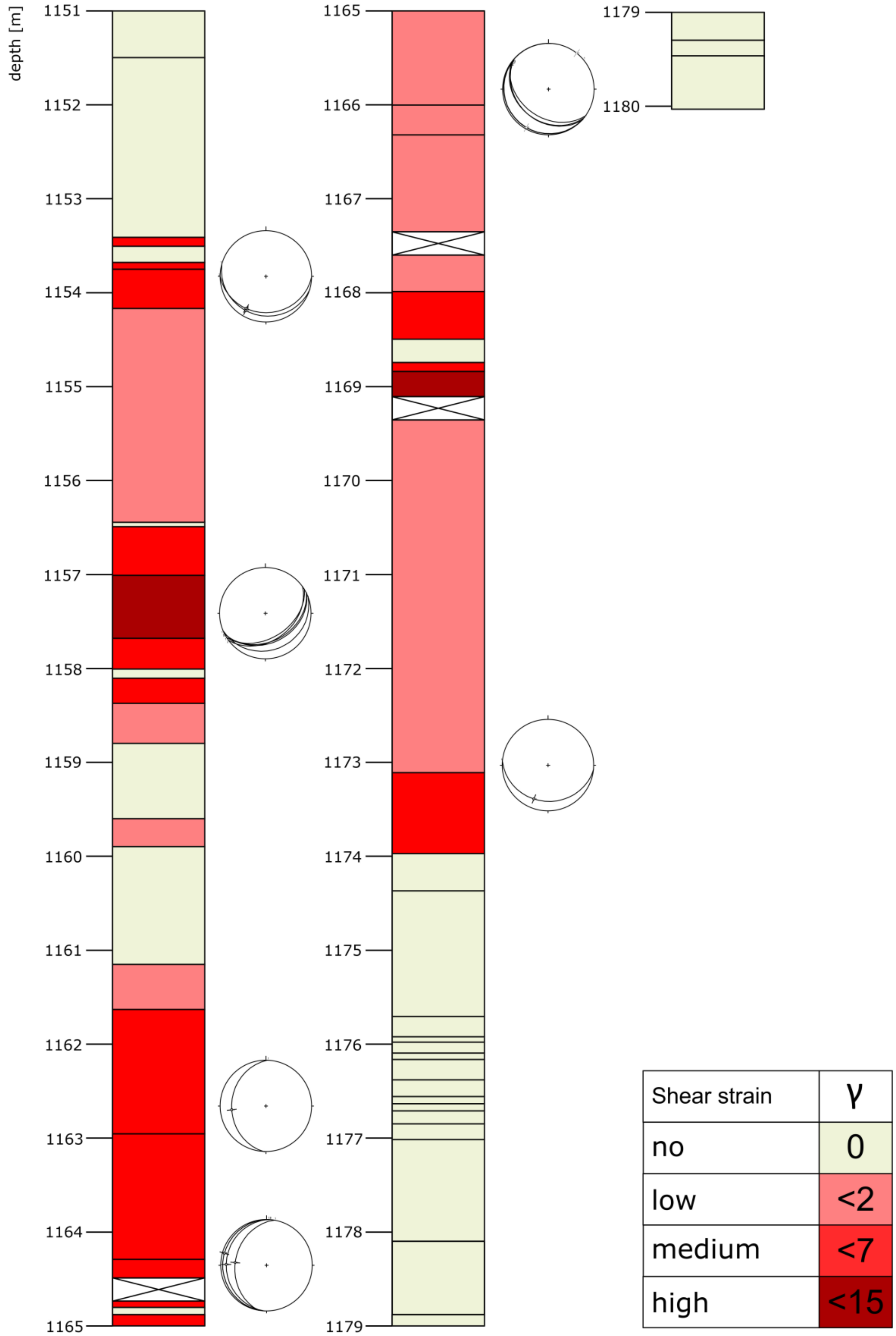


*Fig. 53: Strain profile of STA2-1. Stereoplots show the orientation of the mylonitic foliation and of the corresponding stretching lineation. Crossed sections represent core loss.*

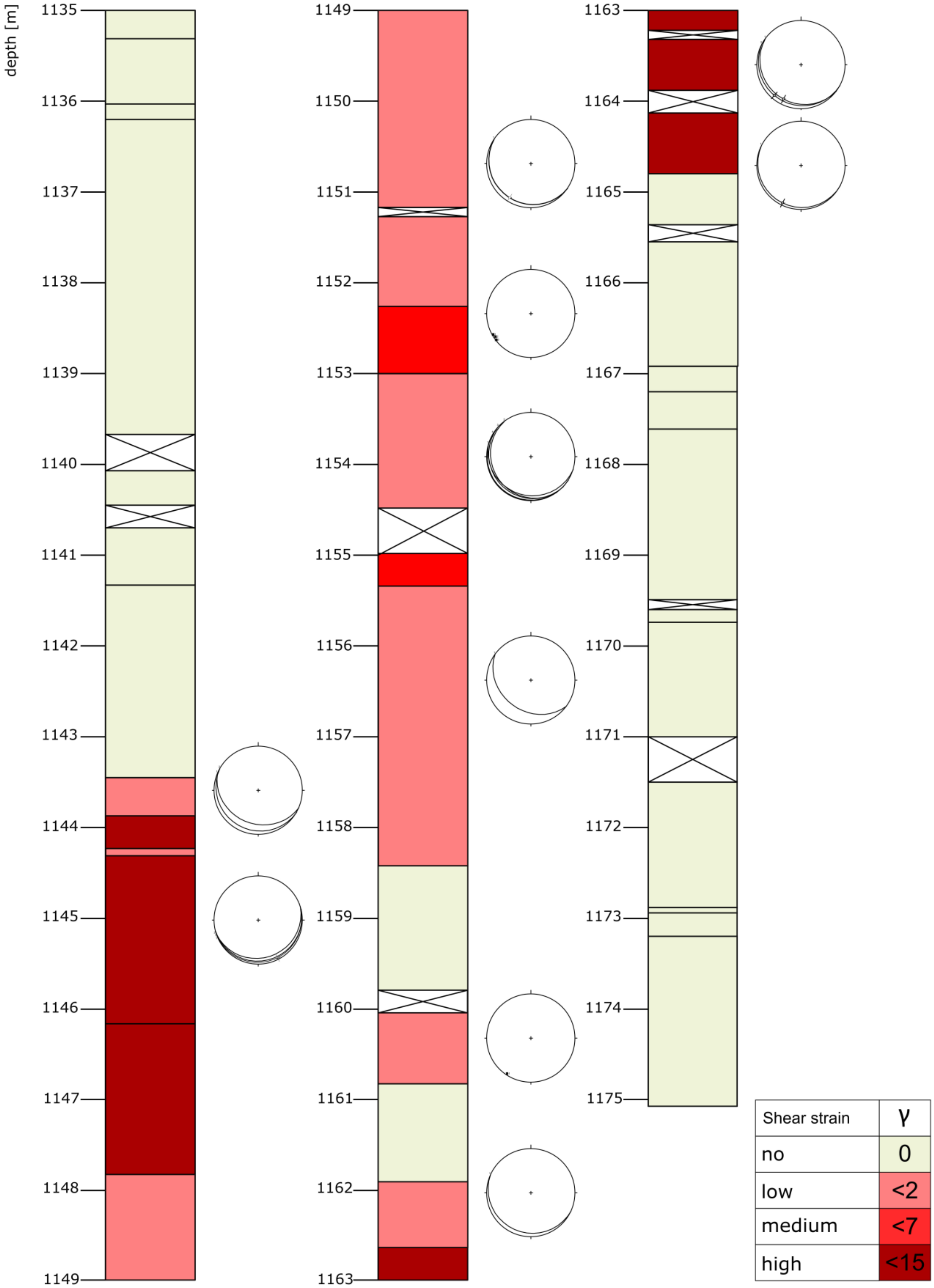


*Fig. 54: Strain profile of STA3-1. Stereoplots show the orientation of the mylonitic foliation and of the corresponding stretching lineation. Crossed sections represent core loss.*

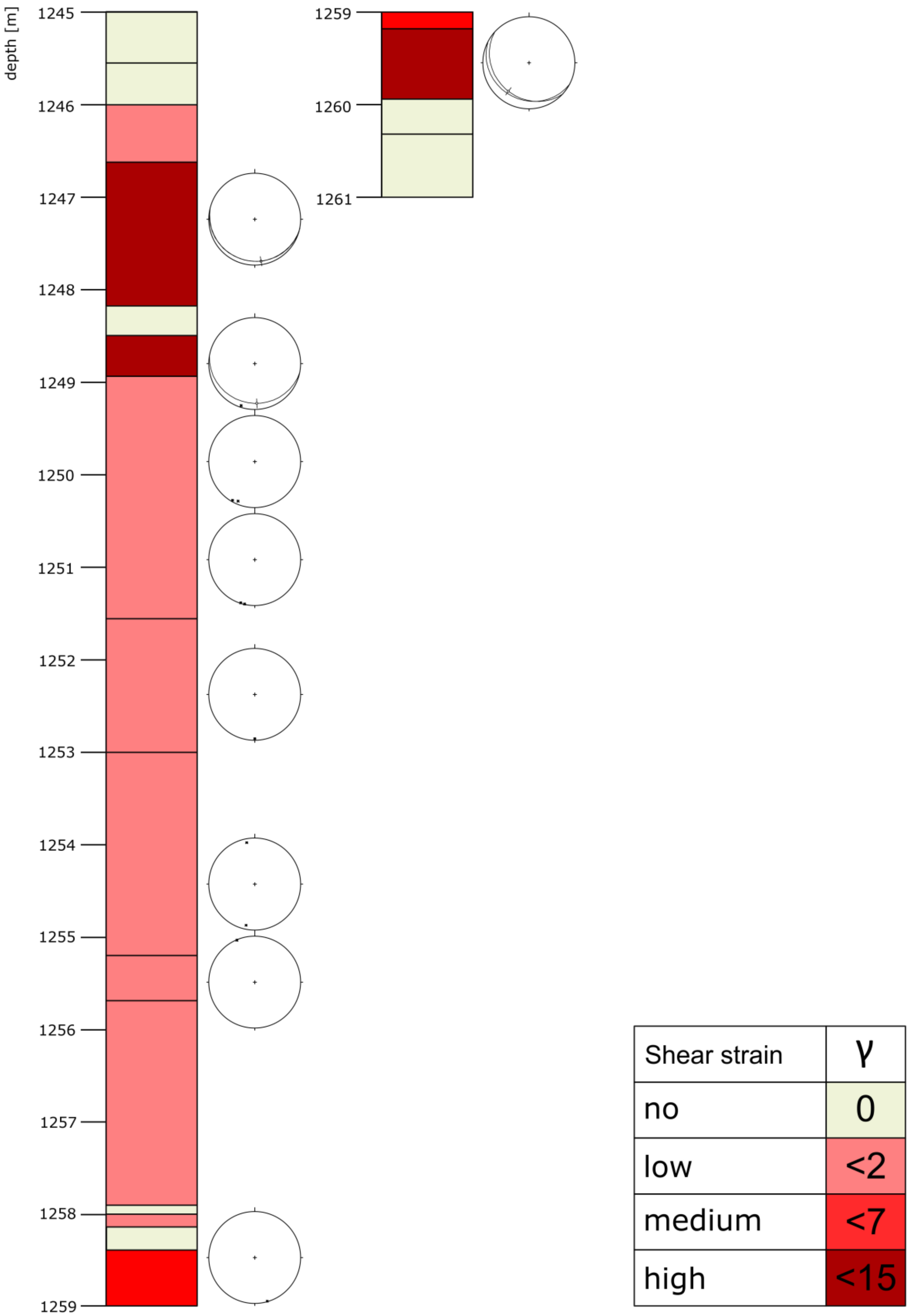


*Fig. 55: Strain profile of BUL1-1B. Stereoplots show the orientation of the mylonitic foliation and of the corresponding stretching lineation, measured at core breaks of viscous deformed halite breccia.*

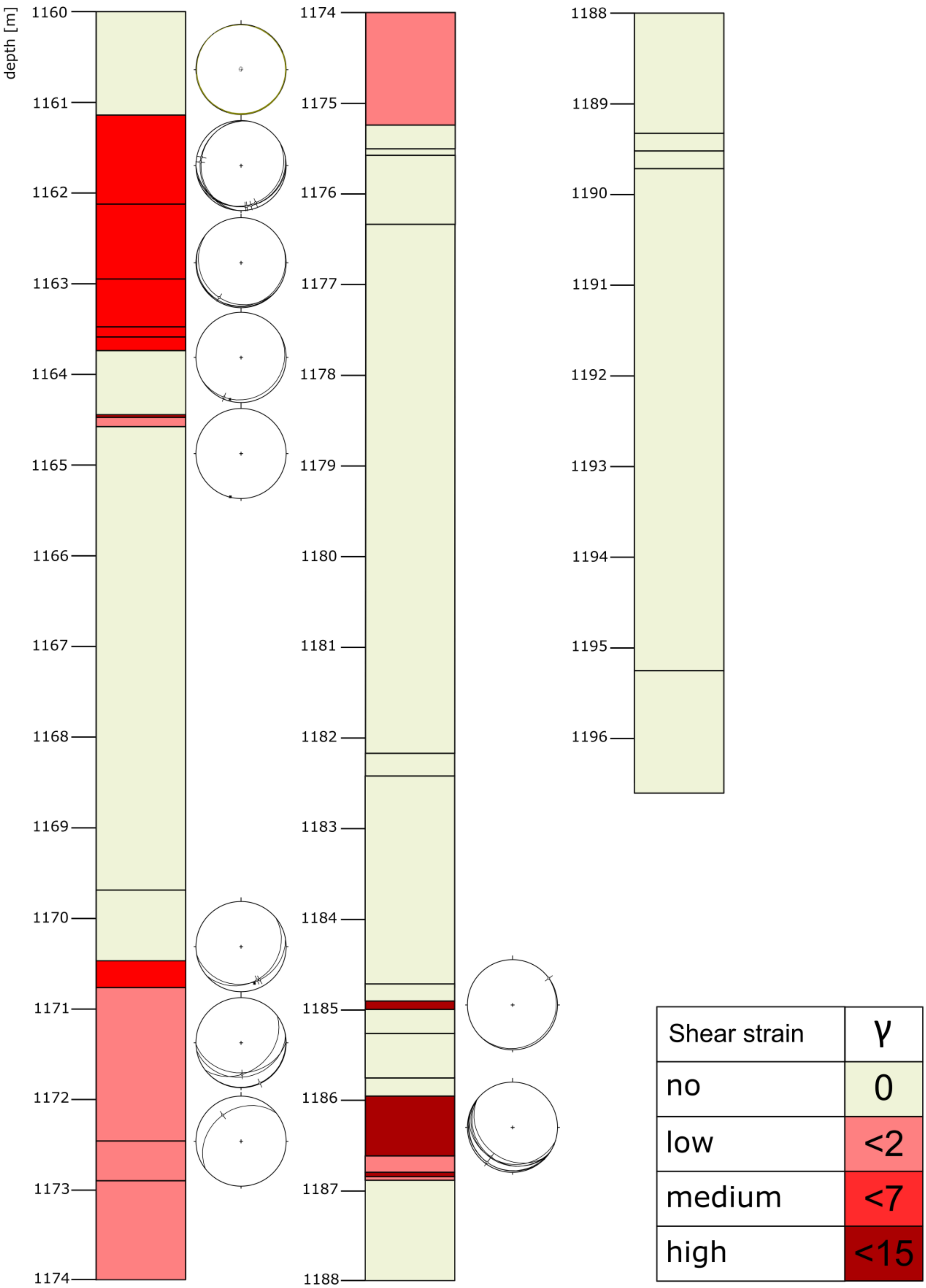


*Fig. 56: Strain profile of BAC1-1. Stereoplots show the orientation of the mylonitic foliation and of the corresponding lineation. Stereoplots next to undeformed sections display the orientation of stylolithic clay layers.*

## 7.5. Strain and strain rate

The division of cores according to the degree of viscous deformation and therefore strain, allows for a calculation of average strain and total displacement for each core, respectively (Table 3). To calculate the displacement the core sections for each core and the four groups of different shear strain as described in chapter 7 were accumulated and multiplied with their respective value of strain. The average strain is the result of the sum of the thickness-shear strain products for each strain category, divided by the total thickness of the "Salzlager" of each well. To calculate the displacement of core loss of STA2-1 and STA3-1, the thickness of core loss was multiplied with the respective average strain of each well. The sum of finite shear strains gives the total displacement for each bore. For all calculations the upper limit of strain of each strain category was used.

*Table 3: Calculation of average strain and total displacement for the four wells STA2-1, STA3-1, BUL1-1B and BAC1-1. T=thickness in m, D=displacement in m. Core loss of STA2-1 (0.83m) and STA3-1 (2.56m) were multiplied with the respective average strain to obtain an estimated value of displacement of these sections. These values where then added to the other values of displacement to calculate the total displacement.*

| Degree of viscous deformation | Strain | **STA2-1** | | **STA3-1** | | **BUL1-1B** | | **BAC1-1** | |
|---|---|---|---|---|---|---|---|---|---|
| | | T [m] | D [m] | T [m] | D [m] | T [m] | D [m] | T [m] | D [m] |
| γ=0 | 0 | 11,115 | 0 | 19,72 | 0 | 2,73 | 0 | 28,19 | 0 |
| γ<2 | 2 | 9,93 | 25,94 | 10,9 | 21,8 | 9,72 | 19,44 | 4,78 | 4,92 |
| γ<7 | 7 | 6,225 | 22,295 | 1,1 | 7,7 | 0,79 | 5,53 | 2,91 | 20,37 |
| γ<15 | 15 | 0,94 | 14,1 | 5,7 | 85,5 | 2,76 | 41,4 | 0,76 | 11,4 |
| Average strain | | 2,75 | | 3,07 | | 4,15 | | 1,13 | |
| Total displacement | | 79,82 | | 122,87 | | 66,37 | | 41,33 | |

Total displacement accommodated by the evaporites of the "Salzlager" of STA2-1, STA3-1, BUL1-1B and BAC1-1 range from ca. 41 to 123m. The maximum value of 122.87m derived for STA3-1 results from the assumption of γ=15 and the compared to the other wells proportionally large thickness of core sections with high strain. A reduction of strain to γ=10 would reduce the total displacement by 28.5m.

The duration of the decoupling process of the Jura fold-and-thrust belt is a matter of discussion with estimated durations between two to ten million years (Jordan, 1987). The endmembers of this time range as well as a duration of seven million years as postulated by Laubscher (1980) were assumed in the course of this study. In the area of interest, a shortening of approximately 150 to 220m had to be accommodated (Jordan et al, 2015). Table

4 to Table 6 contain calculated strain rates for the four bores for durations of 2, 7 and 10Ma and different values for total displacement.

Strain rates calculated in Table 5 and Table 6 are representative for a shortening of 150m and 220m respectively, provided that the entire deformation was solely accommodated in the "Salzlager" of the Zeglingen Fm.

*Table 4: Strain rates of STA2-1, STA3-1, BUL1-1B and BAC1-1 for decoupling durations of 2, 7 and 10Ma and displacements calculated in Table 3. Values for thickness of the "Salzlager" are derived from core observations.*

| Well | | | STA2-1 | STA3-1 | BUL1-1B | BAC1-1 |
|---|---|---|---|---|---|---|
| Thickness "Salzlager" [m] | | | 29,04 | 40,07 | 16 | 36,64 |
| Total displacement [m] | | | 64,17 | 121,04 | 66,37 | 36,69 |
| Average strain | | | 2,21 | 3,02 | 4,15 | 1,00 |
| Duration of decoupling process | 2 Ma | Strain rate | 3,50E-14 | 4,79E-14 | 6,58E-14 | 1,59E-14 |
| | 7 Ma | | 1,00E-14 | 1,37E-14 | 1,88E-14 | 4,54E-15 |
| | 10 Ma | | 7,01E-15 | 9,58E-15 | 1,32E-14 | 3,18E-15 |

*Table 5: Strain rates of STA2-1, STA3-1, BUL1-1B and BAC1-1 for decoupling durations of 2, 7 and 10Ma and a displacement of 150m, which is necessary to accommodate the total shortening of 150m. Values for thickness of the "Salzlager" are derived from core observations.*

| Well | | | STA2-1 | STA3-1 | BUL1-1B | BAC1-1 |
|---|---|---|---|---|---|---|
| Thickness "Salzlager" [m] | | | 29,04 | 40,07 | 16 | 36,64 |
| Total displacement [m] | | | 150 | 150 | 150 | 150 |
| Average strain | | | 5,17 | 3,74 | 9,38 | 4,09 |
| Duration of decoupling process | 2 Ma | Strain rate | 8,19E-14 | 5,94E-14 | 1,49E-13 | 6,49E-14 |
| | 7 Ma | | 2,34E-14 | 1,70E-14 | 4,25E-14 | 1,85E-14 |
| | 10 Ma | | 1,64E-14 | 1,19E-14 | 2,97E-14 | 1,30E-14 |

*Table 6: Strain rates of STA2-1, STA3-1, BUL1-1B and BAC1-1 for decoupling durations of 2, 7 and 10Ma and a displacement of 220m, which is necessary to accommodate the total shortening of 220m. Values for thickness of the "Salzlager" are derived from core observations.*

| Well | | | STA2-1 | STA3-1 | BUL1-1B | BAC1-1 |
|---|---|---|---|---|---|---|
| Thickness "Salzlager" [m] | | | 29,04 | 40,07 | 16 | 36,64 |
| Total displacement [m] | | | 220 | 220 | 220 | 220 |
| Average strain | | | 7,58 | 5,49 | 13,75 | 6,00 |
| Duration of decoupling process | 2 Ma | Strain rate | 1,20E-13 | 8,70E-14 | 2,18E-13 | 9,52E-14 |
| | 7 Ma | | 3,43E-14 | 2,49E-14 | 6,23E-14 | 2,72E-14 |
| | 10 Ma | | 2,40E-14 | 1,74E-14 | 4,36E-14 | 1,90E-14 |

# 8. Interpretation and Discussion

## 8.1. Mineralogical content and lithological types

Four recently drilled deep bores penetrating the Zeglingen Fm. in Northern Switzerland gave the opportunity to analyse continuous sections through the evaporites of the "Salzlager" with the objective to assess if this stratigraphic interval acted as a detachment horizon accumulating high shear strain during thin-skinned thrusting of the overlying successions of the Jura fold-and-thrust belt. The following interpretation and discussion is based on systematic core analyses of lithologies and deformation structures exposed by the cores of the boreholes STA2-1, STA3-1, BUL1-1B and BAC1-1.

Based on the mineralogical and structural content nine main lithologies could be set up into which the core sections were divided. The groups being: undeformed layers of anhydrite and clay, viscous deformed anhydrite and clay layers, authigenic halite breccia, low viscous deformed breccia, viscous deformed breccia, undeformed coarse-grained halite, viscous deformed halite with seams of clay, halite with stylolithic clay layers and halite mylonite. Recordings of the cores of Schafisheim-well located south of the folded Jura approximately 30km southwest of the studied area describe encountered lithologies similarly (Nagra, 1992). Sections of undeformed laminated anhydrite with sedimentary structures still preserved and the occurrence of up to 5cm large clear, orange halite crystals within the anhydrites are described. In BAC1-1 similar lithologies and structures are observable, with authigenic brown to orange halite crystals growing between anhydrite and clay. Differently to the Schafisheim-well fibrous halite was also seen within these sections of BAC1-1. Halite mylonites are also described in the cores of well Schafisheim with grain sizes of a couple of millimeters, a few anhydrite and clay clasts in the decimeter range and a distinct grain elongation up to 10:1 (Jordan, 1992). Stretching lineations were recorded at core breaks and larger halite survivor grains are described as being embedded into the halite matrix. Halite mylonites of STA2-1 display similar properties except for lithoclasts only having sizes of up to 10cm and aspect ratios of halite grains only ranging from 3:1 to 2:1. As in Schafisheim stretching lineations could be observed at core breaks and survivor grains occur in different sizes and abundances.

Smoke-grey, "dirty" halite was also recorded in the Schafisheim-well and correlates with milky-grey halite with seams of clay observed in the studied cores. Halite with stylolithic clay layers though is not described in the records of Schafisheim.

## 8.2. Strain and strain rate

Based on observed structures as boudins, winged inclusions, survivor grains or shear bands an estimation of strain, ranging between zero and fifteen was obtained. The duration of the decoupling process is a matter of discussion with estimated durations between two to ten million years (Jordan, 1987). A duration of seven million years as postulated by Laubscher (1980) was assumed in the course of this discussion. In the area of interest, a shortening of approximately 150 to 220m is accommodated in the so-called Siglistorf Anticline (Fig. 3; Jordan et al, 2015), which is located north of the investigated boreholes. In a thin-skinned deformation model the whole respective displacement must be accommodated by the regional detachment of the Zeglingen evaporites. Maximum displacements calculated for STA2-1, STA3-1, BUL1-1B and BAC1-1 are 79.82m, 122.87m, 66.37m and 41.33m, respectively. All of these values are lower than the 150 to 220m thrust distances estimated from balanced cross-sections through the study area.

In STA2-1 the Zeglingen Fm. has a thickness of 68.71m. Systematic structural analyses of viscous structures and estimates of the finite shear strain reveal that the evaporite detachment of the "Salzlager" accommodates a maximum displacement of 79.82m. For a total displacement of 150 to 220m resulting values of shear strain range from γ=1.18 to γ=3.20, provided that the entire deformation was solely accommodated by the Zeglingen Fm. and evenly distributed over its entire thickness of 68.71m (Table 1). This results in a strain rate of $9.89 \cdot 10^{-15} \cdot s^{-1}$ and $1.45 \cdot 10^{-14} \cdot s^{-1}$ assuming a deformation time of seven million years. Strain estimations derived from structures recorded in the ca. 27m thick "Salzlager" of STA2-1 result in an average strain of γ=2.75, a total displacement of 79.82m and a strain rate of $1.25 \cdot 10^{-14} \cdot s^{-1}$ (Table 4) for a deformation time of 7Ma. In STA2-1 about 42% of the Zeglingen Fm. are assigned to the "Salzlager". Assuming only thin-skinned deformation processes were active in the formation of the Jura fold-and-thrust belt, the residual amount of shortening of 70.18 to 140.18m had to be accommodated by the rest of the Zeglingen Fm.

In STA3-1 the Zeglingen Fm. has a thickness of ca. 80m, resulting in a strain of γ=1.91 to γ=2.77 for a total displacement of 150m and 220m respectively, provided that the entire deformation was solely accommodated in the Zeglingen Fm. Assuming a deformation time of seven million years results in a strain rate of $8.67 \cdot 10^{-15} \cdot s^{-1}$ and $1.26 \cdot 10^{-14} \cdot s^{-1}$. Structures observed within the "Salzlager" of STA3-1 indicate an average strain of γ=3.07, a total displacement of 122.87m and a strain rate of $1.39 \cdot 10^{-14} \cdot s^{-1}$ (Table 4) for a deformation time of 7Ma. The

"Salzlager" makes up about 50% of the Zeglingen Fm. of STA3-1, meaning the residual shortening of 27.13 to 97.13m has to be accommodated by the remaining parts of the Zeglingen Fm., if assumed only thin-skinned deformation processes were active during thrusting.

In BUL1-1B the Zeglingen Fm. has a thickness of 63.21m. For a total displacement of 150 to 220m resulting values of shear strain range from γ=2.37 to γ=3.48, provided that the entire deformation was solely accommodated in the Zeglingen Fm. Assuming a deformation time of seven million years results in a strain rate of $1.08 \cdot 10^{-14} \cdot s^{-1}$ and $1.58 \cdot 10^{-14} \cdot s^{-1}$. Strain estimations obtained from structures recorded in the "Salzlager" of BUL1-1B result in an average strain of γ=4.15, a total displacement of 66.37m and a strain rate of $1.88 \cdot 10^{-14} \cdot s^{-1}$ (Table 4) for a deformation time of 7Ma. In BUL1-1B only 25% of the Zeglingen Fm. are assigned to the "Salzlager". Assuming only thin-skinned deformation processes were active in the formation of the Jura fold-and-thrust belt, the residual amount of shortening of 83.63 to 153.63m had to be accommodated by the rest of the Zeglingen Fm.

In BAC1-1 the Zeglingen Fm. has a thickness of 77.28m, resulting in a strain of γ=1.41 to γ=2.85 for a total displacement of 150m and 220m respectively, provided that the entire deformation was solely accommodated in the Zeglingen Fm. Assuming a deformation time of seven million years results in a strain rate of $8.79 \cdot 10^{-15} \cdot s^{-1}$ and $1.29 \cdot 10^{-14} \cdot s^{-1}$. Structures observed within the "Salzlager" of BAC1-1 indicate an average strain of γ=1.13, a total displacement of 41.33m and a strain rate of $5.11 \cdot 10^{-15} \cdot s^{-1}$ (Table 4) for a deformation time of 7Ma. The "Salzlager" makes up about 47% of the Zeglingen Fm. of BAC1-1, meaning the residual shortening of 108.67 to 178.67m has to be accommodated by the remaining parts of the Zeglingen Fm., if assumed only thin-skinned deformation processes were active during thrusting.

The comparison of balanced cross-section derived values of total shortening of 150 to 220m (Jordan et al., 2015) with the maximum displacements derived from the "Salzlager" of the four wells in this study, shows that there are significant deviations between the two values. Only for STA3-1 the calculated total displacement comes close to the postulated value. Nevertheless, the values of average strain of STA2-1, STA3-1 and BUL1-1B fall within or even exceed the value ranges of strain calculated for a shortening of 150 to 220m and the respective thickness of the Zeglingen Fm. Only the average strain of BAC1-1 is below the calculated value range for strain for a shortening of 150 to 220m. Therefore, theoretically, for STA2-1, STA3-1 and BUL1-1B the accommodation of the postulated range of shortening would be feasible if the respective remaining sections of the Zeglingen Fm. of each well would have a strain value which coincides with the lower value of the respective calculated range for a shortening of 150 to 220m. For BAC1-1 strain values for the remaining sections of the Zeglingen Fm. would have to be above the estimated strain range to fully accommodate the entire shortening.

## 8.3. Thick-skinned or thin-skinned deformation?

Middle Triassic evaporite successions are known to form a major detachment along the floor thrust of the Jura fold-and-thrust belt (Jordan, 1990). However, recent studies focused on basement folds and their potential involvement in the late-stage evolution of the northern Alpine foreland (Schöpfer et al., 2023; Madritsch et al., 2018). 3D seismic data generated at the Constance-Frick Trough was used to investigate a possible reactivation of normal faults as transpressional/reverse faults at the easternmost tip of the Jura range. Based on the thereby gained information the existence of a regional structural detachment above the Base Mesozoic which acted as a detachment for Cenozoic thrusts is considered unlikely in the area of the Constance-Frick Trough (Schöpfer et al., 2023).

At the cores measured orientations of foliation, stretching lineation, elongated (sigmoidal) grains, shear bands and winged inclusions prove polyphase kinematics with different transport directions arguing against a continuous high-strain detachment.

Total displacements derived from the cores of the respective "Salzlager" are considerably lower than the postulated shortening of 150 to 220m. If the remaining amount of shortening was not accommodated by the respective remaining sections of the Zeglingen Fm., thin-skinned deformation alone would not be a sufficient explanation for the accommodation of the overall shortening. However, it has to be stated that the overall shortening varies significantly within the eastern part of the Jura fold-and-thrust belt, thus postulated shortenings may not be applicable for all regions equally. It has also to be taken into account that for the calculation of strain and thus for the total displacement, the highest value of strain was assumed within each strain category. Thus, the overall strain of all sections and therefore the total shortening they accommodated, is likely to be even lower.

Based on recent studies and the calculations and measurements carried out on structures of the investigated four boreholes it is rather likely that the deformation mechanism active in the formation of the Jura fold-and-thrust belt is in fact a combination of thin-skinned and thick-skinned tectonics.

# 9. Conclusion

NAGRA has recently drilled four deep core drillings penetrating the evaporitic succession of the Zeglingen Fm. in the "Vorfaltenzone" of the easternmost part of the Jura fold-and-thrust belt. The cores mainly consist of halite, anhydrite and clay in different quantities and degrees of viscous deformation. Based on mineralogical content and degree of deformation core sections were divided into different lithological units and summarised in lithological profiles. A model describing the probable sedimentary, early diagenetic and deformational evolution of the different evaporitic rock types was elaborated. It is shown that the evaporitic sequence of the Zeglingen Fm. consists of alternations of undeformed and viscous deformed halite and anhydrite. Undeformed sections still show primary sedimentary structures such as depositional laminae or ripples and undeformed Hopper halite crystals. It can be shown that authigenic halite breccias develop through the growth of early diagenetic authigenic halite in joints and between layers of anhydrite and clay. This type of breccia is viscous undeformed proving that halite-anhydrite-clay breccias do not solely result from tectonic deformation. Viscous deformation leads to the formation of a more or less penetrative foliation within the halite-breccias. Foliation is deflected by clay and anhydrite lithoclasts. Shear bands are observed in the more deformed breccias.

Mylonitic halite differs macroscopically from the other lithotypes due to its fine grained halite matrix with grains sized between 1 to 3mm, aspect ratios of 3:1 to 2:1 (length : thickness) and shape preferred orientation. Halite mylonites display a penetrative foliation and stretching lineation. Mylonitised halite frequently contains coarser sized halite survivor grains with sizes up to a few cm and length axes oriented oblique to the penetrative mylonitic foliation. Variably oriented stretching lineations along with sigma clasts and other shear sense indicators (shear bands, winged inclusions, asymmetrical boudins, `V´-pull-aparts) prove polyphase kinematics with different transport directions arguing against a continuous high-strain detachment. Recorded shear directions are top-NNW, top-NNE and top-W.

Winged inclusions, relatively high angles between S and C planes in shear bands, elongations calculated from boudinaged layers and the abundance and sizes of survivor grains are used to estimate the finite shear strain for the different lithotypes. Lithotypes are categorised in coaxial ($\gamma=0$), low shear strain ($\gamma<2$), medium shear strain ($\gamma<7$), and high shear strain ($\gamma<15$). Finite shear strain (expressed by the tangent of the shear angle $\psi$) ranges from zero to below fifteen, with highest strain only occurring in thin halite layers. The total displacement accommodated by the analysed sections of the "Salzlager" are calculated from the sum of the thickness-shear strain products for each strain category revealing the following displacements: STA2-1: 79.82m; STA3-1: 122.87m; BUL1-1B: 66.37m; BAC1-1: 41.33m. It has to be considered that for the calculation of strain and displacement, the highest value of strain was assumed within each strain category. Thus, the finite strain of all sections and therefore the total displacement they accommodated, is likely to be even lower.

Thin-skinned deformation models for the area of interest state a shortening of approximately 150 to 220m of the Jura fold thrust-belt which is accommodated in the so-called Siglistorf Anticline north of the investigated boreholes. Values are estimated from balanced cross-sections through the study area (Jordan et al., 2015). In this thin-skinned model the whole respective displacement of 150 to 220m must be accommodated by the regional detachment of the Zeglingen evaporites. However, the total maximum displacements derived from the cores of the "Salzlager" in this study are considerably lower than 150 to 220m. If the higher values estimated from cross sections apply, the respective deformation cannot be accommodated in evaporites of the "Salzlager" and other detachments in the Zeglingen Fm. would also have to be involved in the decoupling process to make the accommodation of the postulated thrust distance feasible.

Alternatively, some of the overall shortening compensated by the Siglistorf Anticline north of the boreholes could be due to the involvement of the basement (e.g., Schöpfer et al., 2023), implying thick-skinned deformation.

Based on recent studies (Madritsch et al., 2024) and the calculations and measurements carried out on structures of the investigated four boreholes it is rather likely that the deformation mechanism active in the formation of the easternmost tip of the Jura fold-and-thrust belt is in fact a combination of thin-skinned and late stage thick-skinned tectonics.

# 10. References


Adamuszek, M., Dabrowski, M., Schmalholz, S. M., Urai, J. L. and Raith, A. (2015): Estimating Rheological Parameters of Anhydrite from Folded Evaporite sequences: Implications for Internal Dynamics of Salt Structure, EGU General Assembly 2015, held 12-17 April, 2015 in Vienna, Austria. id.9954, 2015 EGUGA..17.9954A.

Ammen, M. & Palten, P.-J. (2021): TBO Bülach-1-1: Data Report Dossier I Drilling. Nagra Arbeitsbericht NAB 20-08-I.

Arslan, A., Passchier, C. W. & Koehn, D., (2008): Foliation boudinage, Journal of Structural Geology, Volume 30, Issue 3, 2008, Pages 291-309, ISSN 0191-8141, https://doi.org/10.1016/j.jsg.2007.11.004.

Becker, A., (2000): The Jura Mountains—an active foreland fold-and-thrust belt? Tectonophysics 321, 381–406.

Bock, H. & Simon, T. (2009): Steinsalzverbreitung im Mittleren Muschelkalk in Baden-Württemberg und der angrenzenden Schweiz. 1 map; Freiburg i.Br. (Landesamt für Geologie, Rohstoffe und Bergbau). (http://www.lgrb-bw.de/download_pool/steinsalzverbreitung.pdf).

Cladouhos, T. (1999): Shape preferred orientations of survivor grains in fault gouge. Journal of Structural Geology. 21. 419-436. 10.1016/S0191-8141(98)00123-0.

Coward, M. P. (1983): Thrust tectonics, thin skinned or thick skinned, and the continuation of thrusts to deep in the crust, Journal of Strutural Geology, 5, Issue 2, 113–123, 1983.

Diebold, P., & Noack, T. (1997): Late Paleozoic troughs and tertiary structures in the eastern Folded Jura. In O. A. Pfiffner, et al. (Eds.), Results of NRP 20 (p. 59–63). Basel: Birkhäuser.

Dronkert, H. (1987): Diagenesis of Triassic evaporites in northern Switzerland: Eclogae Geologicae Helvetiae 8 , 1987.

Dronkert, H. & Bläsi, H.R. & Matter, A. (1990): Facies and Origin of Triassic Evaporites from the NAGRA boreholes, Northern Switzerland.

Fossen, H. (2010) Structural Geology. Cambridge University Press, Cambridge, 463. https://doi.org/10.1017/CBO9780511777806.

Gardner, R.L., Piazolo, S., & Daczko, N.R. (2016): Shape of pinch and swell structures as a viscosity indicator: Application to lower crustal polyphase rocks,Journal of Structural Geology, Volume 88, 2016, Pages 32-45, ISSN 0191-8141, https://doi.org/10.1016/j.jsg.2016.04.012.

Giamboni, M., Wetzel, A., Niviere, B., Schumacher, M. (2004): Plio-Pleistocene folding in the southern Rhinegraben recorded by the evolution of the drainage network (Sundaau area; northwestern Switzerland and France). Eclogae Geol. Helv. 97, 17–31.

Goscombe, B. D., Passchier, C. W., & Hand, M., (2004): Boudinage classification: end-member boudin types and modified boudin structures, Journal of Structural Geology, Volume 26, Issue 4, 2004, Pages 739-763, ISSN 0191-8141, https://doi.org/10.1016/j.jsg.2003.08.015.

Hambrey, M. J., & Milnes, A. G., (1975): Boudinage in glacier ice—some examples. Journal of Glaciology, 14(72), 383-393.

Hanmer, S., (1990): Natural rotated inclusions in non-ideal shear, Tectonophysics, Volume 176, Issues 3–4, 1990, Pages 245-255, ISSN 0040-1951, https://doi.org/10.1016/0040-1951(90)90072-G.

Hanmer, S., Passchier, C.W. (1991): Shear sense indicators: a review. Pap. Geol. Surv., Can. 90, 1e71.

Henk, A., & Timmerman, M. J. (2005): EUROPE—Permian basins. In R. C. Selley, L. R. Cocks, & I. R. Plimer (Eds.), Encyclopedia of geology (pp. 95–102). Amsterdam: Elsevier Ltd.

Hippertt, J. F., (1193): `V´-pull-apart microstructures: a new shear sense indicator, Journal of Structural Geology 15, 1393-1404, 1993.

Homberg, C., Bergerat, F., Philippe, Y., Lacombe, O., Angelier, J. (2002): Structural inheritance and cenozoic stress fields in the Jura fold-and-thrust belt (France). Tectonophysics 357, 137–158.

Jordan, P., (1987): Eine Methode zur Abschätzung tektonischer Scherraten aufgrund mikrostruktueller Beobachtungen, Eclogae Geologicae Helvetiae, vol. 80, 491-508, August 1987.

Jordan, P. & Nüesch, R. (1989): Deformation structures in the Muschelkalk Anhydrites of the Schafisheim Well (Jura overthrust, northern Switzerland), Eclogae Geologicae Helvetiae, 82/2, 429-454.

Jordan, P., Noack, T. & Widmer, T. (1990): The evaporite sheat zone of the Jura Boundary Thrust: new evidence from Wissen well (Switzerland); Eclogae Geologicae Helvetiae 83/3:525-542 (1990).

Jordan, P., Malz, A., Heuberger, S., Pietsch, J., Kley, J., & Madritsch, H. (2015). Regionale geologische Profilschnitte durch die Nordschweiz und 2D-Bilanzierung der Fernschubdeformation im östlichen Faltenjura (Project Report NAB 14-105). Nagra.

Jordan, P. (2016): Reorganisation of the Triassic stratigraphic nomenclature of northern Switzerland: overview and the new Dinkelberg, Kaiseraugst and Zeglingen formations. Swiss J Geosci 109, 241–255 (2016). https://doi.org/10.1007/s00015-016-0209-4.

Jordan, P. & Deplazes G. (2019): Lithostratigraphy of Consolidated Rocks expected in the Jura Ost, Nördlich Lägern and Zürich Nordost Regions. Nagra Arbeitsbericht NAB 19-14.

Jordan, P., Naef, H., Schürch, P., Schwarz M., Ibele, T., Felber, R. & Gysi, M. (2021): TBO Bülach-1-1: Data Report Dossier III Lithostratigraphy. Nagra Arbeitsbericht NAB 20-08.

Jordan P., Schürich P., Schwarz M., Felber R., Naef H., Ibele T. & Weber H.P. (2022); TBO Stadel-2-1: Data Report Dossier III Lithostratigraphy. Nagra Arbeitsbericht NAB 22-02.

Jordan P., Schürich P., Schwarz M., Felber R., Naef H., Ibele T. & Casanova F. (2023): TBO Bachs-1-1: Data Report Dossier III Lithostratigraphy. Nagra Arbeitsbericht NAB 22-04.

Lacombe, O. & Bellahsen, N. (2016): Thick-skinned tectonics and basement-involved fold–thrust belts: Insights from selected Cenozoic orogens. Geological Magazine, 153(5/6), 763–810.

Laubscher, H.P. (1965): Ein kinematisches Modell der Jurafaltung, Eclogae Geologicae Helvetiae, 58/1, 221-228.

Laubscher, H. P. (1980): Die Entwicklung des Faltenjuras – Daten und Vorstellungen, N. Jb. Geol. Paläont. Abh, 160, 28-320.

Kuhn, M. R. (2017): Granular Geomechanics, Elsevier Science and Technology 2017.

Madritsch, H., Schmid, S. M., & Fabbri, O. (2008): Interactions between thin- and thick-skinned tectonics at the northwestern front of the Jura fold-and-thrust belt (eastern France). Tectonics, 27, TC5005. https://doi.org/10.1029/2008TC002282.

Madritsch, H., Naef, H., Meier, B.P., Franzke, HJ. & Schreurs, G. (2018): Architecture and Kinematics of the Constance-Frick Trough (Northern Switzerland): Implications for the Formation of Post-Variscan Basins in the Foreland of the Alps and Scenarios of Their Neogene Reactivation. Tectonics. 37. 10.1029/2017TC004945.

Madritsch, H., Looser, N., Schneeberger,R., Wohlwend, S., Guillong, M., & Malz,A. (2024): Reconstructing the evolution offoreland fold-and-thrust belts using U-Pbcalcite dating: An integrated case-studyfrom the easternmost Jura Mountains(Switzerland). Tectonics, 43,e2023TC008181. https://doi.org/10.1029/2023TC008181.

Malz, A., Madritsch, H. & Kley, J. (2015). Improving 2D seismic interpretation in challenging settings by integration of restoration techniques: A case study from the Jura fold-and-thrust belt (Switzerland). Interpretation 3(4): SAA37-SAA58. https://doi.org/10.1190/INT-2015-0012.1.

McCann, T., Pascal, C., Timmerman, M. J., Krzywiec, P., López-Gómez, J., Wetzel, A., (2006): Post-Variscian (end Carboniferous – Early Permian) basin evolution in Western and Central Europe. In D. G. Gee, & R. A. Stephenson (Eds.), European Lithosphere Dynamics (pp. 355–388). London: Geological Society.

Mosar, J. (1999): Present-day and future tectonic underplating in the western Swiss Alps: Reconciliation of basement/wrench-faulting and décollement folding of the Jura and Molasse basin in the Alpine foreland. Earth and Planetary Science Letters, 173, 143–155. https://doi. org/10.1016/S0012-821X (99)00238-1.

Mukhopadhyay, M., Roy, A., Mandal, N. (2022): Mechanisms of shear band formation in heterogeneous materials under compression: The role of pre-existing mechanical flaws. ESS Open Archive . December 05, 2022.

Nagra (2019). Preliminary horizon and structure mapping of the Nagra 3D seismics NL-16 (Nördlich Lägern) in time domain. Arbeitsbericht NAB 18-35, May 2019 Competing deformation models and geological setting.

Nagra. (2021a). TBO Bülach-1-1: Data Report Dossier I-XI (Project Report NAB 20-08). Nagra.

Nagra. (2022a). TBO Stadel-2-1: Data Report Dossier I-XI (Project Report NAB 22-02). Nagra.

Nagra. (2022b). TBO Stadel-3-1: Data Report Dossier I-XI (Project Report NAB 22-01). Nagra.

Nagra. (2022c). TBO Bachs-1-1: Data Report Dossier I-XI (Project Report NAB 22-04). Nagra.

Platt, J. P., & Vissers, R. L. M., (1980): Extensional structures in anisotropic rocks. Journal of structural geology, 2(4), 397-410.

Pfiffner, O. A. (2016): Basement-involved thin-skinned and thick-skinned tectonics in the Alps. Geological Magazine, 153(5–6), 1085–1109.

Pfiffner, A. (2017): Thick-Skinned and Thin-Skinned Tectonics: A Global Perspective; Geosciences 2017, 7(3), 71; https://doi.org/10.3390/geosciences7030071.

Rime, V., Sommaruga, A., Schori, M. & Mosar, J. (2019): Tectonics of the Neuchâtel Jura Mountains: insights from mapping and forward modelling. Swiss Journal of Geosciences. 112. 10.1007/s00015-019-00349-y.

Robertson, S., (1999): BGS Rock Classification Scheme Volume 2, Classification of metamorphic rocks, British Geological Survey, Research Report Number RR 99-02.

Samanta, S. K., Mandal, N. & Chakraborty, C., (2001): Development of different types of pull-apart microstrucutres in mylonites: an experimental investigation, Journal of Structural Geology 24, 1345-1355, 2002.

Schöpfer, K., Decker, K., Nazari, F., and Madritsch, H. (2023): 3D-seismic evidence for thick-skinned tectonics in a ‘classic’ thin-skinned tectonics region (external Alpine foreland, Switzerland), Terra Nova. 2024;36:217–229., DOI: 10.1111/ter.12701.

Schori, M. (2021): The development of the Jura fold-and-thrust belt: pre-existing basement structures and the formation of ramps. GeoFocus, 50: 200 pp. Université de Fribourg, https://doi.org/10.51363/unifr.sth.2022.001.

Sibson, R, H., (1977): Fault rocks and fault mechanisms. Journal of the Geological Society of London, Vol. 133, 191–213.

Simpson, C. & Passchier, C. W., (1985): Porphyroclast systems as kinematic indicators, United States.

Schori, M., Zwaan, F., Schreurs, G. & Mosar, J. (2021): Pre-existing Basement Faults Controlling Deformation in the Jura Mountains Fold-and-Thrust Belt: Insights from Analogue Models; Tectonophysics 814 (2021) 228980.

Sommaruga, A. (1997): Geology of the Central Jura and the Molasse basin: New insight into an evaporitic-basedforeland fold and thrust belt; Mémoire de la société Neuchâteloise des sciences naturelles; Neuchâtel.

Van der Pluijm, B. A. and Marshak, S. (2004): Earth Structure: an introduction to structural tectonics and geology; Second Edition, United States of America, 2004.

Widmer, T. (1991): Zur Stratigraphie und Sedimentologie der Anhydritgruppe (Mittlere Trias) in der Region Liestal-Arisdorf (Baselland, Nordwestschweiz). Beitr. Geol. Schweiz, geotechnische Serie 79, p. 108.

Ziegler, P. A., & Dèzes, P. (2006): Crustal evolution of Western and Central Europe. Geological Society, London, Memoirs, 32, 43–56., https://doi.org/10.1144/gsl.mem.2006.032.01.03.

# 11. Appendix

## 11.1. Depth intervals of the lithological profiles

| STA2-1 | | | |
|---|---|---|---|
| depth interval [m] | | Lithological group | Thickness [m] |
| 1151 | 1151,5 | Undeformed anhydrite and clay | 0,5 |
| 1151,5 | 1153,4 | Halite with stylolithic clay layers | 1,9 |
| 1153,4 | 1153,5 | Halite mylonite | 0,1 |
| 1153,5 | 1153,675 | Viscous undeformed halite with seams of clay | 0,175 |
| 1153,675 | 1153,75 | Halite mylonite | 0,075 |
| 1153,75 | 1154,17 | Halite mylonite | 0,42 |
| 1154,17 | 1156,43 | Deformed anhydrite and clay layers | 2,26 |
| 1156,43 | 1156,48 | Undeformed coarse-grained halite | 0,05 |
| 1156,48 | 1157 | Halite mylonite | 0,52 |
| 1157 | 1157,67 | Halite mylonite | 0,67 |
| 1157,67 | 1158 | Halite mylonite | 0,33 |
| 1158 | 1158,1 | Undeformed coarse-grained halite | 0,1 |
| 1158,1 | 1158,37 | Halite mylonite | 0,27 |
| 1158,37 | 1158,8 | Deformed anhydrite and clay layers | 0,43 |
| 1158,8 | 1159,6 | Undeformed anhydrite and clay | 0,8 |
| 1159,6 | 1159,9 | Deformed anhydrite and clay layers | 0,3 |
| 1159,9 | 1161,15 | Undeformed anhydrite and clay | 1,25 |
| 1161,15 | 1161,63 | Low viscous deformed halite | 0,48 |
| 1161,63 | 1162,95 | Halite mylonite | 1,32 |
| 1162,95 | 1164,28 | Halite mylonite | 1,33 |
| 1164,28 | 1164,48 | Halite mylonite | 0,2 |
| 1164,48 | 1164,73 | Core loss | 0,25 |
| 1164,73 | 1164,8 | Halite mylonite | 0,07 |
| 1164,8 | 1164,88 | Undeformed coarse-grained halite | 0,08 |
| 1164,88 | 1165 | Halite mylonite | 0,12 |
| 1165 | 1166 | Low viscous deformed halite | 1 |
| 1166 | 1166,32 | Deformed anhydrite and clay layers | 0,32 |
| 1166,32 | 1167,35 | Deformed anhydrite and clay layers | 1,03 |
| 1167,35 | 1167,6 | Core loss | 0,25 |
| 1167,6 | 1167,99 | Deformed anhydrite and clay layers | 0,39 |
| 1167,99 | 1168,5 | Halite mylonite | 0,51 |
| 1168,5 | 1168,75 | Undeformed coarse-grained halite | 0,25 |
| 1168,75 | 1168,85 | Halite mylonite | 0,1 |
| 1168,85 | 1169,12 | Halite mylonite | 0,27 |
| 1169,12 | 1169,37 | Core loss | 0,25 |
| 1169,37 | 1173,09 | Low viscous deformed breccia | 3,72 |
| 1173,09 | 1173,95 | Halite mylonite | 0,86 |
| 1173,95 | 1174,35 | Undeformed anhydrite and clay | 0,4 |
| 1174,35 | 1175,68 | Undeformed anhydrite and clay | 1,33 |
| 1175,68 | 1175,9 | Halite with stylolithic clay layers | 0,22 |

| | | | |
|---|---|---|---|
| 1175,9 | 1175,96 | Undeformed anhydrite and clay | 0,06 |
| 1175,96 | 1176,08 | Halite with stylolithic clay layers | 0,12 |
| 1176,08 | 1176,15 | Undeformed anhydrite and clay | 0,07 |
| 1176,15 | 1176,37 | Halite with stylolithic clay layers | 0,22 |
| 1176,37 | 1176,55 | Undeformed anhydrite and clay | 0,18 |
| 1176,55 | 1176,63 | Halite with stylolithic clay layers | 0,08 |
| 1176,63 | 1176,71 | Undeformed anhydrite and clay | 0,08 |
| 1176,71 | 1176,85 | Halite with stylolithic clay layers | 0,14 |
| 1176,85 | 1177,02 | Undeformed anhydrite and clay | 0,17 |
| 1177,02 | 1178,1 | Viscous undeformed halite with seams of clay | 1,08 |
| 1178,1 | 1178,88 | Viscous undeformed halite with seams of clay | 0,78 |
| 1178,88 | 1179,3 | Undeformed anhydrite and clay | 0,42 |
| 1179,3 | 1179,47 | Undeformed anhydrite and clay | 0,17 |
| 1179,47 | 1180,04 | Undeformed anhydrite and clay | 0,57 |

| STA3-1 | | | |
|---|---|---|---|
| depth interval [m] | | Lithological group | Thickness [m] |
| 1135 | 1135,31 | Undeformed anhydrite and clay | 0,31 |
| 1135,31 | 1136,03 | Halite with stylolithic clay layers | 0,72 |
| 1136,03 | 1136,2 | Undeformed anhydrite and clay | 0,17 |
| 1136,2 | 1139,67 | Undeformed anhydrite and clay | 3,47 |
| 1139,67 | 1140,07 | Core loss | 0,4 |
| 1140,07 | 1140,45 | Undeformed anhydrite and clay | 0,38 |
| 1140,45 | 1140,7 | Core loss | 0,25 |
| 1140,7 | 1141,33 | Undeformed anhydrite and clay | 0,63 |
| 1141,33 | 1143,45 | Viscous undeformed halite with seams of clay | 2,12 |
| 1143,45 | 1143,87 | Low viscous deformed halite | 0,42 |
| 1143,87 | 1144,23 | Halite mylonite | 0,36 |
| 1144,23 | 1144,31 | Low viscous deformed halite | 0,08 |
| 1144,31 | 1146,16 | Halite mylonite | 1,85 |
| 1146,16 | 1147,82 | Halite mylonite | 1,66 |
| 1147,82 | 1151,17 | Low viscous deformed breccia | 3,35 |
| 1151,17 | 1151,27 | Core loss | 0,1 |
| 1151,27 | 1152,26 | Low viscous deformed breccia | 0,99 |
| 1152,26 | 1153 | Viscous deformed breccia | 0,74 |
| 1153 | 1154,48 | Viscous deformed breccia | 1,48 |
| 1154,48 | 1154,98 | Core loss | 0,5 |
| 1154,98 | 1155,34 | Viscous deformed breccia | 0,36 |
| 1155,34 | 1158,42 | Viscous deformed breccia | 3,08 |
| 1158,42 | 1159,79 | Undeformed anhydrite and clay | 1,37 |
| 1159,79 | 1160,04 | Core loss | 0,25 |
| 1160,04 | 1160,82 | Low viscous deformed breccia | 0,78 |
| 1160,82 | 1161,9 | Undeformed anhydrite and clay | 1,08 |
| 1161,9 | 1162,62 | Low viscous deformed breccia | 0,72 |
| 1162,62 | 1163,22 | Halite mylonite | 0,6 |

| | | | |
|---|---|---|---|
| 1163,22 | 1163,32 | Core loss | 0,1 |
| 1163,32 | 1163,88 | Halite mylonite | 0,56 |
| 1163,88 | 1164,13 | Core loss | 0,25 |
| 1164,13 | 1164,8 | Halite mylonite | 0,67 |
| 1164,8 | 1165,36 | Halite with stylolithic clay layers | 0,56 |
| 1165,36 | 1165,55 | Core loss | 0,19 |
| 1165,55 | 1166,92 | Undeformed anhydrite and clay | 1,37 |
| 1166,92 | 1167,2 | Halite with stylolithic clay layers | 0,28 |
| 1167,2 | 1167,61 | Undeformed anhydrite and clay | 0,41 |
| 1167,61 | 1169,49 | Halite with stylolithic clay layers | 1,88 |
| 1169,49 | 1169,6 | Core loss | 0,11 |
| 1169,6 | 1169,74 | Undeformed coarse-grained halite | 0,14 |
| 1169,74 | 1171 | Halite with stylolithic clay layers | 1,26 |
| 1171 | 1171,5 | Core loss | 0,5 |
| 1171,5 | 1172,88 | Halite with stylolithic clay layers | 1,38 |
| 1172,88 | 1172,94 | Undeformed coarse-grained halite | 0,06 |
| 1172,94 | 1173,2 | Halite with stylolithic clay layers | 0,26 |
| 1173,2 | 1175,07 | Undeformed anhydrite and clay | 1,87 |

| BUL1-1B | | | |
|---|---|---|---|
| depth interval [m] | | Lithological type | Thickness [m] |
| 1245 | 1245,55 | Undeformed anhydrite and clay | 0,55 |
| 1245,55 | 1246 | Viscous undeformed halite with seams of clay | 0,45 |
| 1246 | 1246,62 | Low viscous deformed breccia | 0,62 |
| 1246,62 | 1248,18 | Halite mylonite | 1,56 |
| 1248,18 | 1248,5 | Authigenic halite breccia | 0,32 |
| 1248,5 | 1248,94 | Halite mylonite | 0,44 |
| 1248,94 | 1251,56 | Low viscous deformed breccia | 2,62 |
| 1251,56 | 1253,12 | Low viscous deformed breccia | 1,56 |
| 1253,12 | 1255,2 | Low viscous deformed breccia | 2,08 |
| 1255,2 | 1255,69 | Low viscous deformed breccia | 0,49 |
| 1255,69 | 1257,9 | Low viscous deformed breccia | 2,21 |
| 1257,9 | 1258 | Undeformed anhydrite and clay | 0,1 |
| 1258 | 1258,14 | Low viscous deformed halite | 0,14 |
| 1258,14 | 1258,39 | Undeformed anhydrite and clay | 0,25 |
| 1258,39 | 1259,18 | Low viscous deformed breccia | 0,79 |
| 1259,18 | 1259,94 | Halite mylonite | 0,76 |
| 1259,94 | 1260,32 | Viscous undeformed halite with seams of clay | 0,38 |
| 1260,32 | 1261 | Undeformed anhydrite and clay | 0,68 |

| BAC1-1 | | | |
|---|---|---|---|
| depth interval [m] | | Lithological group | Thickness [m] |
| 1160 | 1160,54 | Undeformed anhydrite and clay | 0,54 |

| | | | |
|---|---|---|---|
| 1160,54 | 1161,14 | Halite with stylolithic clay layers | 0,6 |
| 1161,14 | 1162,14 | Halite mylonite | 1 |
| 1162,14 | 1162,96 | Halite mylonite | 0,82 |
| 1162,96 | 1163,49 | Halite mylonite | 0,53 |
| 1163,49 | 1163,6 | Low viscous deformed halite | 0,11 |
| 1163,6 | 1163,75 | Low viscous deformed halite | 0,15 |
| 1163,75 | 1164,47 | Halite with stylolithic clay layers | 0,72 |
| 1164,47 | 1164,51 | Halite mylonite | 0,04 |
| 1164,51 | 1164,62 | Low viscous deformed halite | 0,11 |
| 1164,62 | 1169,71 | Undeformed anhydrite and clay | 5,09 |
| 1169,71 | 1170,49 | Viscous undeformed halite with seams of clay | 0,78 |
| 1170,49 | 1170,79 | Halite mylonite | 0,3 |
| 1170,79 | 1172,48 | Low viscous deformed halite | 1,69 |
| 1172,48 | 1172,92 | Low viscous deformed halite | 0,44 |
| 1172,92 | 1175,24 | Low viscous deformed halite | 2,32 |
| 1175,24 | 1175,51 | Undeformed coarse-grained halite | 0,27 |
| 1175,51 | 1175,59 | Undeformed anhydrite and clay | 0,08 |
| 1175,59 | 1176,35 | Viscous undeformed halite with seams of clay | 0,76 |
| 1176,35 | 1182,17 | Authigenic halite breccia | 5,82 |
| 1182,17 | 1182,42 | Halite with stylolithic clay layers | 0,25 |
| 1182,42 | 1184,75 | Authigenic halite breccia | 2,33 |
| 1184,75 | 1184,94 | Halite with stylolithic clay layers | 0,19 |
| 1184,94 | 1184,95 | Halite mylonite | 0,01 |
| 1184,95 | 1185,26 | Halite with stylolithic clay layers | 0,31 |
| 1185,26 | 1185,75 | Undeformed anhydrite and clay | 0,49 |
| 1185,75 | 1185,95 | Halite with stylolithic clay layers | 0,2 |
| 1185,95 | 1186,61 | Halite mylonite | 0,66 |
| 1186,61 | 1186,79 | Low viscous deformed halite | 0,18 |
| 1186,79 | 1186,84 | Halite mylonite | 0,05 |
| 1186,84 | 1186,88 | Low viscous deformed halite | 0,04 |
| 1186,88 | 1187,3 | Halit mit stylolithischen Tonlagen | 0,42 |
| 1187,3 | 1189,34 | Undeformed anhydrite and clay | 2,04 |
| 1189,34 | 1189,55 | Undeformed anhydrite and clay | 0,21 |
| 1189,55 | 1189,75 | Undeformed anhydrite and clay | 0,2 |
| 1189,75 | 1191,4 | Viscous undeformed halite with seams of clay | 1,65 |
| 1191,4 | 1192,61 | Viscous undeformed halite with seams of clay | 1,21 |
| 1192,61 | 1195,29 | Viscous undeformed halite with seams of clay | 2,68 |
| 1195,29 | 1196,64 | Undeformed anhydrite and clay | 1,35 |

## 11.2. Measurements of survivor grains

| STA2-1 | | | | |
|---|---|---|---|---|
| Depth [m] | Length [mm] | Width [mm] | Angle to foliation plane [°] | Aspect Ratio |
| 1153,75 | 50 | 12 | 20 | 4,17 |
| 1153,87 | 45 | 11 | 18 | 4,09 |
| 1153,88 | 33 | 12 | 25 | 2,75 |
| 1153,89 | 36 | 9 | 15 | 4,00 |
| 1153,99 | 50 | 8 | 20 | 6,25 |
| 1153,75 | 30 | 8 | 10 | 3,75 |
| 1153,93 | 45 | 12 | 23 | 3,75 |
| 1153,92 | 48 | 16 | 22 | 3,00 |
| 1156,70 | 22 | 16 | 40 | 1,38 |
| 1156,80 | 18 | 16 | 39 | 1,13 |
| 1156,98 | 15 | 13 | 52 | 1,15 |
| 1156,87 | 26 | 6 | 41 | 4,33 |
| 1156,91 | 13 | 11 | 25 | 1,18 |
| 1156,97 | 13 | 11 | 46 | 1,18 |
| 1158,30 | 10 | 4 | 40 | 2,50 |
| 1158,31 | 21 | 4 | 42 | 5,25 |
| 1158,32 | 18 | 8 | 41 | 2,25 |
| 1162,19 | 33 | 15 | 35 | 2,20 |
| 1162,37 | 17 | 8 | 54 | 2,13 |
| 1162,36 | 12 | 5 | 42 | 2,40 |
| 1162,45 | 18 | 9 | 38 | 2,00 |
| 1162,59 | 18 | 8 | 44 | 2,25 |
| 1162,60 | 20 | 7 | 61 | 2,86 |
| 1162,83 | 25 | 6 | 37 | 4,17 |
| 1162,63 | 12 | 10 | 42 | 1,20 |
| 1162,68 | 3 | 4 | 44 | 0,75 |
| 1162,44 | 23 | 10 | 54 | 2,30 |
| 1162,49 | 12 | 8 | 54 | 1,50 |
| 1162,56 | 27 | 11 | 38 | 2,45 |
| 1162,65 | 48 | 15 | 40 | 3,20 |
| 1163,37 | 16 | 12 | 43 | 1,33 |
| 1163,33 | 23 | 10 | 54 | 2,30 |
| 1163,66 | 34 | 5 | 40 | 6,80 |
| 1165,28 | 16 | 11 | 28 | 1,45 |
| 1165,31 | 27 | 25 | - | 1,08 |
| 1165,35 | 32 | 20 | 29 | 1,60 |
| 1165,67 | 30 | 22 | 27 | 1,36 |
| 1165,17 | 23 | 15 | 28 | 1,53 |
| 1165,20 | 22 | 12 | 27 | 1,83 |
| 1165,42 | 20 | 12 | 27 | 1,67 |
| 1165,74 | 24 | 15 | 16 | 1,60 |

| | | | | |
|---|---|---|---|---|
| 1165,89 | 20 | 10 | 0 | 2,00 |
| 1165,91 | 16 | 9 | 0 | 1,78 |
| 1165,95 | 22 | 13 | 15 | 1,69 |
| 1165,78 | 42 | 25 | -3 | 1,68 |
| 1165,85 | 30 | 16 | 12 | 1,88 |
| 1165,87 | 32 | 15 | 5 | 2,13 |
| 1173,91 | 15 | 10 | 28 | 1,50 |
| 1173,92 | 20 | 8 | 22 | 2,50 |
| 1173,11 | 32 | 11 | 18 | 2,91 |
| 1173,13 | 70 | 37 | 20 | 1,89 |
| 1173,12 | 30 | 12 | 14 | 2,50 |
| 1173,10 | 47 | 11 | 26 | 4,27 |
| 1173,86 | 17 | 4 | 25 | 4,25 |

| STA3-1 | | | | |
|---|---|---|---|---|
| Depth [m] | Length [mm] | Width [mm] | Angle to foliation plane [°] | Aspect Ratio |
| 1143,87 - 1144,23 | 60 | 20 | 13 | 3,00 |
| | 45 | 18 | 25 | 2,50 |
| | 25 | 7 | 31 | 3,57 |
| | 45 | 11 | 26 | 4,09 |
| | 33 | 15 | 16 | 2,20 |
| | 27 | 8 | 18 | 3,38 |
| 1144,31 - 1146,16 | 29 | 12 | 21 | 2,42 |
| | 40 | 14 | 25 | 2,86 |
| | 25 | 7 | 18 | 3,57 |
| | 23 | 7 | 23 | 3,29 |
| | 32 | 9 | 28 | 3,56 |
| | 18 | 8 | 22 | 2,25 |
| | 14 | 6 | 19 | 2,33 |
| | 24 | 12 | 26 | 2,00 |
| | 20 | 11 | 29 | 1,82 |
| | 55 | 15 | 17 | 3,67 |
| | 25 | 11 | 22 | 2,27 |
| | 16 | 8 | 24 | 2,00 |
| | 15 | 5 | 25 | 3,00 |
| | 34 | 12 | 28 | 2,83 |
| | 20 | 10 | 17 | 2,00 |
| 1146,16 - 1147,82 | 18 | 8 | 25 | 2,25 |
| | 20 | 10 | 29 | 2,00 |
| | 28 | 12 | 30 | 2,33 |
| | 23 | 8 | 25 | 2,88 |
| | 26 | 9 | 28 | 2,89 |
| | 22 | 10 | 30 | 2,20 |
| | 20 | 6 | 33 | 3,33 |

| | | | | |
|---|---|---|---|---|
| 1153,00 - 1154,48 | 28 | 9 | 28 | 3,11 |
| | 19 | 5 | 33 | 3,80 |
| | 35 | 13 | 23 | 2,69 |
| | 18 | 8 | 24 | 2,25 |
| | 16 | 4 | 28 | 4,00 |
| | 26 | 6 | 27 | 4,33 |
| | 32 | 11 | 20 | 2,91 |
| | 25 | 6 | 24 | 4,17 |
| | 29 | 10 | 30 | 2,90 |
| | 17 | 8 | 22 | 2,13 |

| BUL1-1B | | | | |
|---|---|---|---|---|
| Depth interval [m] | Length [mm] | Width [mm] | Angle to foliation plane [°] | Aspect Ratio |
| 1248,50 - 1248,94 | 16 | 6 | 8 | 2,67 |
| | 20 | 7 | -4 | 2,86 |
| | 10 | 5 | 22 | 2,00 |
| | 18 | 7 | 26 | 2,57 |
| | 13 | 6 | 5 | 2,17 |
| 1259,18 - 1259,94 | 20 | 11 | 23 | 1,82 |

| BAC1-1 | | | | |
|---|---|---|---|---|
| Depth interval [m] | Length [mm] | Width [mm] | Angle to foliation plane [°] | Aspect Ratio |
| 1186,61 - 1186,79 | 28 | 14 | 34 | 2,00 |
| | 24 | 13 | 30 | 1,85 |
| | 36 | 21 | 35 | 1,71 |
| | 42 | 14 | 21 | 3,00 |
| | 22 | 7 | 29 | 3,14 |
| | 17 | 7 | 40 | 2,43 |
| | 20 | 9 | 34 | 2,22 |
| | 25 | 9 | 23 | 2,78 |
| | 22 | 8 | 31 | 2,75 |
| | 44 | 13 | 35 | 3,38 |
| | 32 | 11 | 38 | 2,91 |
| | 13 | 5 | 41 | 2,60 |
| | 18 | 7 | 38 | 2,57 |

## 11.3. Measurements of shear bands

| STA3-1 | | |
|---|---|---|
| Depth interval [m] | Length [mm] | Width [mm] |
| 1153,00 - 1154,48 | 80 | 6 |
| | 60 | 8 |
| | 90 | 7 |
| | 80 | 9 |
| | 110 | 12 |
| | 110 | 10 |
| | 100 | 8 |

## 11.4. Measurements of boudins

| STA2-1 1155.50m | | |
|---|---|---|
| Length [mm] | Width [mm] | Aspect ratio |
| 0,829 | 0,561 | 1,48 |
| 1,343 | 0,898 | 1,50 |
| 0,656 | 0,431 | 1,52 |
| 0,16 | 0,105 | 1,52 |
| 0,258 | 0,166 | 1,55 |
| 0,196 | 0,124 | 1,58 |
| 0,147 | 0,091 | 1,62 |
| 0,291 | 0,177 | 1,64 |
| 0,49 | 0,289 | 1,70 |
| 0,592 | 0,343 | 1,73 |
| 0,474 | 0,258 | 1,84 |
| 0,174 | 0,092 | 1,89 |
| 0,401 | 0,211 | 1,90 |
| 0,094 | 0,049 | 1,92 |
| 1,277 | 0,649 | 1,97 |
| 0,077 | 0,039 | 1,97 |
| 0,309 | 0,156 | 1,98 |
| 0,872 | 0,433 | 2,01 |
| 1,279 | 0,632 | 2,02 |
| 0,214 | 0,105 | 2,04 |
| 0,327 | 0,16 | 2,04 |
| 0,824 | 0,398 | 2,07 |
| 0,505 | 0,241 | 2,10 |
| 0,789 | 0,364 | 2,17 |
| 0,328 | 0,147 | 2,23 |
| 1,241 | 0,537 | 2,31 |
| 0,479 | 0,207 | 2,31 |
| 0,606 | 0,26 | 2,33 |
| 0,363 | 0,153 | 2,37 |

| | | |
|---|---|---|
| 0,216 | 0,09 | 2,40 |
| 0,108 | 0,045 | 2,40 |
| 0,372 | 0,152 | 2,45 |
| 2,133 | 0,858 | 2,49 |
| 0,458 | 0,184 | 2,49 |
| 0,682 | 0,273 | 2,50 |
| 0,472 | 0,188 | 2,51 |
| 1,487 | 0,569 | 2,61 |
| 0,247 | 0,094 | 2,63 |
| 1,817 | 0,685 | 2,65 |
| 0,55 | 0,202 | 2,72 |
| 0,255 | 0,092 | 2,77 |
| 0,241 | 0,085 | 2,84 |
| 0,998 | 0,347 | 2,88 |
| 0,219 | 0,076 | 2,88 |
| 0,766 | 0,265 | 2,89 |
| 0,72 | 0,246 | 2,93 |
| 0,401 | 0,136 | 2,95 |
| 0,891 | 0,297 | 3,00 |
| 0,218 | 0,071 | 3,07 |
| 0,727 | 0,233 | 3,12 |
| 2,116 | 0,675 | 3,13 |
| 2,436 | 0,771 | 3,16 |
| 1,078 | 0,34 | 3,17 |
| 0,88 | 0,277 | 3,18 |
| 0,22 | 0,069 | 3,19 |
| 2,821 | 0,879 | 3,21 |
| 1,057 | 0,329 | 3,21 |
| 0,472 | 0,144 | 3,28 |
| 1,953 | 0,595 | 3,28 |
| 0,753 | 0,228 | 3,30 |
| 2,046 | 0,614 | 3,33 |
| 3,279 | 0,983 | 3,34 |
| 0,207 | 0,062 | 3,34 |
| 1,022 | 0,305 | 3,35 |
| 0,512 | 0,15 | 3,41 |
| 1,658 | 0,485 | 3,42 |
| 0,559 | 0,163 | 3,43 |
| 0,594 | 0,172 | 3,45 |
| 0,616 | 0,178 | 3,46 |
| 0,492 | 0,139 | 3,54 |
| 0,376 | 0,106 | 3,55 |
| 0,647 | 0,18 | 3,59 |
| 0,201 | 0,055 | 3,65 |
| 1,711 | 0,456 | 3,75 |
| 1,234 | 0,326 | 3,79 |
| 0,517 | 0,136 | 3,80 |

| | | |
|---|---|---|
| 0,561 | 0,147 | 3,82 |
| 3,56 | 0,914 | 3,89 |
| 0,715 | 0,178 | 4,02 |
| 0,519 | 0,127 | 4,09 |
| 0,379 | 0,091 | 4,16 |
| 0,751 | 0,178 | 4,22 |
| 0,558 | 0,13 | 4,29 |
| 0,486 | 0,111 | 4,38 |
| 0,586 | 0,133 | 4,41 |
| 2,29 | 0,514 | 4,46 |
| 0,903 | 0,199 | 4,54 |
| 0,64 | 0,14 | 4,57 |
| 0,624 | 0,136 | 4,59 |